Julius−Maximilians−Universität Würzburg
Graduate School of Science and Technology

Doctoral thesis / *Dissertation*

for the doctoral degree / *zur Erlangung des Doktorgrads*

Doctor rerum naturalium (Dr. rer. nat.)

Fabrication and Optical and Electronic Characterization of Conjugated Polymer-Stabilized Semiconducting Single-Wall Carbon Nanotubes in Dispersions and Thin Films

Herstellung und Optische- und Elektronische- Charakterisierung von konjugierten Polymer-stabilisierten halbleitenden Kohlenstoffnanoröhren in Dispersionen und dünnen Filmen

Submitted by / *Vorgelegt von*

Imge Namal

from / *aus*

Keçiören

Würzburg, 2017

Submitted on / *Eingereicht am*:
……

Stamp / *Stempel* Graduate School

Members of thesis committee / *Mitglieder des Promotionskomitees*

Chairperson / *Vorsitz*:
……

1. Reviewer and Examiner / *1. Gutachter und Prüfer*:
……..

2. Reviewer and Examiner / *2. Gutachter und Prüfer*:
……..

3. Examiner / *3. Prüfer*:
……

Additional Examiners / *Weitere Prüfer*:
……

……
……

Day of thesis defense / *Tag des Promotionskolloquiums*:
……

Table of Contents

1. Introduction

Semiconductor devices are the foundation of the consumer electronics industry, which is expected to have an 800 billion USD market by 2020 [1]. By the same year, silicon-based semiconductor technology is expected to reach absolute limits on its performance [2]. This means that improvements in transistor speed and performance will have to come from new materials. In the search of a suitable material, single-wall carbon nanotubes (SWNTs) received considerable attention due to their exceptional electrical, physical and thermal properties. [3–5]

When SWNTs were first discovered by Iijima and Ichihashi in 1993 [6], it was foreseen to immediately replace silicon in the electronics industry, but it has taken 15 years from the first reports on SWNT field effect transistors (FETs) [7,8] to the appearance of the first SWNT processor [9, 10]. The road to producing transistors from single-wall carbon nanotubes has been hindered by the difficulties in achieving electronic and chiral separation, dispersing in a solvent and reproducible production of a thin film.

The electronic properties of SWNTs are dependent on their diameter and chirality as well as aggregation state [11]. In order to overcome the difficulty of electronic heterogeneity and obtain a stable dispersion of SWNTs of selected chirality, polymer wrapping is found to be a practical method [12, 13]. With the help of the π–π interactions between conjugated polymers and carbon nanotubes, high electronic and chiral selectivity of SWNTs is obtained. Although there has been some improvement on obtaining different compositions of dispersions with different polymer combinations [14–23], a comprehensive understanding of the selective dispersion of SWNTs with conjugated polymers was missing.

Formation of films of SWNTs on desired substrates is the second challenge for their use in semiconducting device applications. Solution deposition techniques are attractive because resulting films can be cost–effectively up–scaled and a wide variety of substrates can be used [24]. The problem is, the most common solution deposition methods result with a non–uniform distribution of materials when scaling up the dimension [25–27]. Therefore, reproducible and scalable methods that produce uniform macroscopic SWNT thin films of foreseeable optical, topographical or electronic properties are of high demand.

This work starts with background information in Chapter Two, covering the structural properties of SWNTs, physical properties of wrapping polymers, factors influencing thin film properties and an introduction to the theory of thin film field effect transistors.

Following the theory, chapter three consists of the equipment, material and the experimental method of this work. Information about analysis results of the wrapping polymers, revealing their molecular weight and electronic band gap as well as device architecture of the measured SWNT FETs can be found there.

Within the scope of this work, aforementioned challenges were addressed. Through controllable change of the polymer backbone and SWNT raw material, insights into the polymer wrapping were searched in chapter four. A thin film preparation method accustomed for polymer wrapped SWNTs, producing scalable and uniform thin films was presented and with vertical scaling, the change in optical and electronic properties of the SWNT thin films was examined in chapter five. Following, in chapter six, a summary and an outlook for this study will be presented.

2. Background Information

Research on the science and applications of single−wall carbon nanotubes (SWNTs) has been the focus of both experimentalists and theoreticians for almost three decades due to their outstanding properties. In this section, a short introduction into these properties will be presented.

Afterwards, details about physical properties of polymers will be discussed in the context of selective dispersion of SWNTs via polymer wrapping. Lastly, factors affecting thin film properties of SWNTs and corresponding electronic applications such as field effect transistors will be discussed.

2.1 Geometric and Electronic Structure of SWNTs

A single-wall carbon nanotube (SWNT) can be conceptualized as a single sheet of graphene, rolled into a cylinder. The circumference of the SWNT is defined with a lattice chiral vector of C_h and its length along the tube axis is defined with a translational vector of T:

$$C_h = n a_1 + m a_2 \tag{2.1}$$

$$\bar{T} = \frac{2m+n}{d_R}\overline{a_1} + \frac{2n+m}{d_R}\overline{a_2} \tag{2.2}$$

where n and m are the integers defining the chirality of the resulting cylinder and a_1 and a_2 are the unit vectors for the lattice of the graphene sheet.

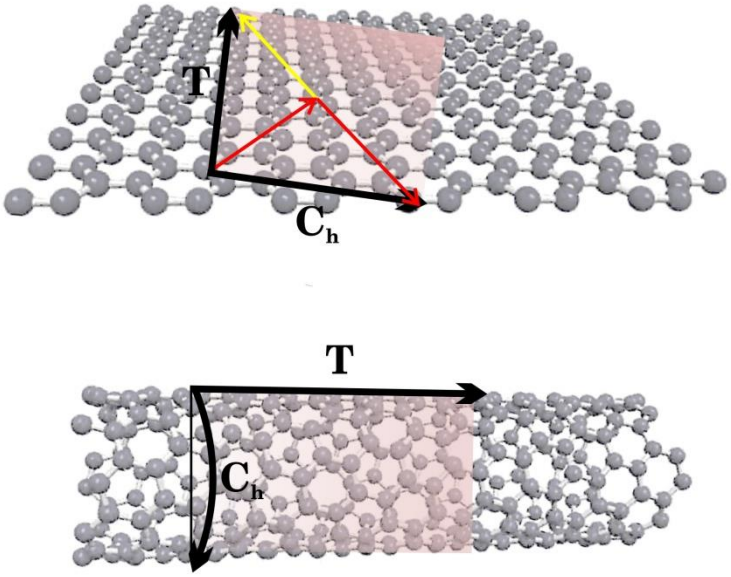

Figure 2.1: Graphic representation showing the structure of SWNTs. Schematic illustration of the structures of an SWNT with lattice chiral vector C_h and tube axis T.

These indices can be used to calculate the diameter and chiral angle of the SWNT [171,172] using the following equations:

$$d=\frac{a}{\pi}\sqrt{n^2+m^2+nm} \tag{2.3}$$

$$\cos\theta = \frac{2n+m}{2\sqrt{n^2+m^2+nm}} \tag{2.4}$$

The electronic properties of SWNTs depend on their structure, determining whether it is metallic or semiconducting and can be designated also with the help of the integers, n, m. If n−m is a multiple of 3, SWNT is metallic and otherwise semiconducting. The band gaps of semiconducting SWNTs are inversely proportional to their diameter. This can be explained by the following equation [173]. :

$$E_g = \gamma\left(\frac{2R_{c-c}}{d_{SWNT}}\right) \tag{2.5}$$

where γ is the hopping matrix element (~3 eV), R_{C-C} is the C−C bond length and d is the SWNT diameter.

The electronic structure of SWNTs can be explained with the help of the electronic structure of graphene. Due to translational symmetry along the unit vectors, linear combinations of Bloch functions can be used to solve stationary Schrödinger Equation for single electron wave functions in a periodic crystal lattice. In the Brillouin zone, which is the corresponding unit cell representing the periodically occurring smallest unit in the reciprocal space, the electron dispersion of graphene can be calculated by the tight binding model. In the Dirac energy dispersion cone, the two bands of graphene overlap in the Fermi level (at the point K), where the electronic density of states is zero. Therefore, graphene is a semiconductor with a vanished band gap. The wave vector, k can take any value.

When graphene is rolled up to an SWNT, boundary conditions are applied. While the parallel wave vector to the tube axis, $k_{\parallel}$, stays constant, wave vector perpendicular to the tube axis is quantized. The electronic properties of an SWNT depend on the projection of the energy dispersion of graphene on the wave vector perpendicular to the tube axis. If the projection includes a K point, where the two bands meet, the SWNT lacks a band gap and is therefore metallic. Otherwise, the SWNT is semiconducting.

Minima and maxima in the energy dispersion of SWNTs lead to the van Hove Singularities in the density of states. According to the one-particle picture of optical processes, transitions between the van Hove Singularities, connecting the valence and conduction bands are enhanced and correspond to the optical transitions. Optical transitions of SWNTs on the other hand, cannot be fully explained using one particle picture, as it does not consider the enhanced Coulomb interactions in a 1D confinement.

In three-dimensional semiconductors like Si, and Ge, the binding energy of an exciton, a photoexcited electron-hole pair, is calculated to be around 10 meV, which is energetically lower than the single particle excitation. Consequently, optical absorption to exciton levels cannot be observed for these semiconductors at room temperature. SWNTs, due to their 1D nature, have enhanced Coulomb interactions and a transfer of the oscillator strength from the electron-hole continuum to the excitonic transitions is observed. As a result, the binding energy of the exciton (~100 meV) is much larger than in three-dimensional semiconductors.

The increased exciton binding energy in SWNTs acts against a stronger increase in the size of the band gap due to the reduced effective charge density on each charge carrier with increased many-body interactions. As a result, a phenomenon called "band gap renormalization" is observed, causing an increase in the absorption energy of the S_1 exciton. The many-body interactions in SWNTs, which cause the bandgap renormalization are affected by the surrounding medium. Since the electric field lines lay outside of the carbon nanotubes, the screening of the electron and hole depends on the environment. The electronic transitions of SWNTs are therefore dependent on the permittivity of the medium. The size of the shift in the optical transitions due to the permittivity of the medium is found to be between 1 and 10 meV.

Excitons can be classified as Wannier-Mott Excitons or Frenkel Excitons depending on the properties of the material in question. In SWNTs, excitons have both characteristics, due to the Coulomb interactions in their 1D confinement. The dielectric function of the nanotube is large enough to allow for the exciton wave function to extend over several nanometers along the tube axis, qualifying for a Wannier-Mott Exciton. Poor screening in the dielectric environment outside the SWNT, on the other hand, causes large exciton binding energies for the Frenkel Excitons.

Several excitons of different symmetry are obtained for each excitonic transition. In chiral SWNTs where n ≠ m and m≠0, every Van Hove singularity has two degenerate sub-bands. From the four singlet excitons, only one is symmetry allowed due to the selection rules for one-photon excitation. The energetically lowest state which is also called as S_0 is a dark state. A direct optical excitation from S_0 sub-band is not allowed. The second lowest state which is the S_1 sub-band is symmetry allowed for an optical excitation. Through the absorption of a photon, transition of an exciton with an A_1 symmetry in the ground state into A_2 symmetry in the S_1 sub-band is observed to be a bright exciton. Often, due to a Stokes Shift of a couple of meV's, there is a bright S_2 exciton appearing in the absorption spectrum of an excited SWNT. The relaxation of this exciton is almost 90% through S_1 sub-band.

Quantum yield for SWNTs, which is defined as the ratio of emitted to absorbed photons is measured to be exceeding 1% [83]. Structural defects, tube ends, bound metallic species and impurities may act as quenching sites, decreasing the quantum yield. Consequently, the synthesis method, the post-synthesis treatment, and the stabilizing agent are elements that affect the obtained quantum yield [170].

2.2 Physical Properties of Polymers and Selective Dispersion of SWNTs by Polymer Wrapping

Polymers are classified according to the sequence of the monomers it is composed of. If there is only one type of monomer that the polymer is made up of, it is called a homopolymer. If there is a variety in the nature of the monomers, it is called a copolymer of these units. Copolymers can be block, alternating or random due to the presence of a specific order in the organization of the monomers.

The number of monomer units in a linear polymer chain is expressed with the degree of polymerization. For most industrial purposes, degrees of polymerization in the thousands or tens of thousands are desired. In general, increasing degree of polymerization correlates with higher melting temperature and higher mechanical strength [27]. As individual polymer chains rarely have exactly the same degree of polymerization and molecular weight, a molecular weight distribution is used in order to express the average value. The difference in molecular weight of the polymer may cause a difference in its physical properties hence the same composition. Three different average values are generally used for expressing molecular weight of a polymer and they differ in the statistical method applied: Number average molecular weight, weight average molecular weight, and Z−average molecular weight. In this work, weight average molecular weight is used in order to define the molecular weight of the wrapping polymers. It is expressed as:

$$\overline{M_w} = \frac{\sum_i N_i M_i^2}{\sum_i N_i M^i} \tag{2.6}$$

where N_i is the number of molecules of molecular weight M_i.

Another important property that needs to be considered while introducing a polymer is the solubility of the polymer and correspondingly the conformation of the polymer in a specific solution. There, the intramolecular forces play an important role. In the presence of a flexible backbone where single C−C bonds can rotate, a high amount of different conformations of the polymer is possible [28].

In order to explain the thermodynamics of the solubility of polymers, Flory−Huggins solution theory can be introduced. It considers the dissimilarities in the molecular sizes of solute and solvent molecules and adapts the expression for the entropy of mixing to obtain the Gibbs free energy change for mixing:

$$\Delta G_{mix} = \Delta H_{mix} - T\Delta S_{mix} \tag{2.7}$$

As the solute is a macromolecule and not a small molecule, instead of using mole fractions, it assumes that each polymer and solvent segment occupies a part in a lattice. So the total number of parts in the lattice (N) would be:

$$N = N_1 + xN_2 \tag{2.8}$$

N_1 is the number of solvent molecules and N_2 is the number of polymer molecules, each molecule having x segments. The change in the entropy (ΔS_{mix}) from this mixing would be:

$$\Delta S_{mix} = -\kappa[N_1 ln\frac{N_1}{N} + N_2 ln\frac{xN_2}{N}] \tag{2.9}$$

where κ is the Boltzmann's constant, $\frac{N_1}{N}$ is the lattice volume fraction of the solvent (ϕ_1) and $\frac{\chi N_2}{N}$ is the lattice volume fraction of the polymer (ϕ_2).

For the change in enthalpy, 3 different interactions should be considered: solvent-solvent (ω_{11}), polymer-polymer (ω_{22}) and polymer-solvent interactions (ω_{12}). The energy change per monomer-solvent contact is:

$$\Delta\omega = \omega_{12} - \frac{\omega_{11}+\omega_{22}}{2} \tag{2.10}$$

The total number of monomer solvent contact is:

$$N_1\phi_2 \mathrm{Z} = xN_2\phi_1 \mathrm{Z} \tag{2.11}$$

where Z is the number of nearest neighbors for a lattice part. The change in the enthalpy is:

$$\Delta H_{mix} = N_1\phi_2 \mathrm{Z}\Delta\omega \tag{2.12}$$

The equation for this Gibbs energy change is:

$$\Delta G_{mix=} RT\left[N_1 ln\phi_1 + N_2 ln\phi_2 + N_1\phi_2\frac{\mathrm{Z}\Delta\omega}{\kappa T}\right] \tag{2.13}$$

$\frac{Z\Delta\omega}{\kappa T}$ can be expressed as χ_{12}, which is the parameter for the energy of mixing polymer and solvent molecules. It is also called the Flory–Huggins parameter. An ideal solvent of a polymer has an χ of 0.5 where there is neither attractive nor repulsive forces between the polymer units. When χ has a higher value than 0.5, the mixture is not energetically favorable and the solvent is not suitable for the polymer.

For the polyfluorene and polycarbazole derivatives used in this study, toluene was found to be a good solvent [30,31]. For the adsorption of polymer segments on SWNTs, SWNT–solvent, polymer–solvent, and polymer–SWNT interactions should be taken into account. As there is a decrease in the entropy of the polymer by adsorption to SWNTs, the free energy at the end of this process should be enough to compensate for the loss [32,33].

When selecting a solvent for the selective dispersion of SWNTs, a few criteria should be considered. Firstly, the solvent should have a good solubility for the conjugated wrapping polymer. At the same time, SWNTs should have a low intrinsic solubility in the solvent, such that only polymer–wrapping would enable the dispersion of SWNTs; and the solvent should have a lower density than SWNTs (1.33 g cm^{-2}) to allow the SWNT bundles to sediment after centrifugation. Hwang et al. studied several solvents for sorting SWNTs with PFO and observed that high–density solvents, such as chloroform (density of 1.5 g cm^{-3}), do not achieve the selective dispersion of semiconducting SWNTs. They mentioned the presence of the bundled SWNTs remaining in the solution after centrifugation and attributed this behavior to buoyant forces, causing the SWNT bundles to float on the solvent surface [42].

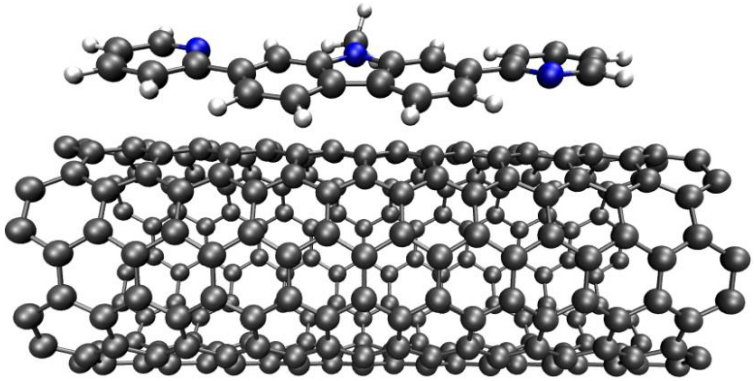

Figure 2.3: Simulation of a pyridine containing polyfluorene derivative on an SWNT.

Adsorption of polymers on SWNTs is through various interactions such as π–π, CH–π or cation–π. The advantage of polymer wrapping is the thermodynamic stability of the polymer, which prevents SWNT aggregation. It is, therefore, possible to remove the unbound polymer without disturbing the polymer–SWNT pair. This process can be carried out by dialysis [34, 35], precipitation/decantation [36], filtration [37,38], ultracentrifugation [39] and chromatography [35].

Although a detailed mechanism of the selective wrapping is still unknown, it is assumed that the π–conjugated polymers with a rigid backbone exhibit the selectivity for the specific chiral indices by aligning their backbones along the SWNTs' surfaces with a preferential angle in order to maximize the interaction on the π–surface [40]. Compared to other separation techniques, polymer wrapping is superior due to its simplicity and the high efficiency in the chiral of semiconducting SWNTs.

2.3 Factors Influencing SWNT Thin Film Properties

Each fabrication step from SWNT synthesis to the film preparation method influences the final electrical optical and mechanical properties of SWNT films. Therefore it is essential to understand each step and their effect on the produced thin film.

2.3.1 Raw Material Dependent Properties

There are different SWNT synthesis methods that produce SWNTs with different lengths and compositions. In this work, CoMoCAT (cobalt-molybdenum catalyst) and CVD (chemical vapor deposition) SWNTs are used.

In chemical vapor deposition, decomposition of hydrocarbons in the presence of an inert gas is aided by the presence of a metallic catalyst. Synthesis for catalytic CVD is performed on a substrate at temperatures ranging from 500 to 1100 ^{o}C or in the presence of enhanced plasma. Synthesized SWNTs can either be left on the substrate or cleaved off for other applications.

There are a variety of different CVD methods like water assisted, oxygen assisted, hot filament, microwave plasma, and radio frequency CVD. The diameter of the resulting tube varies from 0.6 to 2.0 nm and the length of the grown tube is between 100 nm to a couple of centimeters. The yield of the process varies for different methods, but particularly catalytic CVD allows for the large-scale synthesis of SWNTs. A variety of factors such as the temperature [73], type of catalyst [74], hydrocarbon source [76], and substrate [75] can affect the type and properties of the grown SWNTs.

CoMoCAT stands for the method that uses a cobalt–molybdenum catalyst in order to grow SWNTs from a carbon monoxide (CO) source. The first recipe reported was using 1:3 mol ratio of cobalt to molybdenum at 750 ^{o}C

and 5 atm carbon monoxide pressure resulted with more than 50% semiconducting SWNTs, enriched with (6,5) and (7,5) SWNTs [77,158]. The chiral enrichment of the as-synthesized CoMoCAT SWNTs is superior to other synthesis methods chemical vapor deposition or HiPCO. High amounts of SWNTs can be produced with this process. However the resulting raw material has a higher amount of impurities, therefore an extra purification step is needed before SWNTs are further used. The integration of this extra step causes the defect density of CoMoCAT SWNTs to be higher than the raw material obtained from CVD process [77, 80]. The average diameter of the produced SWNTs is around 0.7 to 0.8 nm and their lengths are on average around 900 nm [165, 80].

2.1.1 Thin Film Deposition Technique

There are two main ways of dispersion deposition of carbon nanotube thin films: direct deposition and transfer deposition [25]. Direct film deposition requires wet assembly of the SWNT suspension onto a substrate. High compatibility for various substrates, operation in low temperatures, relatively low costs, and high speed are the advantages of these techniques. However, films fabricated with direct deposition usually have issues with their homogeneity and reproducibility even if same carbon nanotube source was used [26].

The most commonly used direct deposition technique is spin coating. During spin coating, a substrate with an excess amount of dispersion is rotated at a high speed in order to coat the substrate with the help of centrifugal force. The thickness of the film is dependent on spin speed, acceleration, process time, the concentration of the dispersion and the wettability of the substrate [162].

This practical technique has its limitations in the properties of the resulting film. The interaction between SWNTs often makes only a few

consecutive spin coating layers possible, which sets a limit in the achievable thickness and optical density. The nonlinear dependence of film thickness on dispersion volume and concentration makes spin coated SWNT films hardly scalable [160].

Drop casting is also a widely used wet deposition method due to its simplicity. The process is only the casting of the droplet onto the substrate and solvent evaporation drives the deposition to form a thin film. In this technique, the film thickness is proportional to the concentration of the dispersion and limited by the aggregation of the SWNTs. Accordingly, its other limitations are about substrate coverage, film uniformity, and reproducibility [25].

In dip coating, the substrate is submerged into the dispersion and removed after coating takes place. Multiple layers of coating can be done with this method in order to increase the thickness of the film. The technique is time consuming compared to the other methods. The chosen substrate and its roughness affect the film thickness. An increase in roughness corresponds to an increase in SWNT concentration [162].

In inkjet printing, an ink of dispersion is loaded on a printer cartridge and is ejected from a nozzle via the piezoelectric process. After the dispersion is spread on the substrate, the process is like drop casting. Wetting properties of the substrate affect the quality of film deposition. Therefore it is a key issue to control the morphology of the whole array. This technique has an advantage of little to no material waste. There are many other direct deposition methods, including Langmuir Blodgett deposition and spray coating. However, these methods lack in film uniformity, homogeneity or film thickness controllability [166].

Transfer deposition of SWNT films requires the use of a dummy substrate. From the dummy substrate, the fabricated film is transferred onto the selected substrate. Vacuum filtration is one of the most practical transfer

deposition methods for producing macroscopic and transparent networks of randomly oriented carbon nanotubes. A vacuum apparatus is attached to a filter with suitably small pore size and SWNT suspension is poured through the filter. Vacuum filtration of the SWNT suspension creates a concentration gradient due to the fluid velocity across the filter. With suitable suspension concentration and fluid velocity, a nematic phase forms on the surface of the filter [24, 141, 159]. Transfer of the fabricated SWNT film is highly depending on the surface energy between the selected substrate and SWNT film, which needs to be much higher than the surface energy between SWNT film and filter. After film transfer, the filter is removed either by peeling off or dissolving with a solvent in which SWNTs are not soluble.

SWNTs can also be directly grown for aligned arrays but the electronic purity of these arrays is quite low. There have been some post-synthesis treatments for metallic tube removal but besides the concern of large-scale manufacturability, these techniques cause variable numbers of CNTs in the region of interest with unacceptable sample variation [148,161]. In addition to the challenge of s−SWNT purity, the nanotube density, which is typically in the range of 1−50 tubes per µm for as-grown arrays, must be increased to at least 200 tubes per µm to provide sufficient current output in order to be considered for a practical technology [105].

2.4 SWNT Thin Film Field Effect Transistors

There are four basic layers of an organic field effect transistor: Gate, dielectric, semiconductor and channel electrodes, which are the source and drain. According to the chosen architecture, the stacking order of these layers may differ. The gate is a conductor that is mostly bonded to a substrate. The gap between the source and drain electrodes is called the channel. The conductance of the channel is adjusted by the gate bias. Accumulation of induced charges at the interface of dielectric and

semiconductor layers due to the electric field produced by the gate bias is followed by injection of oppositely charged carriers from the source to the drain.

Carbon nanotube electronics have been actively studied due to their superior bulk properties over silicon. Semiconducting SWNTs are expected to outperform silicon in field effect transistors with twice the current density [118,119] and two to three times lower power consumption [120,121] with higher speed and better gate control. In networks of SWNTs, microstructures of the SWNT films are affecting electrical properties of carbon nanotube thin films. Application of an SWNT thin film preparation technique with high levels of control over tube density (number of tubes per unit area for random network films) and spatial layout of SWNTs is critical for their successful application as electronic materials. Experimental and theoretical studies show that these parameters determine the collective electrical, optical and mechanical properties [24, 128, 129, 162].

If a negative bias is applied to the gate while the silicon substrate is grounded, the structure behaves like a parallel-plate capacitor where the two electrodes are the gate and the channel electrodes, and silicon oxide is the dielectric 2 between the gate and the semiconductor (Figure 2.4 left). The application of the bias gives rise to a negative charge on the gate. An equal charge of opposite sign appears at the dielectric/semiconductor interface. From parallel plate capacitance theory, it is known that the majority of the carriers can accumulate at, or deplete from, the dielectric/semiconductor interface and the conductivity of the semiconductor at the interface can be modulated by the gate bias.

For a parallel plate capacitor, charge density exists on the plate's surface which has an area A. The electric field (E) near the center of the device is expected to be uniform with the magnitude $E = (\rho/\varepsilon)$ where ρ is the charge density over the plate's surface ($\rho = Q/A$) and ε is the permittivity constant

for free space. Voltage is defined as the line integral of the electric field between the plates:

$$V = \int_0^d EdZ = \int_0^d \frac{\rho}{\varepsilon} dZ = \frac{\rho d}{\varepsilon} = \frac{Qd}{\varepsilon A} \tag{2.14}$$

Solving this for $C = \frac{Q}{V}$ reveals that capacitance increases with area and decreases with separation of the plates d:

$$C = \frac{(\varepsilon A)}{d} \tag{2.15}$$

Parallel plate capacitance theory is commonly applied to thin film transistors. The semiconducting thin film thickness is neglected and d is taken as the thickness of the dielectric layer. However, capacitance depends as well on the average spacing between the tubes and the distribution of the SWNTs in SWNT FETs [127].

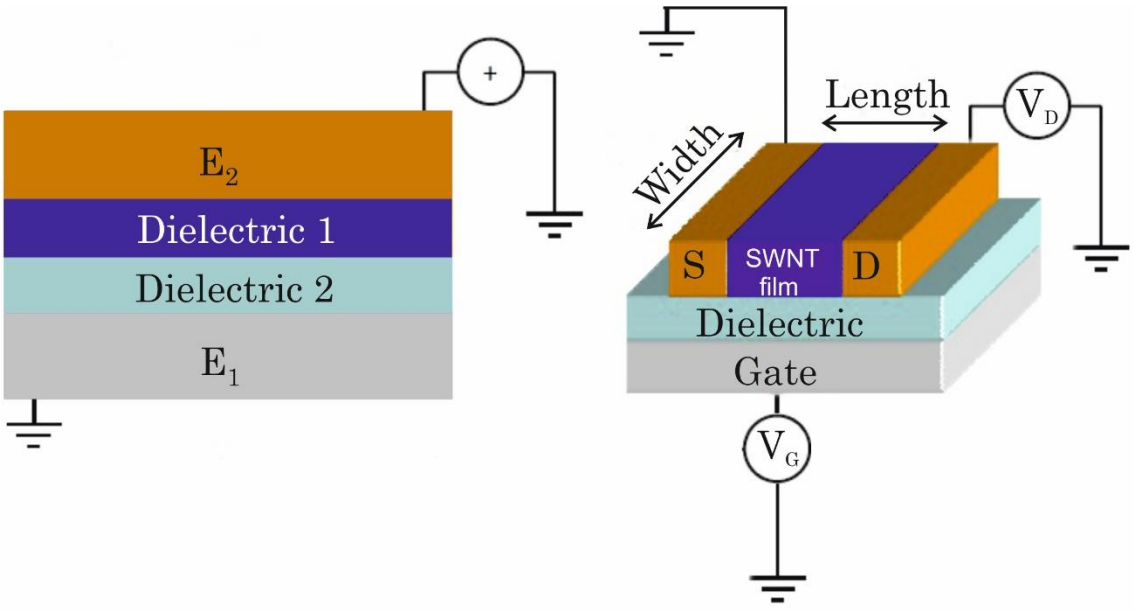

Figure 2.4: Representation of a parallel plate capacitor model (on the left) and real-life application of the model (on the right) of SWNT thin film transistors with bottom gate top contact geometry. S and D are the source and drain respectively. V_D represents drain voltage and V_G represents gate voltage.

Since nanotubes were first used in field effect transistors [7, 67], there has been a constant effort to improve device performance through optimizing key device parameters. The first parameter to be considered is the gate voltage, V_G. It is practically the operating voltage of the transistor. The gate voltage should be kept so high that the transistor reaches the maximum current in the channel (I_{SD}) and so low that prevents any damage in the gate oxide. Threshold Voltage (V_{th}) is the minimum voltage that can form a current flow between the source and the drain. This is not desired and to which extent the phenomena occurs is monitored via the Subthreshold Swing (SS). It is a parameter that indicates how effectively device turns off with the change in gate voltage:

$$SS = \ln 10 \ [\frac{dV_G}{d \ln I_{SD}}] \tag{2.16}$$

The theoretical minimum for the SS value is $k_B T \ln(10)$ = 60mV·decade^{-1}, arising from the thermal smearing of the Fermi distribution of the charge carriers in the device. [69–72].

Another device property is the ratio between the currents when the field effect transistor is on and when it is off. Values in the range of 10^3 to 10^6 are commonly seen for nanotube field effect transistors [44].

The most commonly used device parameter is the field effect transistor mobility, μ_{FET}, indicating the mobility of the charge carriers in the channel. According to gradual channel approximation of the drain current equation:

$$I_D = \frac{WC_i}{L} \cdot \mu_{FET} \cdot [(V_G - V_T) \cdot V_D - (\frac{V_D^2}{2})] \tag{2.17}$$

where W is the width and L is the length of the channel (distance between the source and drain electrodes) and C_i is the intrinsic capacitance, when $V_G > V_{th}$ and $V_G - V_{th} > V_D$, the field effect transistor operates like a resistor controlled by the gate voltage. The carrier mobility can be extracted directly from the transfer characteristics (I_D vs. V_G) in the linear regime:

$$\mu_{linear} = \left[\frac{\partial I_D}{\partial I_{V_G}}\right] \cdot \left[\frac{L}{WC_i V_D}\right] \tag{2.18}$$

and in the saturation regime:

$$\mu_{saturation} = \left[\frac{\partial^2 I_D}{\partial V_G^2}\right] \cdot \left[\frac{2L}{WC_i}\right] \tag{2.19}$$

3. Experimental

In the following chapter, sample preparation techniques are explained and corresponding characterization methods are overviewed in terms of their application for optical and electronic analysis of SWNTs. Instrumental details, as well as theoretical considerations for forthcoming analysis, are specified.

3.1 Dispersing SWNTs with π–conjugated polymers

As already mentioned in the introduction, in order to enrich and stabilize SWNTs, π–conjugated polymers were used as the dispersant for SWNTs.

For Chapter Four, six different π–conjugated polymers were introduced in order to selectively disperse CoMoCAT SWNTs. Towards understanding the wrapping tendency of each polymer, concentrations of *Poly*[(9,9–*dioctylfluorenyl*–2,7–*diyl*)–*alt*–*co*–(2,6–bi-*pyridine*)] (PFOBPy), *Poly[N–9′–heptadecanyl–2,7–carbazole–alt–6,6'diyl–2,2'–bipyridine]* (PCzBPy), *Poly*[(9,9–*dioctylfluorenyl*–2,7–*diyl*)–*alt*–*co*–(2,6–*phenyl*)] (PFOBPh), *Poly[N–9′–heptadecanyl–2,7–carbazole–alt–6,6'diyl–2,2'–biphenyl]* (PCzBPh) , *Poly*[(9,9–*dioctylfluorenyl*–2,7–*diyl*)–*alt*–*co*–(2,6–*bithiophene*)] (PFOT2) and *Poly[N–9′–heptadecanyl–2,7–carbazole–alt–6,6'diyl–2,2'–bithiophene]* (PCzT2) were varied. Next, in order to understand the effect of the SWNT soot on the dispersed chirality, PFOBPh was used as the dispersant for homegrown chemical vapor deposition (CVD) SWNTs (produced by Matthias Kastner) in comparison to the commercial (CoMoCAT®–SWeNT® SG65 Southwest Nanotechnologies) SWNTs.

For each set of experiment, 0.5, 2.5, 5, 10, 20, 50 and 70 mg polymer were mixed with 5 mg SWNTs in 10 ml toluene. The mixture was sonicated for 2 hours with a ½″ *Resonator* connected to a 5 mm *Microtip* with an output of 20% in order to determine the selectively through dispersed chiralities with each polymer. The resulting dispersion was divided into 1.5 ml Eppendorf tubes and centrifuged with a bench top centrifuge (Biofuge 15, Heraeus) at 14000 rpm for 4 min. After the collection of the supernatant, dispersions were ready for further spectroscopic investigation.

As a reference, chiralities that were originally present in the SWNT soot were determined by dispersing with Sodium Dodecyl Sulfate (SDS), as SDS does not show enrichment of any specific chirality in the dispersion but only stabilizes the present chiralities [165]. 5 mg of SWNTs was mixed with 10 ml of 1 wt. % SDS (Sigma Aldrich Purity ≥ 99%) water solution. Similar to the polymer dispersed SWNTs, after 2 hours of sonication at 0°C, benchtop centrifugation at 14000 rpm for 4 min was performed. The resulting supernatant was investigated with UV/vis and Photoluminescence Spectroscopies.

Chemical structures and specifications of the polymers used in chapter four can be found in Figure 3.1. Polymers PFOBPy (American Dye Source) and PFOT2 (Sigma Aldrich) were commercially available whereas PCzBPy, PCZBPh, PFOBPh, and PCzT2 were synthesized and electronically characterized by our cooperation partner, Rajesh Veeravarapu, from the research group of Prof. Jorge Morgado, at IT–Lisboa. Synthesis route for the polymers is shown in Figure3.2.

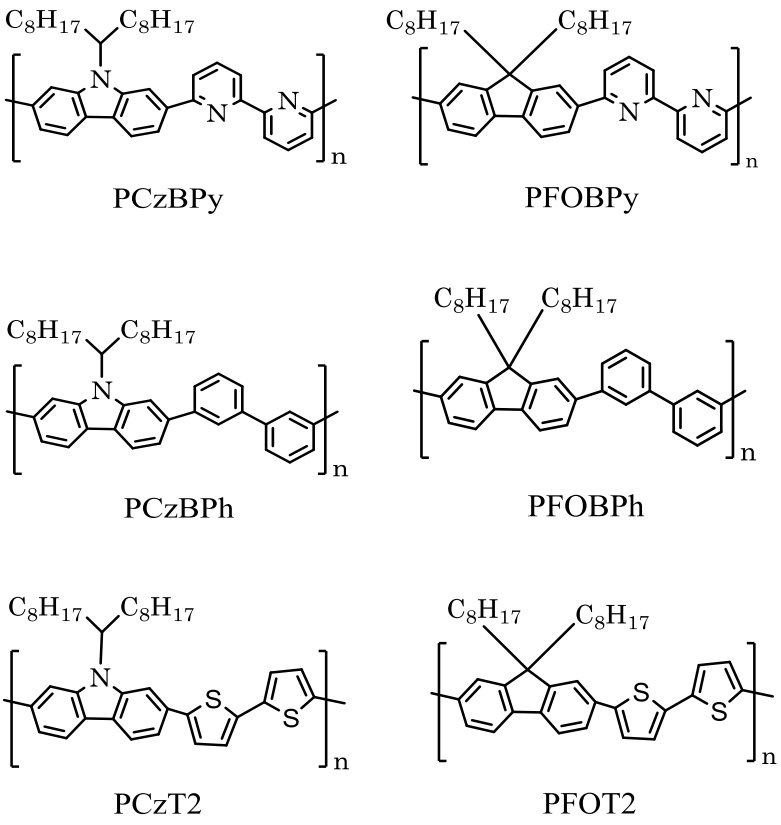

Figure 3.1: Chemical structures of the used polymers.

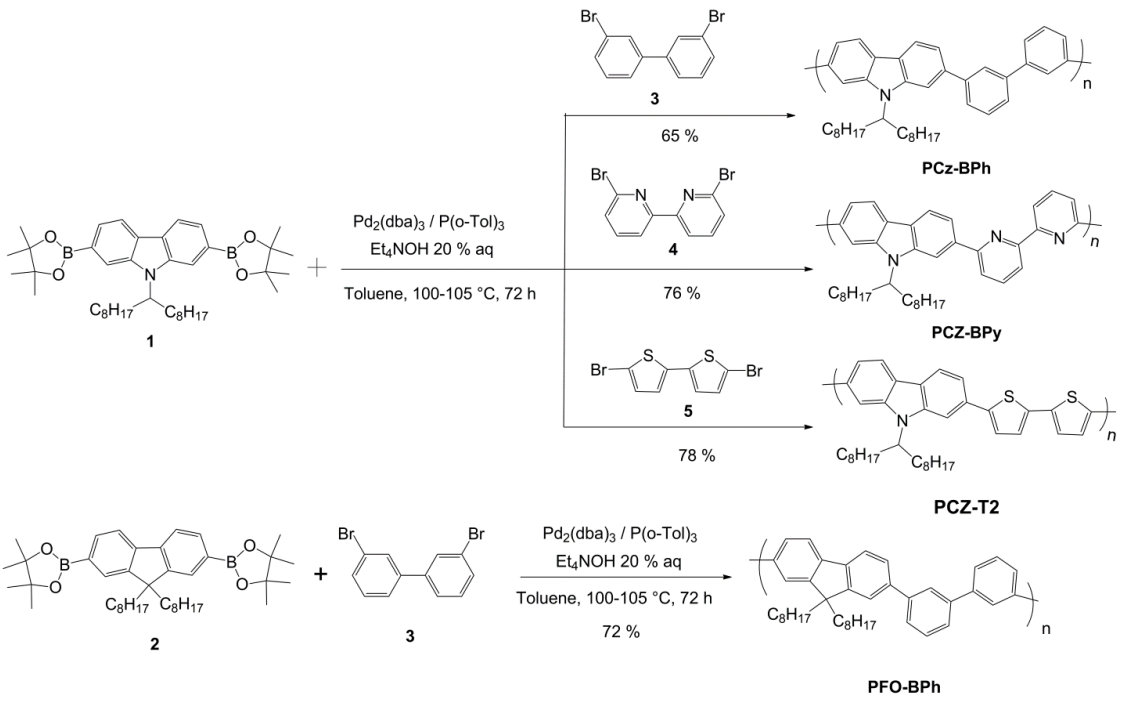

Figure 3.2: Synthesis of the polymers PCzBPh, PCzBpy, PCzT2, and PFOBPh.

Poly[N–9′–heptadecanyl–2,7–carbazole–*alt*–6,6'diyl–2,2'–bipyridyne] (PCz–BPy): Yield: 76%.) ^{1}H NMR (300 MHz, $CDCl_3$): δ (TMS, ppm) 8.71 (br, 2H), δ 8.51 (s, 1H), 8.32 (br, 3H), 8.05 (br, 6H), 4.8 (br, 1H), 2.52 (br, 2H), 2.12 (br, 2H), 1.25–1.45 (br, 27H), 0.75 (t, J = 7.12 Hz, 6H).Anal. Calcd for $C_{39}H_{47}N_3$ (%): C, 83.97; H, 8.49; N, 7.53. Found: C, 82.30; H, 8.34; N, 7.50. M_n=15800; M_w = 36900; PDI = 2.33.

Poly[9, 9–dioctylfluorenyl–2,7–*alt*–diyl–biphenyl] (PFO–BPh) :Yield: 82%. ^{1}H NMR (300 MHz, $CDCl_3$) δ (TMS, ppm) 7.98 (br, 2H), δ 7.83 (br, 2H), δ 7.64 (m, 10H), 2.07 (br, 4H), 1.32–1.12 (br, 22H), 0.75 (br, 6H), 0.79 (t, J = 6.96 Hz, 6H). Anal. Calc. for $C_{41}C_{48}$ (%): C, 90.64; H, 9.03. Found: C, 89.65; H, 9.03. M_n=6000; M_w = 14500; PDI = 2.41.

Poly[N–9′–heptadecanyl–2,7–carbazole–*alt*–6,6'diyl–2,2'–biphenyl] (PCz–BPh): Yield: 76%. ^{1}H NMR (300 MHz, $CDCl_3$): δ (TMS, ppm) 8.21 (br,

2H), δ 8.04 (br, 2H), 7.82–7.55 (m, 10H), 4.75 (br, 1H), 2.42 (br, 4H), 2.02 (br, 2H), 1.25–1.14 (br, 25H), 0.75 (t, J = 9 Hz, 6H). Anal. Calc. for $C_{41}H_{49}N$ (%): C, 88.59; H, 8.88; N, 2.52. Found: C, 87; H, 9.05; N, 2.50. M_n=12900; M_w = 57900; PDI = 4.49.

Poly[N–9′–heptadecanyl–2,7–carbazole–*alt*–5,5'diyl–2,2'–bithiophene]:
Yield: 63%. ^{1}H NMR (300 MHz, $CDCl_3$): δ (TMS, ppm) 8.11 (br, 2H), δ 7.82 (br, 1H), 7.605 (br, 4H),7.39 (br, 3H), 4.8 (br, 1H), 2.52 (br, 4H), 2.12 (br, 2H), 1.25–1.45 (br, 27H), 0.75 (t, J=7.22Hz, 6H). Anal. Calc. for $C_{38}H_{47}N_2S_2$ (%): C, 78.16; H, 8.46; N, 2.40; S, 10.98. Found: C, 76.23; H, 7.42; N, 2.24; S, 10.10. M_n=33800; M_w = 59100; PDI = 1.70.

The electrochemical properties of the polymers in the solid film were investigated by our cooperation partner, Rajesh Veeravarapu, from the research group of Prof. Jorge Morgado, at IT–Lisboa. Cyclic voltammetry measurements were performed in a Solartron potentiostat using 0.1 M tetrabutylammonium tetrafluoroborate ($TBABF_4$)/CH_3CN supporting electrolyte, at a scan rate of 50 mVs^{-1}. A saturated calomel reference electrode calibrated against ferrocene, Fc/Fc^+ (0.42 V), a platinum wire as a counter electrode and a platinum disk as working electrode were used. The polymer was dissolved in toluene and drop cast onto the working electrode. The HOMO and LUMO energies were estimated from the onset values measured for the oxidation and reduction processes, respectively, after reference to the vacuum level. As the energy level of Fc/Fc^+ is at 4.80 eV below the vacuum level we calculate HOMO (eV) = – ($E_{onset,ox}$ (eV) + 4.38) and LUMO (eV) = – ($E_{onset,red}$ (eV) + 4.38). As the anodic and cathodic peaks are not fully reversible, fresh films were used for the oxidation (anodic) and for the reduction (cathodic) scans.

Table 3.1: Absorption, and photoluminescence peaks' central wavelengths, HOMO and LUMO energy levels for the polymers used in the study.

	λ_{abs} (nm) Soln	λ_{em} (nm) Soln	λ_{abs} (nm) Film	λ_{em} (nm) Film	E_{HOMO} (eV)	E_{LUMO} (eV)
PFOBpy	354	378	370	350	−5.80	−2.90
PCzBpy	334	421	383	426	−6.53	−2.34
PFOBPh	330	380	332	494	−5.97	−2.50
PCzBPh	328	402	355	432	−5.42	−2.48
PCzT2	456	533	474	562	−5.42	−2.60
PFOT2	447	510	455	550	−5.50	−3.10

For studying the optical and electronic properties of SWNT films, PFOBPy was used in order to selectively disperse (6,5) SWNTs from a CoMoCAT soot. In order to prepare PFOBPy wrapped (6,5) SWNTs, 100 mg CoMoCAT SWNTs (SWeNT® SG65 Southwest Nanotechnologies) were mixed with 200 mg PFOBPy (American Dye Source) and suspended in 200 ml toluene(AnalaR NORMAPUR®, VWR Purity ≥ 99.5%) The mixture was sonicated inside a 300 ml rosette vessel (G. Heinemann) with a *¾″ High Gain Horn* (Branson Sonifier II W−450, Output=40%) at 0°C. Apparatus can be shown in Figure 3.3. After 14 hours, the mixture was transferred into 50 ml Falcon tubes and centrifuged for 30 min at 4000 rpm in a bench top centrifuge (Rotina 35R). Resulting supernatant contained PFOBPy wrapped (6,5) SWNTs with an excess of polymer whereas impurities, large aggregates, and metallic SWNTs precipitated at the bottom of the falcon tube.

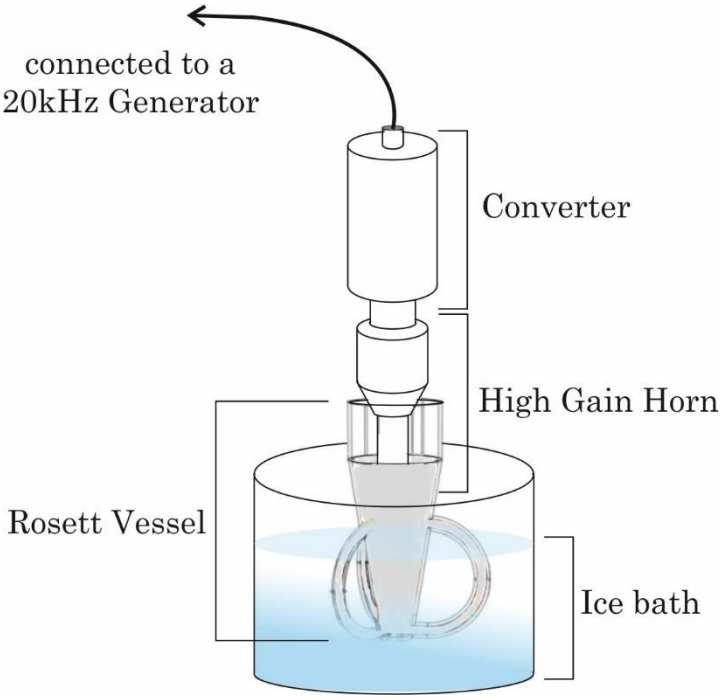

Figure 3.3: Apparatus for dispersing SWNTs in toluene via sonication and stabilization of single SWNTs with polymer π– π interactions, so-called polymer wrapping.

3.2 Vacuum Filtration and Wet Film Transfer

Thin film production is an important part of this study. In order to produce homogeneous thin films with controllable thickness, vacuum filtration wet thin film transfer was introduced for polymer dispersed SWNTs.

PFOBPy wrapped SWNT suspension was prepared as explained in Section 3.1. The optical density of the S_1 transition of (6,5) SWNTs of the supernatant was found to be 5. Absorption and photoluminescence spectra of the suspension can be seen in Figure 3.4. The horizontal axis of the spectrum was divided into two using different scales for optical density. The optical density of the polymer was found to be almost an order of magnitude higher than optical density of the S_1 transition of the dispersed SWNTs. In order to reduce the polymer concentration, the suspension was

vacuum filtered through a nitrocellulose membrane with 0.1 µm pore size (*IsoporeTM Membrane Filters 0.1 µmVCWP, Merck Millipore*). Remaining network of polymer-wrapped SWNTs on top of the membrane was rinsed with 5 ml toluene under vacuum.

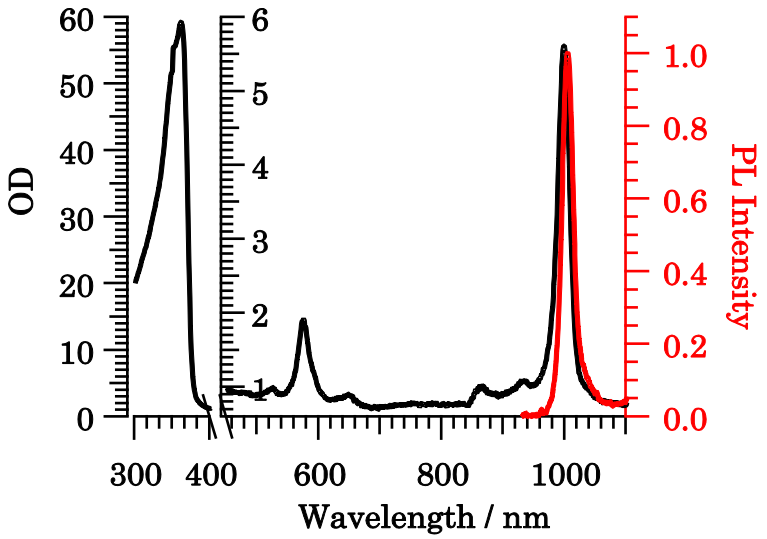

Figure 3.4: Absorption (black) and photoluminescence (red) spectra of the dispersion prepared from 200 mg PFOBPy and 100 mg CoMoCaT SWNTs.

In order to produce homogeneous thin films with scalable thickness, wet film transfer technique for polymer wrapped SWNTs was introduced. Here, the procedure from the work of Wue et. al. was modified and used for polymer wrapped SWNTs [141]. This adaptation enabled the production of PFOBPy wrapped (6,5) SWNT films with a scalable thickness on various substrates efficiently. Optical and electronic properties of the produced films were examined with absorption, photoluminescence and field effect transistor measurements.

In the wet film transfer, the substrate of choice (glass for optical measurements at room temperature, sapphire for optical measurements at low temperatures and SiO_2 for electronic measurements) was wetted with toluene. The vacuum filtrated network of SWNTs on top of cellulose membrane was placed and pressed upside down on the substrate so that SWNTs adhere on the surface. Samples were let dry for 30 min at 100°C and immediately transferred into an acetone bath in order to dissolve the cellulose filter. After 5 consecutive acetone baths, the cellulose filter was dissolved (confirmed by AFM and SEM measurements in Chapter Five) and films were ready for the optical or electronic measurements. With this technique, the thickness of the film can be varied with the amount of dispersion filtered through the membrane, which was demonstrated by changing the filtrate volume in the range of 0.25 to 12 ml.

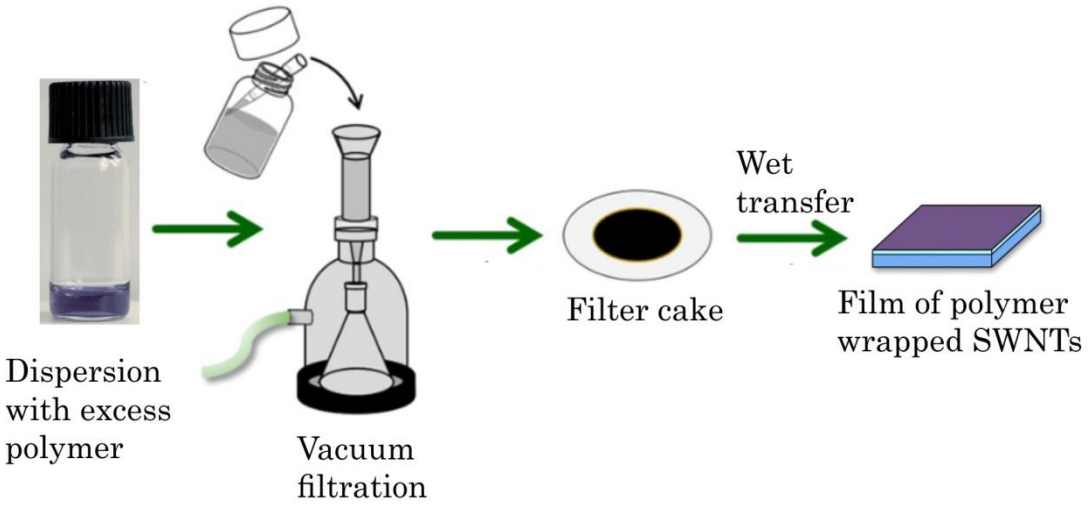

Figure 3.5: The thin film preparation process.

3.3 UV–Vis–NIR Absorption Measurements

Polymer wrapped SWNTs, which were dispersed in toluene, were analyzed first by UV–nIR–vis spectroscopy to identify the change in concentrations of dispersed chiralities. A range of 400 to 1400 nm was scanned in order to observe the difference of intensity, width, and the central wavelength of S_{11} (900–1400 nm) and S_{22} (550–900 nm) transition peaks of dispersed SWNTs. Dispersions were measured in square cuvettes with 2 mm path length for polymer concentrations in the range of 0.05 to 7 mg ml^{-1}. Here, the polymer concentration is referred as the concentration present in the dispersion during ultrasonication and will be used accordingly from now on.

Absorption spectra of dispersions, as well as thin films in ultraviolet, visible and near infra–red region, were taken using Cary 5000–Spectrometer (*Varian, Agilent*). The spectrometer contains a deuterium lamp for measurements in the UV region and a halogen lamp for the measurements in the visible region. At around 800 nm, there is a change in the detector, grid, and filter which happens to be in the region of interest for the conducted measurements.

Dispersions were measured inside quartz micro cuvettes with a thickness of 10 mm (*105.250–QS, Hellma Analytics*). Taking the saturation levels of detectors into consideration, dispersions were diluted with a solvent in order to reach the full dynamic range of resolution. For every measurement corresponding solvent spectrum is taken in the same spectral region with same conditions and subtracted from the dispersion spectrum.

SWNT films on glass or sapphire are fixed on the film holder apparat of the spectrometer via two-sided tape and the light path passing through the film was having a diameter of 1 cm.

3.4 Photoluminescence Measurements

The setup used for photoluminescence excitation measurements for SWNT dispersions and thin films is shown in Figure 3.6. A supercontinuum white light source (*SuperK EXTREME EXR−15, NKT Photonics*) was used which was composed of a pulsed Nd: YAG−Laser and a nonlinear glass fiber. The wavelength was varied via a filter module (*SuperK Varia, NKT Photonics*). In order to block the excitation light, a NIR filter was integrated. The laser power for the excitation light intensity was held at 80 % at all times. The correction for the variance of the excitation power along the map was performed through measurements made on a glass substrate placed on the light path (*S120C/PM100A, Thorlabs*). The light was collected on a 10x objective and emitted light from the dispersion in the cuvette was probed perpendicular to the excitation light and passed through a parabolic mirror (*f =2"*), silver mirror and another parabolic mirror (*f =4"*) in order to reach the Spectrograph (*Shamrock 303i−B, Andor*). The detection of the signal was either with an InGaAs photodetector (iDus DU491A, Andor) or a Si−CCD photodetector (Newton DU920P, Andor) depending on the emission wavelength to be monitored. Measurements were performed with the detector at −80°C in order to increase the efficiency of the detectors for the selected wavelength range [45, 46]. A long pass filter (900FH90) was integrated into the setup in order to block the scattered excitation light.

Integrating different modules enables the measurement of dispersions, thin films and thin films at low temperature at the same setup. For low−temperature PLE Measurements on SWNT thin films, films were placed inside the low−temperature module: an isolated capsule connected to a cryostat (down to 7 K) under high vacuum. The low−temperature module was held 45° to the excitation light in order to minimize the light scattering. For thin film measurements at room temperature, cryostat was disconnected and the films were measured in stable room temperature.

The PLE Maps were taken using the LabView interface that was created by Tilman Hain, Matthias Kastner, and Daniel Zuleeg. The excitation wavelength was varied in the range from 450 to 800 nm and emission is recorded with a wavelength range from 900 to 1250 nm for Si–CCD and InGaAs detector with an integration time of 2s per spectrum using a 4 cm bandpass. Slit width was adjusted to 200 µm, a grid with 150 lines.µm^{-1} and blaze wavelength of 1250 nm was used.

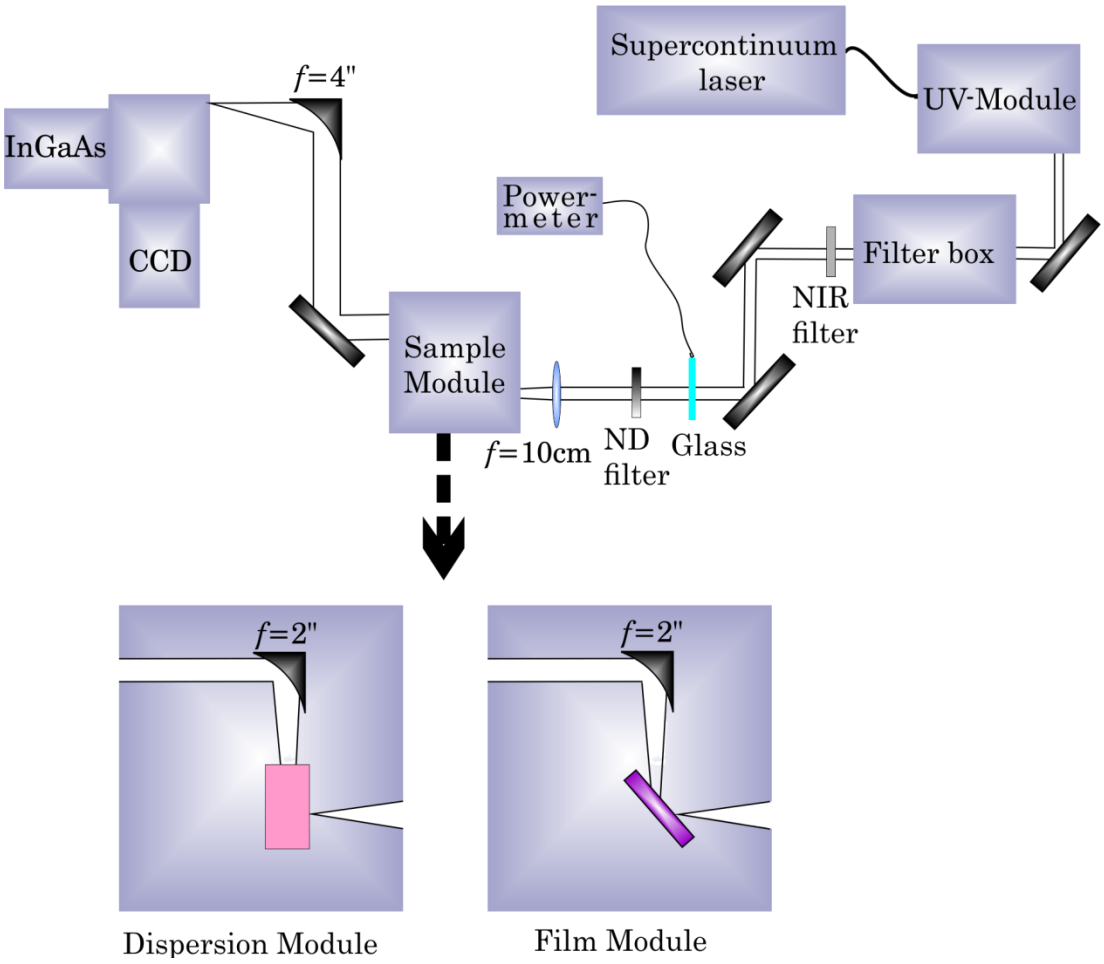

Figure 3.6: Setup for dispersion and film photoluminescence excitation spectroscopy measurements.

For chapter four, in order to find out the species present in the CoMoCAT raw material, 5 mg SWNTs were dispersed in 1 wt % SDS solution. Resulting dispersion was investigated as explained above with PLE and spectroscopy. In total, 11 different semiconducting SWNTs were observed in the soot [80–82]. These chiralities were: (9,1), (8,3), (7,3), (6,5), (7,5), (7,6), (8,4), (8,6), (9,2), (9,5) and (8,7).

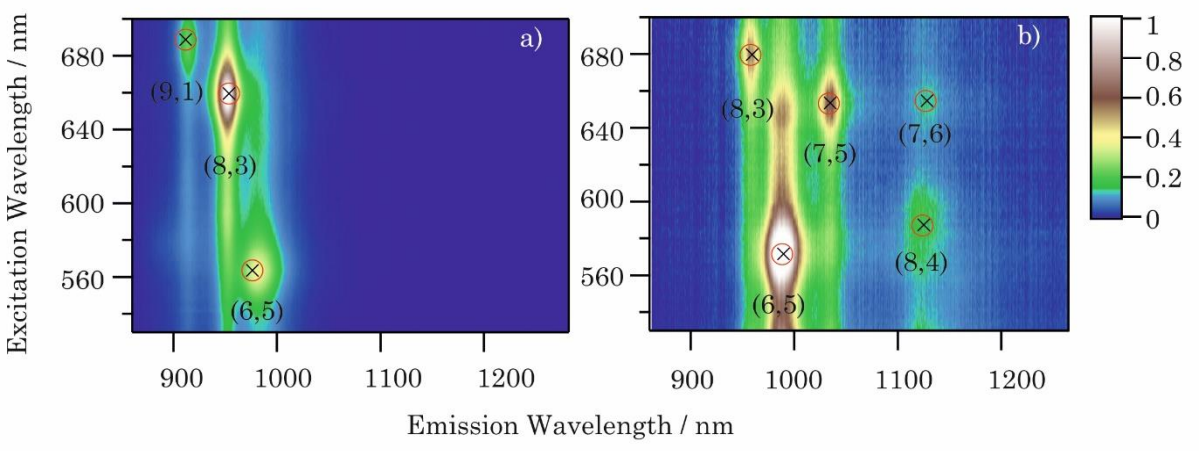

Figure 3.7: Photoluminescence excitation-emission maps of sodium cholate dispersed carbon nanotubes from CoMoCAT raw material. a) Measured with a CCD detector b) Measured with an InGaAs detector. Photoluminescence intensities are normalized for both detectors. 5 different chiralities are dominantly observed in addition to other 6 [80, 81].

3.5 Device Architecture and Preparation of (6,5) SWNT Field Effect Transistors

Fabrication of the transistors, as well as measurements of current-voltage characteristics, were performed at the lab of Prof. Thomas Anthopoulos in Imperial College London, UK, in collaboration with Francesca Bottacchi. Further information regarding the fabrication procedure and measurement setup can be found in Reference 138 and 151.

Bottom–gate top contact transistors were fabricated by wet transfer of vacuum filtration films of PFOBPy wrapped (6,5) SWNTs. The volume of SWNT suspension was varied between 0.25 to 1.75 ml to produce films with thicknesses between 8±5 and 80±5 nm. Thermal grown SiO_2 (100 nm thickness) was chosen as a dielectric layer as the best performance in terms of charge carrier mobility was achieved with high capacitance gate dielectrics [132]. The doped Si substrate beneath the SiO_2 was used as the back gate, which may effectively modulate the carrier concentration in the channel and in the region near the metal/semiconductor CNT interface. These substrates were sequentially cleaned by ultrasonication in acetone and in isopropyl alcohol baths for 5 minutes each and exposed to UV–ozone for 20 minutes before the SWNT films were applied. Source and drain electrodes were chosen to be gold according to its high work function and the nearly ohmic contact it produces with SWNT thin films [152]. 40 nm Au were deposited via thermal sublimation in high vacuum. Figure 3.8 shows the schematic of the resulting transistor architecture.

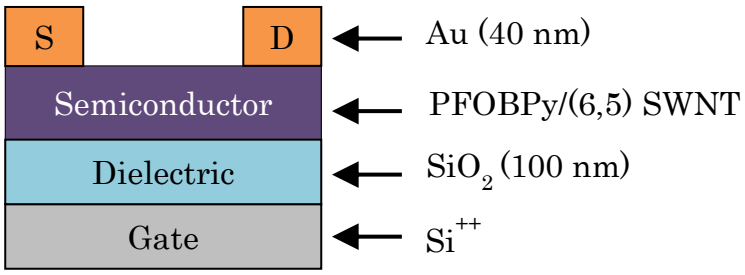

Figure 3.8: Schematic of the bottom gate top contact field effect transistor fabricated on a Si^{++}/SiO_2 substrate.

4. Insights into Polymer Wrapping

4.1 State of the Research and Purpose of this Study

Since their discovery, single-wall carbon nanotubes (SWNTs) have been considered as promising materials to be used in active layers of photovoltaic devices or thin film transistors due to their remarkable light absorption and charge transport characteristics. However, the implementation of these applications has been constrained by various problems as it is already mentioned. These problems can be summoned under two major titles: All known synthesis methods produce polydisperse SWNTs containing both metallic and semiconducting species and debundling SWNTs in an efficient way without affecting their electronic structure is not trivial.

Methods for solving these problems include either covalent functionalization of produced SWNTS or sorting of SWNTs in solution with non−covalent dispersing agents. Each sorting method has its own limits in terms of the purity, complexity, electronic or chiral selectivity of the obtained SWNTs, dispersion efficiency, process scalability and feasibility in terms of time and cost.

The biggest disadvantage of covalent functionalization is the altering of semiconducting SWNTs' electronic structure and hindering their promising electrical properties.

Noncovalent interactions between SWNT surface and noncovalent functionalization agents can be enthalpy driven such as π−π, CH−π, NH−π or entropy driven interactions such as hydrophobic interactions using surfactants. Surfactants like sodium dodecyl sulfate (SDS) [47–49], sodium dodecylbenzene sulfonate (SDBS) [50–54], sodium cholate (SC) [55–57],

cetyltrimethylammonium bromide (CTAB) [52, 58], Brij [52, 57], Tween [52, 57] and Triton X [50, 52, 57, 59] have typically been used [56]. In the case of surfactant-assisted dispersion of SWNTs, typically an extra step of separation (Ultracentrifugation [60, 62], gel chromatography [61,63], partition separation [64,65]) is needed for obtaining pure, monochiral, semiconducting SWNTs.

Among all methods, polymer wrapping offers a relatively inexpensive, time effective and straightforward way to selectively disperse SWNTs. Use of conjugated polymers as the wrapping agent enables endless possibilities to innovate in polymer design. Conjugated polymers show great potential with their ability to not only disperse SWNTs in various aqueous and organic solvents via π−π interactions but also to purify them. The challenge to be faced is to extract semiconducting SWNTs in a specific chirality range with high dispersion efficiency without shortening the lengths of individual SWNTs and introducing defects in the nanotube structure which can be overcome only with the right choice of polymer and optimized process parameters.

There are several conjugated polymer families including polyfluorenes, polythiophenes, polycarbazoles, polyphenylenes etc. that have been considered as SWNT wrapping agents. Polyfluorenes are the polymers that were first shown to selectively disperse almost a single semiconducting chirality by polymer wrapping in an organic solvent [12, 13].

Later on, up to 98% selectivity of (6,5) SWNTs were reached by Ozawa et. al, using another fluorene containing random copolymer: PFOBPy [14]. In this publication, the dependence of chiral selectivity and dispersion efficiency of the wrapping polymer on the choice of solvent was investigated. This investigation was focusing mainly on the density and polarity of the solvents and their effects. Among others [15, 16], Jakubka et. al. brought a comprehensive understanding for the dependence of polymer chiral selectivity on preferred solvent by emphasizing the

importance of difference in solvent viscosity. They used PFOBPy and F8BT as wrapping agents and their understanding was considering the molecular weight of the polymer as an important factor that affects the viscosity of the dispersion [17, 23]. It was demonstrated with F8BT that selective behavior of the polymer changes with an increasing polymer weight, emphasizing the importance of having resembling molecular weights for polymers in comparative studies.

Polymer concentration or the effect of a change in the ratio of the polymer concentration to the SWNT concentration has been investigated as it influences both sorting yields of the semiconducting SWNTs in the final dispersion and its chiral content [18–21]. Although results of these studies provided an insight about the polymers that were in focus, a throughput analysis that unfolds effects of the polymer structure on the obtained spectra in a systematic manner for a wide polymer concentration range is still missing.

Differing compositions of SWNT dispersions changing the SWNT raw material and role of raw material on the dispersed species has been studied only by a few researchers. For laser ableviated SWNTs, Mistry et. al. communicated about a comparison at different temperatures [18]. In addition to that, Rice et. al. studied HiPCO and CoMoCAT nanotube samples wrapped with a polymer and monitored dispersed chiralities for each case [22]. More information can be reached by comparing different publications that use the same polymer with different SWNT soot [14, 18]. In this case, details about material processing which determine the end dispersion become of extreme importance as they should be identical in order to draw unsusceptible conclusions. Therefore such a comparison can be problematic. All and all, up to now it hasn't been clear if the difference in dispersed chiralities comes from the difference in production method (chemical or heat treatment during production, catalyst, conditions etc. affecting the interactions between SWNT and polymer) or simply from the chirality distribution of the raw material.

In comparison to polyfluorenes, polyphenylenes, and polythiophenes, polycarbazoles have received significantly less attention as nanotube dispersing agents. However, the synthetic availability of polycarbazoles to be easily derivatized from the nitrogen atom makes them unique candidates for preparing various polymers and alters the polymer band gap in order to obtain more favorable polymer–SWNT heterojunctions. Additionally, the incorporation of the nitrogen into the polymer backbone increases the π electron density and enables a stronger interaction between the SWNT and polymer. As a result, the dispersion efficiency is expected to be higher than the efficiency of the corresponding fluorene homolog that is lacking the nitrogen.

Not only the rigid components but also alkyl chains and copolymer units in the polymer backbone play an important role in the selectivity and dispersion efficiency of the polymer. There have been a great number of publications that systematically investigated the effect of changing alkyl chain length, concluding that larger diameter tubes can be dispersed with longer side chains [21, 78]. However, the design of polymers for investigation of the role of copolymer unit on selectivity and dispersion efficiency seems to be random up to now. There is a lack of systematic investigation of different copolymer units in order to monitor the effect on dispersed SWNTs.

In this chapter, systematic investigation of random polyfluorene and polycarbazole derivatives copolymerized with bipyridine, biphenyl and bithiophene for selectively dispersing semiconducting SWNTs from CoMoCaT and CVD raw materials are reported. The molecular weight of the used polymers and preferred solvent (toluene) for all dispersions are held constant. Absorption spectroscopy and PLE spectroscopy were used in order to characterize the dispersions. On dispersions with varying polymer concentration with a range from 0.05 to 7 mg/ml polymer, an investigation was held to disperse together with 0.5 mg/ml SWNTs in toluene. Effects of wrapping polymer structure and the choice of SWNT raw material are

studied in order to figure out the optimized combination of parameters for increased chiral selectivity, high electronic sorting ability and high de−bundling efficiency of wrapping polymers on SWNTs. Here, providing a thorough understanding of the effects of aforementioned factors on the chiral selectivity, electronic sorting ratio and dispersion efficiency of the polymer is aimed.

4.2 Difference of Polymer Backbone

4.2.1 Bipyridine Copolymers of Fluorene and Carbazole

a. Optical Absorption Spectroscopy of PFOBPy and PCzBPy wrapped SWNTs

UV–vis–nIR spectra of the dispersions, with PFOBPy concentrations ranging from 0.05 to 7 mg ml^{-1} can be seen in Figure 4.1.a. Spectra are dominated by (6,5) SWNTs, which appear at 998 nm. Next to the (6,5) absorption peak, there is another S_{11} transition around 1037 nm which is designated to (7,5) SWNTs.

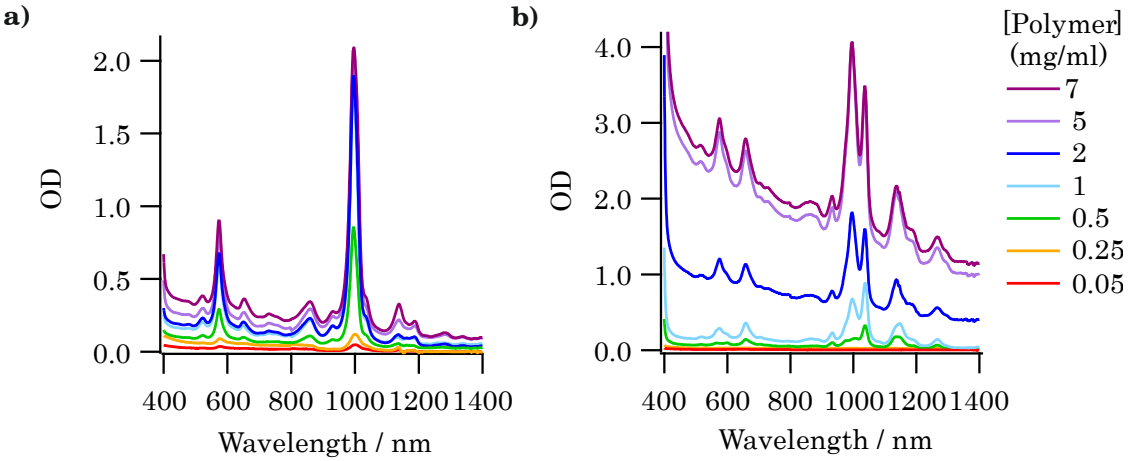

Figure 4.1: The optical absorption spectra of the SWNTs wrapped with a) PFOBPy and b) PCzBPy with a concentration range of each polymer from 0.05 to 7 mg ml^{-1}. Dispersions were prepared in toluene and corrections due to solvent absorption are already performed.

PCzBPy wrapped dispersions (Figure 4.1.b) are showing 4 distinct absorption peaks from semiconducting SWNTs. These are; (9,1), (8,3), (6,5) and (7,5). Peaks corresponding to the S_{11} transition of these chiralities are located at 935, 975, 997, 1037 nm respectively.

Underneath resonant transition peaks of PCzBPy wrapped SWNTs, there is an almost featureless background, which is more apparent for high polymer concentrations (between 2 to 7 mg ml^{-1}). It may be caused by the spectral congestion of semiconducting species. Elevation of the background might have been enhanced by aggregation of nanotubes due to the more favorable polymer–polymer interaction in high concentrations [20]. Another reason for large backgrounds may be metallic tubes that are present inside small bundles. They may cause some spectral elevation below 600 nm and also at longer wavelengths than 1000 nm due to the tail of π – plasmon resonance which is more enhanced for metallic SWNTs [82].

In order to find out the concentration of each SWNT dispersed, Voigt line shapes are fitted to the absorption peaks corresponding to the S_{11} transitions of stated SWNTs and the area under curves are integrated (Figure 4.2).

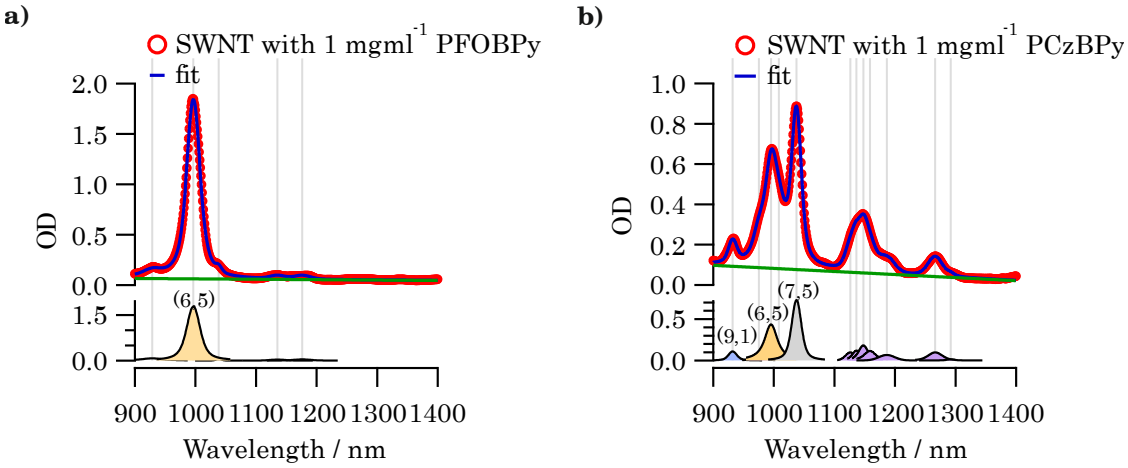

Figure 4.2: Voigt line shapes fitted to the optical absorption spectra of a)PFOBPy and b) PCzBPy wrapped SWNTs for polymer concentration of 1 mg ml^{-1}.

Integrated carbon SWNT optical cross section reported by Schöppler et. al. [104] is used in order to calculate carbon concentration per each dispersed chirality, using the formula:

$$C_c = \frac{\Delta_{FWHM} OD}{fd} \tag{4.1}$$

where d is the optical cell thickness and f is the C–atom oscillator strength which is calculated to be 0.010 and 0.006 for S_1 and S_2 exciton transitions respectively. Constant B is taken as $5.1 \cdot 10^{-8}$ mol L^{-1} cm nm^{-1} in order to calculate C_c in mol L^{-1}. Multiplication of C_c with the molar weight of carbon will give the [C] in μg ml^{-1}.

In both PFOBPy and PCzBPy wrapped SWNT dispersions, the evaluation of single chiralities from the absorption spectra in the range between 1100 and 1400 nm might be misleading due to the congestion in the spectra, especially for low polymer concentrations (Figure 4.1). Therefore, the dispersed carbon concentration for chiralities present in this spectral range is expressed as a sum and plotted separately.

At the first glance to Figure 4.3.a, it is clear that PFOBPy is selective for (6,5) SWNTs. With 1 $mgml^{-1}$ polymer, carbon concentration for (6,5) SWNTs reaches a plateau. On the other hand, the concentration of (7,5) and larger diameter tubes continue to increase. Therefore, according to optical absorption spectra, optimum concentration of PFOBPy to selectively disperse (6,5) SWNTs is around 1 mg ml^{-1}. The selectivity of (6,5) tubes can be explained by the tendency of PFOBPy to disperse this specific diameter of the SWNTs. However, a diameter dependent tendency would have resulted with equal dispersion tendency of (9,1) SWNTs, which has the same diameter with (6,5) SWNTs. According to Ozawa et. al., the absence of chirality (9,1), may suggest that two parameters, the diameter and the chiral angle of the SWNTs play a role in the selective dispersion and chiral angle of the SWNT is a more dominant selection rule.

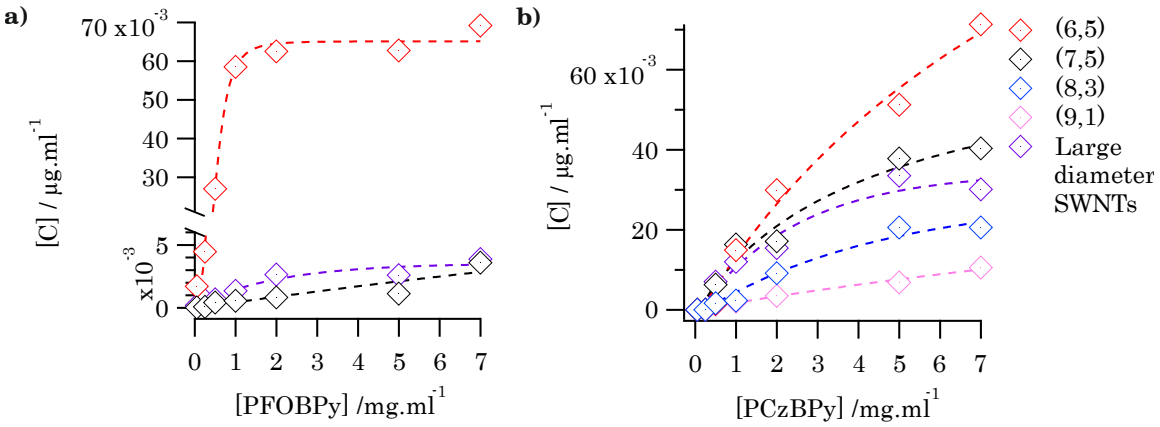

Figure 4.3: Concentration of dispersed carbon for each SWNT chirality between 900 and 1100 nm with increasing polymer concentration for a)PFOBPy and b)PCzBPy. Carbon concentration for each chirality has an exponential fit shown with a dashed line.

For PCzBPy dispersed SWNTs, there is no chirality whose concentration saturates in the range of investigation. Carbon concentration for each chirality increases exponentially with increasing polymer concentration, suggesting that the plateau for the concentration of the SWNTs wrapped with PCzBPy is to be seen for concentrations larger than 7 mg·ml^{-1}.

Comparing the concentration of the larger diameter SWNTs, PCzBPy tends to disperse almost 10 times more of large diameter SWNTs than PFOBPy. Considering the polydisperse nature of dispersions in almost every polymer concentration, PCzBPy shows a high dispersion efficiency but low selectivity in wrapping SWNTs. This result is also agreeing with the previous work from Lemasson et. al. [102] who suggests that the sp^2 hybridization of the N–bridging atom, different from the sp^3 hybridized C–bridging atom in fluorine unit, reduces the steric hindrance of that position. Selectivity of the fluorine unit is therefore disturbed, resulting in highly polychiral dispersions with PCzBPy.

b. Photoluminescence Excitation Spectroscopy of PFOBPy and PCzBPy wrapped SWNTs

PLE measurements were performed for polymer concentrations from 0.05 to 7 mg ml^{-1}. PLE Maps taken from 1 $mgml^{-1}$ PFOBPy and PCzBPy dispersions are shown in Figure 4.4, which holds features that represent all 7 maps for each polymer. Peaks corresponding to (6,5), (7,5), (7,6) and (8,6) are denoted on the map for PFOBPy wrapped tubes whereas (9,1), (8,3), (6,5), (7,5), (9,4), (8,4), (7,6), (9,2) are present chiralities wrapped with PCzBPy. Detailed peak positions of major PL peaks of the two samples are in good agreement with (n,m) indices assigned by Bachilo et al [81].

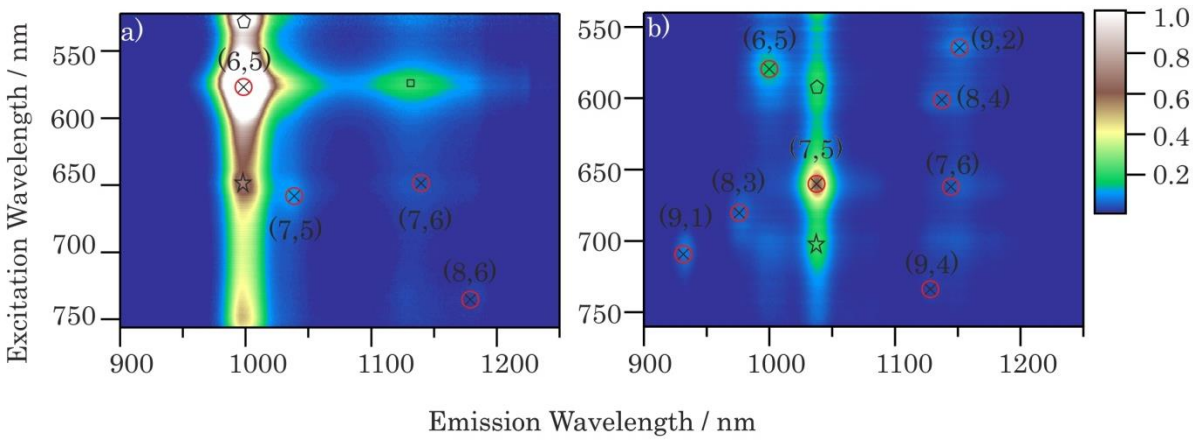

Figure 4.4: PLE maps for 1 $mgml^{-1}$ a) PFOBPy and b) PCzBPy wrapped SWNT dispersions with features representing their entire set. Peaks corresponding to the S_{22} of the semiconducting SWNTs are denoted with red circles, with excitation and emission wavelengths fitted for each polymer in reference to the previously published work [81]. Pentagons are representing E_{22-G}, and stars are representing E_{12-21} emissions. Intensity differences caused by detector changes are corrected and maximum photoluminescence intensity is normalized to 1 for each PLE map.

PL features, marked with a red circle are related to optical excitations that are polarized parallel to the SWNT axis. In this case, optical absorption

between sub-bands having the same quasiangular momentum is allowed, resulting in E_{22} transitions shown in Figure 4.4. Transverse photoexcitations ($E_{12,21}$) on the other hand, which are allowed for perpendicularly polarized light with respect to the SWNT axis are for absorption between the first and second subbands. These are having an intensity of about one-tenth of the corresponding E_{22} transition, similar to the results already reported [84–86].

In the PLE maps, phonon-assisted emissions or so-called excitation satellites (E_{22-G}) denote Raman active normal vibrational modes in SWNTs which are marked with a pentagon. These photoexcitations are characteristic low intensity PL features for ensembles of dispersed SWNTs [85–94] and are obvious for the major chiralities.

Two sidebands near the bright $^1E_{11}$ singlet exciton, one absorptive sideband ~200 meV above, and one emissive sideband ~140 meV below the bright singlet exciton has been well recognized and studied in the literature [91–97]. The phonon sideband above the E_{ii} levels was first predicted by Perebeinos et al. [91] as a result of strong coupling between dipole–forbidden excitons above the E_{11} level and *K*–point phonons. As dark (6,5) E_{11} K–momentum exciton and *K*–point phonons couple, dark excitons also scatter into the bright excitonic state at q=0, causing the appearance of this bright phonon sideband [95–97] like in Figure 4.4.a, where it lies below the bright $^1E_{11}$ singlet exciton.

Next, a photoluminescence spectrum is extracted for each SWNT chirality from the cross sections of measured PLE maps at the corresponding excitation wavelength. Areas under the curves are calculated by fitting Voight shaped peaks on the measured spectrum in order to find photoluminescence intensity and peak width for every dispersed chirality.

Resulting integrated photoluminescence intensities with increasing polymer concentrations can be seen in Figure 4.5 with fits of:

$$y = y_0 + Ae^{\left\{\left(\frac{-x}{\tau}\right)\right\}} \quad (4.6)$$

represented with a dashed line. For both polymers, present SWNTs tend to have increasing photoluminescence until the polymer concentration reaches around 2 mg ml^{-1}. Afterwards, saturation in photoluminescence is almost at the same point for all chiralities. This phenomenon is already seen in literature for another polymer [20]. It is most apparently observed for PFOBPy wrapped (6,5) SWNTs and PCzBPy wrapped (6,5) and (7,5) SWNTs in Figure 4.5a and b. For polymer concentrations higher than 2 mg ml^{-1}, where metallic tube concentrations may become detectable, constant photoluminescence intensity of dispersed semiconducting SWNTs may be attributed to an enhancement in PL quenching.

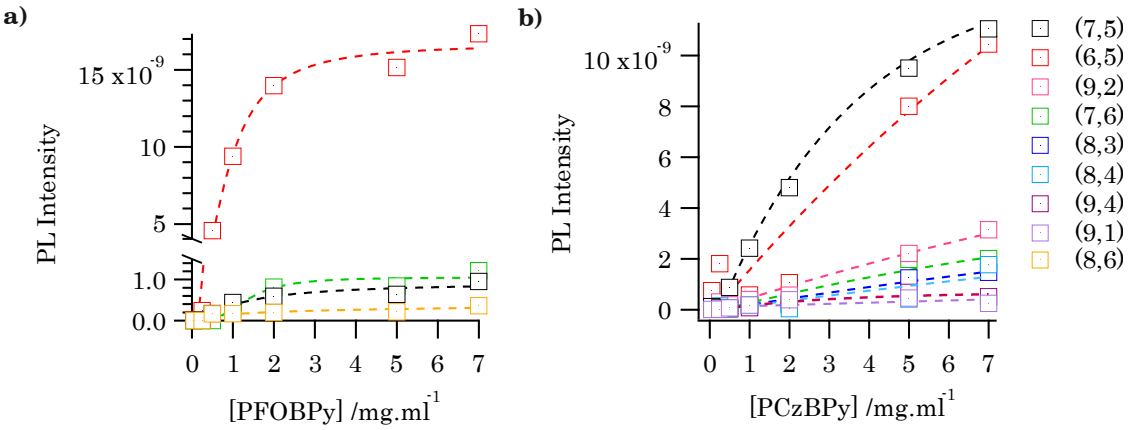

Figure 4.5: PL Intensity for each chirality plotted as a function of polymer concentration for a) PFOBPy and b) PCzBPy. Data (squares) is fitted with equation 4.6 which is represented by dashed lines for each chirality.

c. Photoluminescence Quantum Yield

In order to quantify and compare photoluminescence quantum yield for semiconducting SWNTs wrapped with polymers, the area under the photoluminescence peak is divided by the optical density, representing the photoluminescence quantum yield (PLQY), which can be expressed as:

$$\text{PLQY} = \frac{I_{PL} FWHM}{OD} \tag{4.7}$$

where I_{PL} is the photoluminescence intensity, OD is the optical density and FWHM is the width of photoluminescence peak for each chirality.

When common chiralities in the dispersions of both polymers are compared, it is seen that PLQY is slightly higher for the ones that are wrapped with PFOBPy, which might be pointing out a higher debundling efficiency for PFOBPy. On the other hand, increasing metallic tube concentration might as well be a factor that lowers the PLQYs of PCzBPy wrapped SWNT dispersions.

As seen in Figure 4.6, saturation in the PL intensity reproduces itself in the PLQY which makes the optimum concentration of wrapping polymer to be smaller than or equal to 2 mg ml^{-1}.

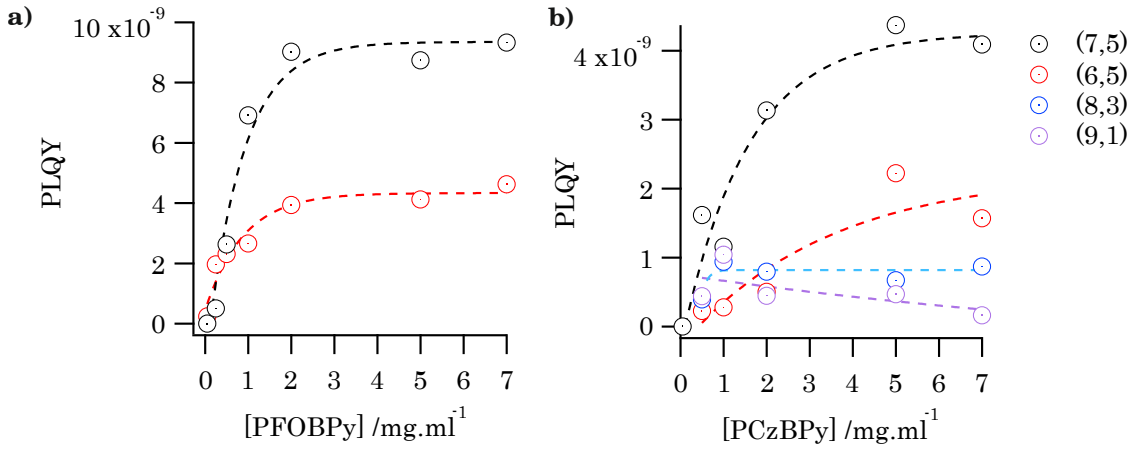

Figure 4.6: Relative photoluminescence quantum yield with increasing polymer concentration. Circles represent calculated PLQY for each concentration using formula (4.7) and an exponential fit according to Equation (4.6) for each chirality shows the evaluation of the PLQY.

4.2.2 Bithiophene Copolymers of Fluorene and Carbazole

a. Optical Absorption Spectroscopy of PFOT2 and PCzT2 wrapped SWNTs

UV–vis–nIR absorption spectra for PFOT2 wrapped dispersions contain four different semiconducting SWNTs appearing distinctly in the absorption spectra. These are (7,3), (8,3), (6,5) and (7,5) whose S_{11} transitions appear around 932, 975, 1000 and 1050 nm, respectively. Their corresponding S_{22} transitions, which should have appeared between 600 and 700 nm, are covered with a large featureless background.

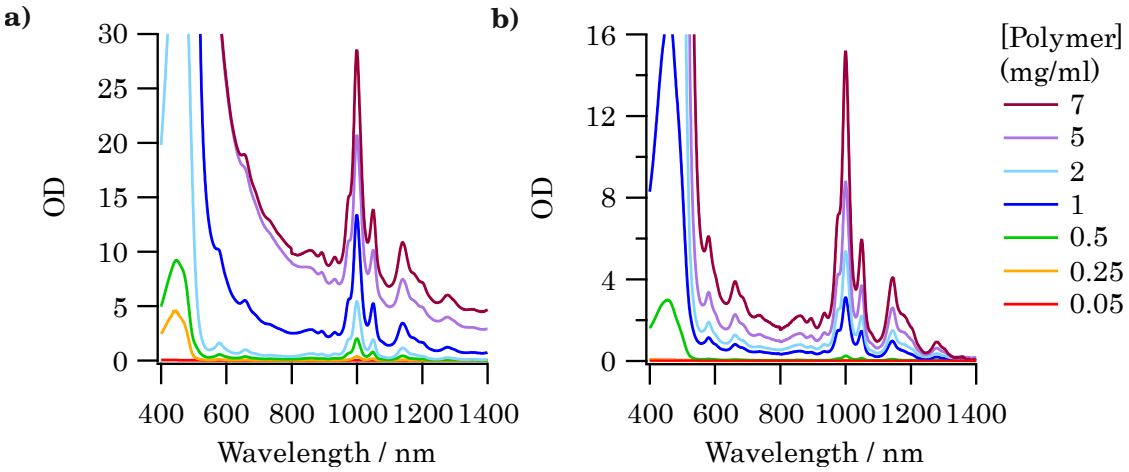

Figure 4.7: Optical absorption spectra of the SWNTs wrapped with a) PFOT2 and b) PCzT2 with a concentration range of each polymer from 0.05 to 7 mg ml^{-1}. Dispersions were prepared in toluene and corrections due to solvent absorption are made.

PCzT2 spectra show four semiconducting SWNTs. S_{11} Transitions for (7,3), (8,3), (6,5) and (7,5) SWNTs are seen at 940, 978, 1005 and 1052 nm, respectively. At around 583 and 662 nm, S_{22} transitions for (6,5) and (7,5) tubes can be recognized. For the rest of the dispersed chiralities, S_{22} transitions vanish under the background.

Here, it should be noted that as measured absorption spectra of PFOT2 and PCzT2 are subjected to an elevation due to the polymer absorption peak which appears at 447 nm for PFOT2 and 456 nm for PCzT2.

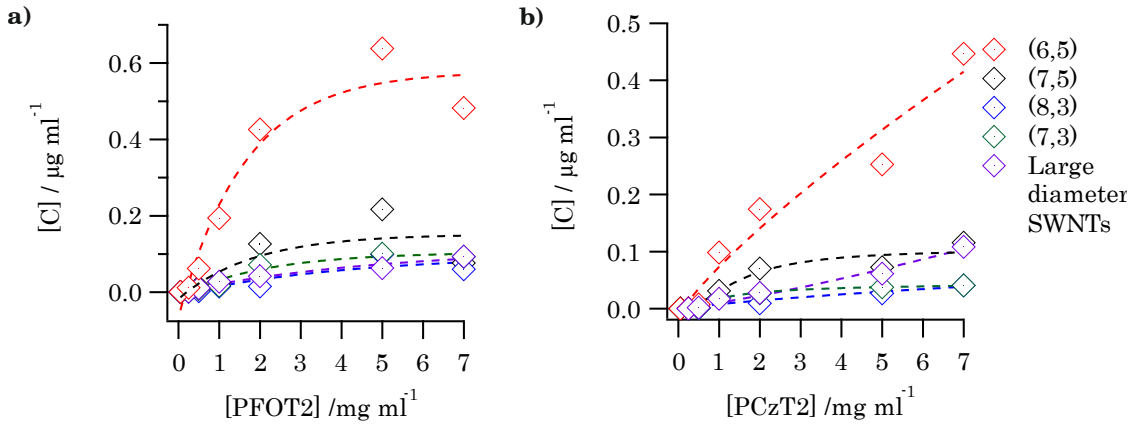

Figure 4.8: Carbon concentration per dispersed chirality for a) PFOT2 and b) PCzT2 wrapped SWNTs with increasing wrapping polymer concentration.

The tendency of dispersing SWNTs for these fluorine and carbazole containing polymers differs as it can be seen from Figure 4.8. For both polymers, the most abundant chirality is (6,5) although the selectivity for this chirality is not as high as it was with PFOBPy. PFOT2 wrapped SWNTs show saturation in the carbon concentration starting with 2 mg.ml^{-1} for (6,5), (7,5), (7,3) and (8,3). For PCzT2 on the other hand, saturation for the abundant chirality is yet to be reached within the concentration range. Considering an almost linear increase of carbon concentration for PCzT2 wrapped (6,5) tubes, selectivity closer to PFOBPy can be obtained for polymer concentrations higher than 7 mg ml^{-1} with a corresponding polymer to nanotube weight ratio higher than 14:1.

b. Photoluminescence Excitation Spectroscopy of PFOT2 and PCzT2 wrapped SWNTs

Figure 4.9 represents dispersions with PFOT2 (a) and PCzBPy (b) in toluene for 5 mg ml^{-1} polymer concentration, holding features representing the whole set of dispersions of these thiophene-containing polymers.

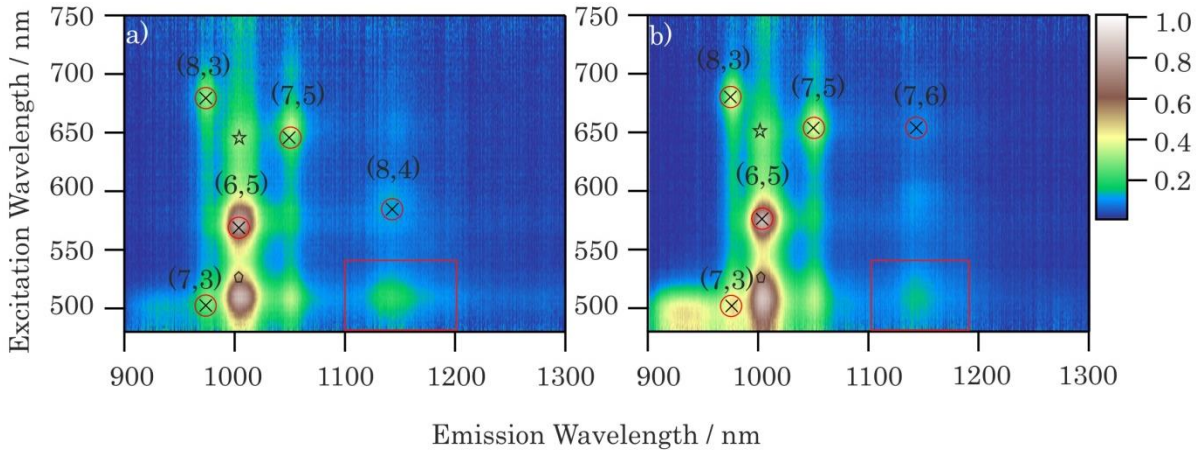

Figure 4.9: SWNTs wrapped with a) PFOT2 and b) PCzT2 for 5 mg ml^{-1} polymer. Dispersions were measured in square cuvettes with 2 mm path length and emission is measured perpendicular to the excitation. Spectra are normalized to the excitation beam intensity at each excitation wavelength and corrected for the relative collection efficiency and photodetector responsivity at the emission wavelength. Maximum photoluminescence intensity for each PLE map is normalized to 1. Dispersed chiralities are assigned according to Reference 35.

PLE maps of PFOT2 wrapped SWNT dispersions have peaks corresponding to (6,5), (7,5), (7,3), (8,3) and (8,4) tubes. A wide emission peak corresponding to the polymer, excited at 447 nm, appears at around 930 nm.

PCzT2 PLE maps contain emission peaks for (6,5), (7,5), (7,3), (8,3) and (7,6) semiconducting SWNTs. Around 900 nm, wide emission peak for the polymer is observed with an excitation at 456 nm.

Photoluminescence features that appear complementary to the photoemission of SWNTs, excited at lower (E_{12-21}) and higher (E_{22-G}) wavelengths, are observable for both samples. Transverse photoexcitation (E_{12-21}), at around 640 nm for (6,5) SWNTs and phonon-assisted excitation at around 530 nm (E_{22-G}) are marked with a star and a pentagon in Figure 4.9 respectively.

Surprisingly, for both of dispersions, emissions from all species are seen when excitation is around 447 nm for PFOT2 and 456 nm for PCzT2, which are in coincidence with maximum absorption wavelengths of the polymers. These emissions are unlikely resulted from E_{33} resonance excitation as the PLE peak positions are not matching. Especially peaks appearing around 1150 nm for both dispersions, framed with a red rectangle are showing the exceptional case for the SWNTs that are wrapped with these thiophene-containing polymers. Here, as it was suggested by Chen et. al. for PFOT2 [84], both of these polymers are functioning as light absorbers which transfer energy to SWNTs and cause NIR emissions of SWNTs subsequently. Broad emission of PFOT2 and PCzT2 extending to longer wavelengths or the weak absorption between E_{22} and E_{33} peaks might contribute to this energy transfer.

Next, for each SWNT chirality, a photoluminescence spectrum is extracted from the cross sections of measured PLE maps at the corresponding excitation wavelength. Areas under the curves are calculated by fitting Voigt shaped peaks on the measured spectrum in order to find the photoluminescence intensities and peak widths.

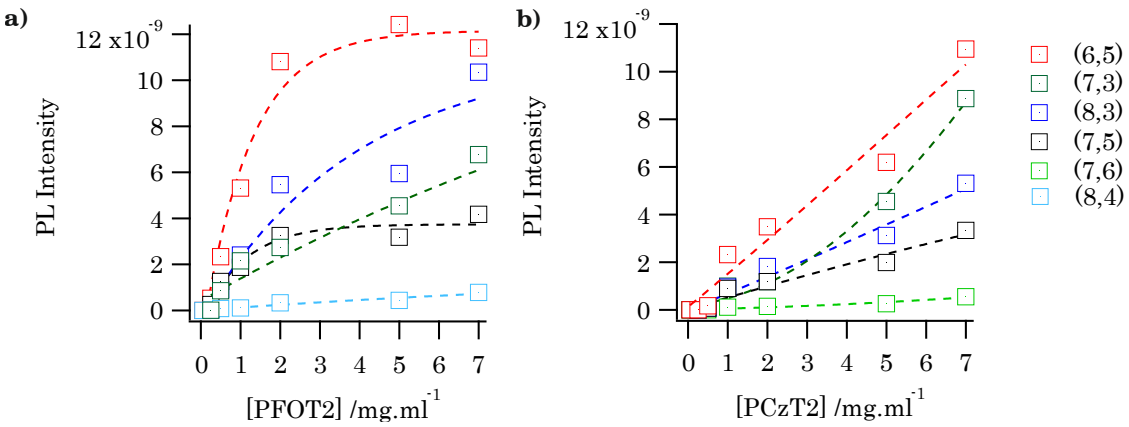

Figure 4.10: PL Intensity for each chirality plotted as a function of polymer concentration for a) PFOT2 and b) PCzT2. Data (squares) are fitted exponentially which is represented by dashed lines for each chirality.

Integrated photoluminescence intensities with increasing polymer concentrations can be seen in Figure 4.10. For PFOT2, present SWNTs tend to have increasing photoluminescence until the polymer concentration reaches around 2 mg ml^{-1}. Afterwards, saturation in photoluminescence is seen almost at the same point for all chiralities. For polymer concentrations higher than 2 $mgml^{-1}$ the constant photoluminescence intensity of dispersed semiconducting SWNTs can be attributed to an enhancement in PL quenching [20].

Photoluminescence intensity for PCzT2 dispersed SWNTs, on the other hand, increases linearly with increasing polymer concentration. This trend, which resembles the increase of dispersed nanotube concentration, indicates that photoluminescence quenching is not as dominant as in the SWNTs dispersed with PFOT2. This might be attributed to any metallic tube content or the more effective charge transfer from the carbazole containing polymer to the SWNTs than its fluorene containing homolog.

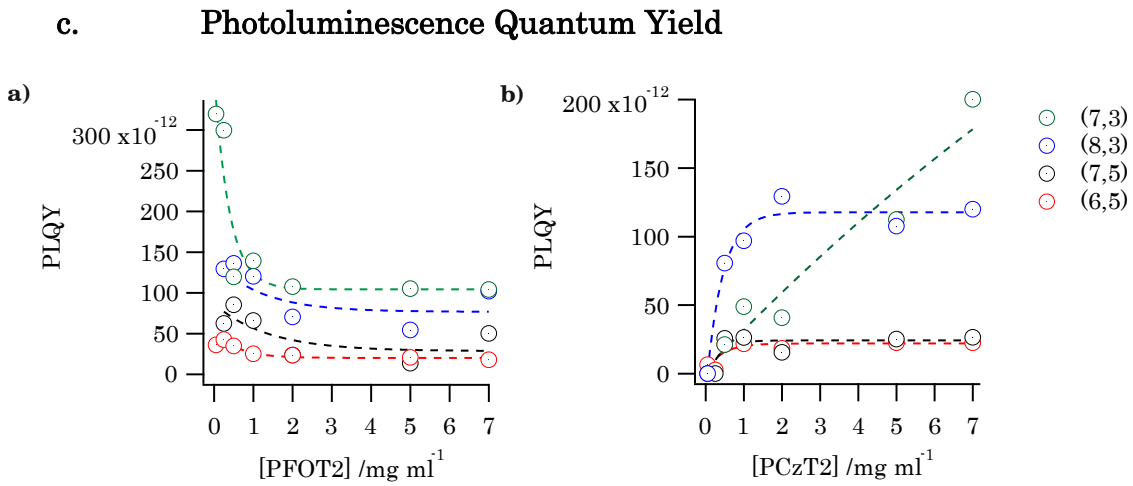

Figure 4.11: Relative photoluminescence quantum yields with increasing polymer concentration for a) PFOT2 and b) PCzT2. Circles represent calculated rPLQY for each concentration using Equation 4.7 and an exponential fit for each chirality shows the evaluation of the rPLQY.

PLQY values for PFOT2 dispersed SWNTs are decreasing linearly until around 2 mgml^{-1} polymer, where the quantum yield reaches a constant value. For PCzT2 on the other hand, an increase followed by a saturation in the PLQY is seen for every chirality except (7,3).

Surprisingly, photoluminescence quantum yield of each polymer set decreases almost linearly with increasing tube diameter. The decrease of PL quantum yields is most likely associated with the photoluminescence energy transfer, suggesting that inter–tube energy transfer, from large to small diameter tubes, may also be present [103]. These findings have far-reaching consequences for the choice of the polymer as a dispersion material for applications where understanding the flow of energy and charge in coupled nanotube materials is important.

4.2.3 Biphenyl Copolymers of Fluorene and Carbazole

a. Optical Absorption Spectroscopy of PFOBPh and PCzBPh wrapped SWNTs

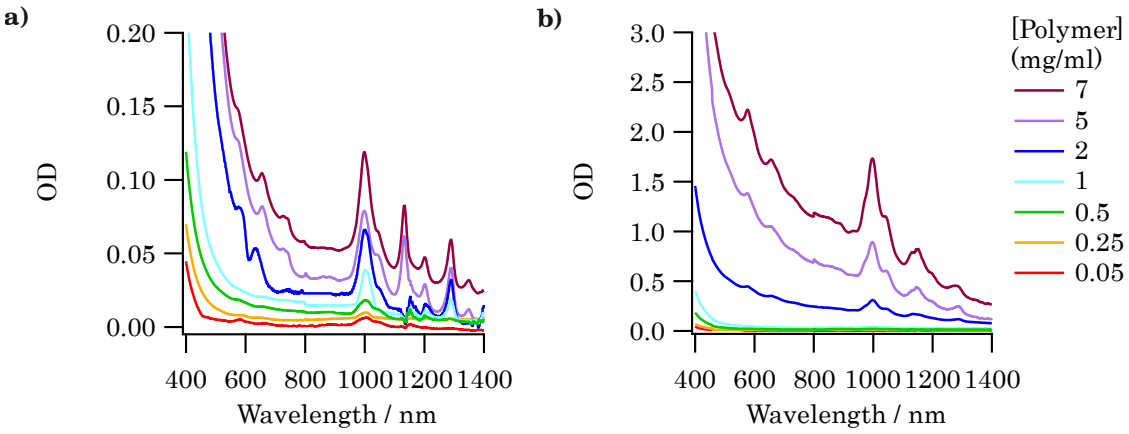

Figure 4.12: Optical absorption spectra of the SWNTs dispersed with a)PFOBPh and b)PCzBPh with a concentration range for each polymer between 0.05 to 7 mgml^{-1}. Dispersions were prepared in toluene and corrections due to solvent absorption are made.

In PFOBPh wrapped SWNT dispersions, 2 different chiralities are distinctly observed for all polymer concentrations: (6,5) and (7,5) SWNTs. S_{11} and S_{22} transitions of (6,5) SWNTs are at 1000 and 575 nm and of (7,5) SWNTs are at 1050 and 656 nm. For the concentrations higher than 5 mgml^{-1}, S_{11} transitions of (7,6), (8,6) and (8,7) semiconducting SWNTs are appearing at 1132, 1202 and 1291 nm with corresponding S_{22} transitions at 668, 727 and 743 nm.

Chiralities that are present in the dispersions of PCzBPh were (8,3), (6,5) and (7,5) with S_{11} transitions appearing at 971, 998 and 1042 nm. S_{22} transitions of these SWNTs are at 686, 577 and 658 nm. For both PFOBPh and PCzBPh, the large diameter tubes appearing between 1100 and 1400 nm are represented as a sum, similar to the other polymers, due to the congestion in the spectra for low polymer concentration dispersions.

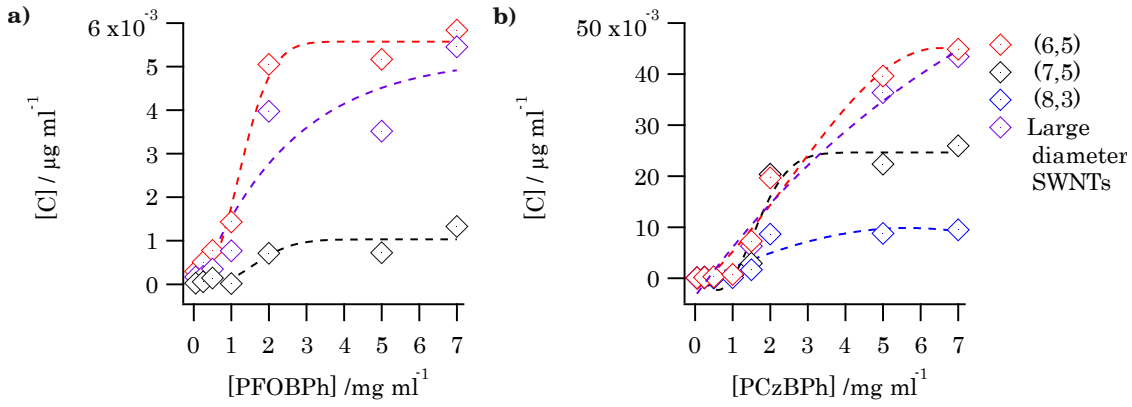

Figure 4.13: Carbon concentration per dispersed chirality for a) PFOBPh and b) PCzBPh wrapped SWNTs with increasing wrapping polymer concentration.

With both polymers, dispersed carbon concentrations per chirality tend to increase linearly until around 2 mgml^{-1} polymer and reach a plateau. Only large diameter SWNTs continue on increasing with increasing polymer concentration. The abundance of larger diameter SWNTs is surprising, considering their minority in the starting material. This might be showing the tendency of both biphenyl containing polymers to disperse large diameter SWNTs.

b. Photoluminescence Excitation Spectroscopy of PFOBPh and PCzBPh wrapped SWNTs

PFOBPh wrapped SWNT dispersions have photoluminescence peaks corresponding to (6,5), (7,5), (7,6), (8,6) and (8,7) tubes. Photoluminescence from (7,6) tubes appears to be the most intense although it happens to be less abundant than (6,5) SWNTs. Complementary to the photoemission of SWNTs, photoluminescence features that appear at lower (E_{12-21}) and higher (E_{22-G}) wavelengths are observed. Transverse photoexcitation (E_{12-21}), at around 730 nm for (7,6) SWNTs and phonon-assisted excitation

at around 580 nm ($E_{22-G)}$ are marked with a star and a pentagon in Figure 4.14 respectively.

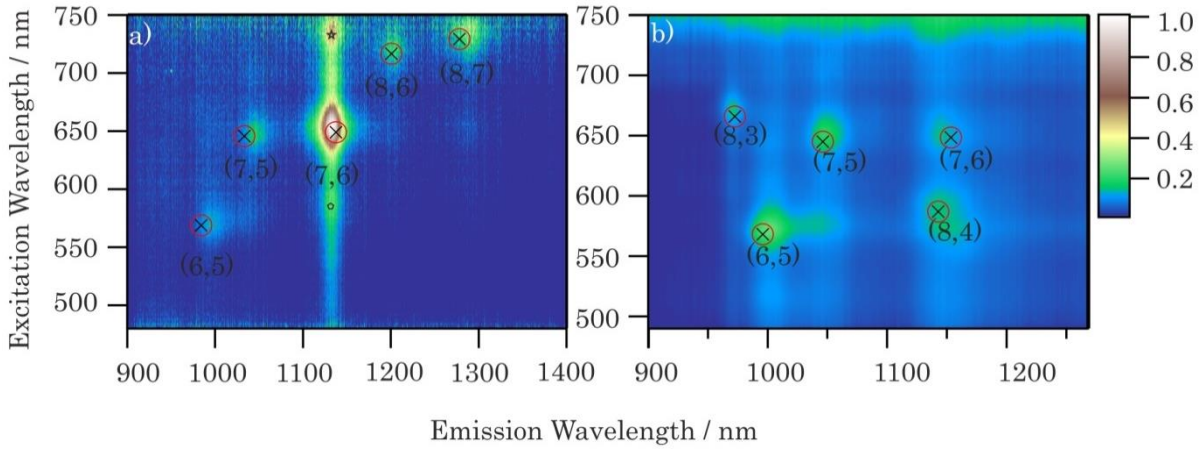

Figure 4.14: SWNTs wrapped with a) PFOBPh and b) PCzBPh for the 7 mg ml^{-1} polymer. Dispersions were measured in square cuvettes with 2 mm path length and emission is measured perpendicular to the excitation. Spectra are normalized to the excitation beam intensity at each excitation wavelength and corrected for the relative collection efficiency and photodetector responsivity at the emission wavelength. Maximum photoluminescence intensity for each PLE map is normalized to 1. Dispersed chiralities are noted according to Reference 35.

PCzBPh PLE maps contain emission peaks for (6,5), (7,5), (7,6), (8,3) and (8,4) semiconducting SWNTs. Photoluminescence intensity from the appearing species, despite the 10 times higher dispersion efficiency of PCzBPh, appears to be less than for PFOBPh.

Next, a photoluminescence spectrum is extracted from the cross sections of measured PLE maps for each SWNT chirality in order to calculate photoluminescence intensity and peak width as well as peak emission energies.

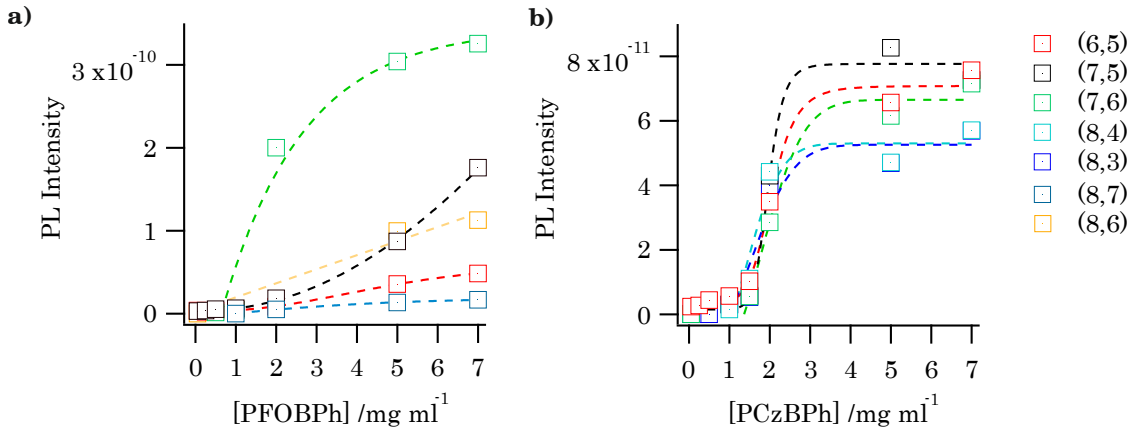

Figure 4.15: PL Intensity for each chirality plotted as a function of polymer concentration for a) PFOBPh and b) PCzBPh. Data (squares) are fitted with Hill Equation which is represented as dashed lines for each chirality.

Photoluminescence tends to increase linearly until a concentration of 2 to 3 mg ml^{-1} for all the chiralities dispersed with PCzBPh. Afterwards, PL intensity stays constant for the higher concentrations. As it is already observed with other polymers, the saturation happens around the same polymer concentration for the dispersed SWNTs.

c. Photoluminescence Quantum Yield

A high quantum yield would point out a high de–bundling efficiency. A decrease of PLQY with increasing polymer concentration is predicted to be caused by the increase in small aggregates and bundles in the denser dispersion. This, accompanied by a redshift which shows the increase in the dielectric function of the environment. Another reason for the decrease in photoluminescence quantum yield is the presence of metallic tubes and the energy transfer from semiconducting to metallic tubes ending with a non–radiative decay within the metallic species.

As seen from Figure 4.16, PLQY of PFOBPh and PCzBPh dispersed tubes decrease almost linearly until 2 mg ml^{-1} polymer concentration, where it stays constant afterwards. This was already observed with other polymers such as PFOT2 and the behavior was attributed to an increased rate of bundling due to increased dispersion density accompanied with the appearance of metallic species.

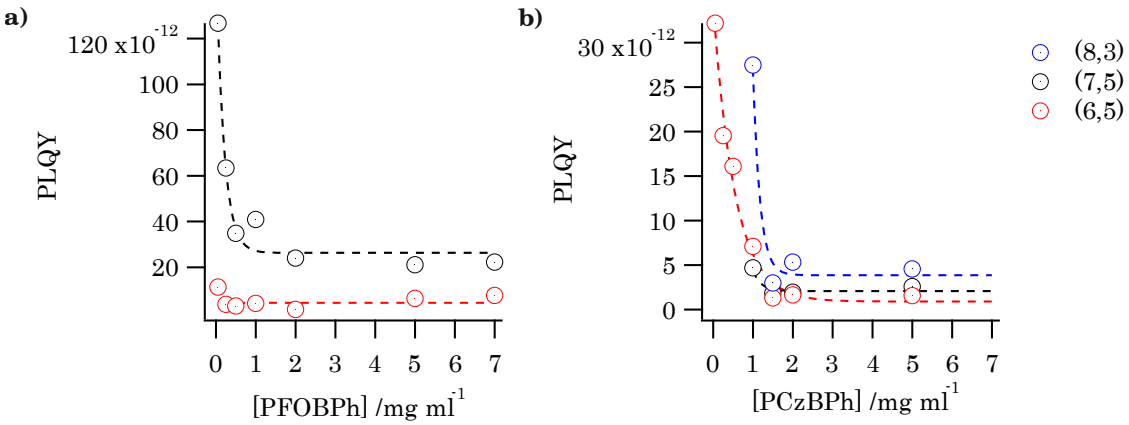

Figure 4.16: Relative photoluminescence quantum yields with respect to increasing polymer concentration. Circles represent calculated rPLQY for each concentration and an exponential fit for each chirality shows the evaluation of the rPLQY.

4.3 Difference of SWNT soot

4.3.1 CVD SWNTs synthesized at 750 and 850°C

In the previous section for investigating the influence of wrapping polymer backbone on chirality and optical properties of dispersed SWNTs, commercially available CoMoCAT SWNTs with a diameter range between 0.7 to 0.9 nm were used. With the optimized synthesis method from the commercial producer Southwest Nanotechnologies, (6,5) SWNT content of the used raw material was around 40%, with over 90% carbon content.

Here, in order to investigate the effect of the composition of the starting material on the chiral selectivity of the polymer, PFOBPh was used to disperse SWNTs synthesized with alcohol–Chemical Vapor Deposition (CVD) at two different temperatures.

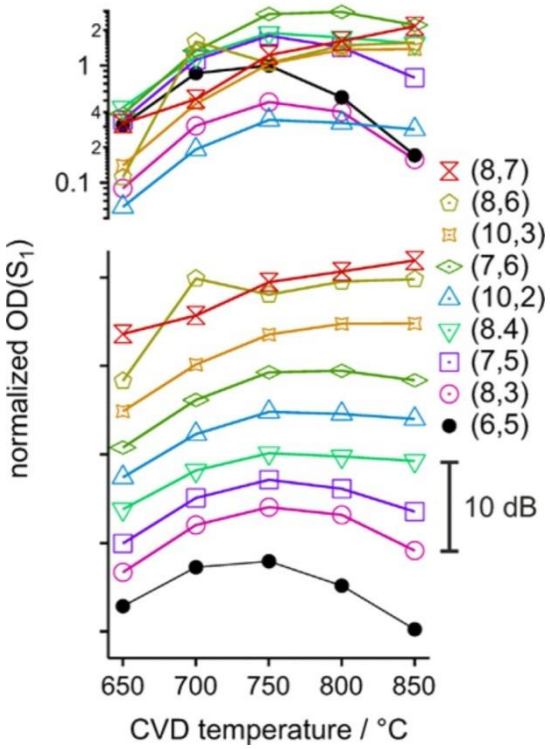

Figure 4.17: Optical Densities of the absorption features of different tube types, normalized to the optical density of the (6,5) species grown at 750 °C (above) and waterfall plot of the data (below). The figure is taken and adjusted from reference 52.

Alcohol Chemical Vapor Deposition is an SWNT synthesis method, where the composition of the synthesized chiralities depends highly on the reaction temperature. It is already demonstrated by Kastner et. al. that at higher temperatures, larger diameter SWNTs tend to be more abundant where smaller diameter SWNTs are decreasing in their yield [52]. In

Figure 4.17, the abundance of as-synthesized SWNTs at temperatures from 650 to 850 ° C is shown.

The composition of the raw material changes from small diameter SWNTs to large diameter SWNTs going to higher temperatures. At 750° C, the percentage of (7,6) tubes reaches its highest value according to the optical density data. After 750 °C, higher diameter tubes become more abundant. (8,7) SWNTs, with a steep increase, reach the optical density of (7,6) tubes at 850 °C. In the light of this data, two CVD SWNT soot synthesized at 750 and 850 °C are selected in order to investigate the effect of the raw material on the dispersed SWNT composition. CVD SWNT material was synthesized by Matthias Kastner.

PFOBPh surprisingly dispersed large diameter SWNTs in addition to the two most abundant SWNTs in the raw material (6,5) and (7,5) SWNTs, using CoMoCAT material. In two CVD raw material batches, (7,6) and (8,7) are abundant chiralities synthesized at 750 and 850 °C respectively. These species have almost the largest diameter within their batch. Between 750 to 850 °C, enriched chirality wrapped with PFOBPh is expected to change from (7,6) to (8,7) if the assumptions for large diameter selectivity are valid.

2.1.2 Absorption and PLE Spectroscopy of dispersions of PFOBPh with CVD750 and CVD850 SWNTs

In order to prepare dispersions of PFOBPh wrapped CVD SWNTs, 5 $mgml^{-1}$ polymer concentration was chosen in order to disperse 2.5 $mgml^{-1}$ CVD SWNTs. As the SWNT content of the raw material is considerably lower than CoMoCAT SWNTs, especially for low temperatures, high polymer, and SWNT raw material concentrations would enable observation of selected SWNTs easily.

Dispersions in toluene were analyzed by UV–vis–nIR spectroscopy in a wavelength range from 400 to 1400 nm. For Photoluminescence Excitation Spectroscopy, an excitation from 500 to 850 nm is monitored as emission in the range between 930 to 1400 nm. Obtained spectra are shown in Figures 4.18 and 4.19 for dispersions with CVD750 and CVD850 raw materials respectively.

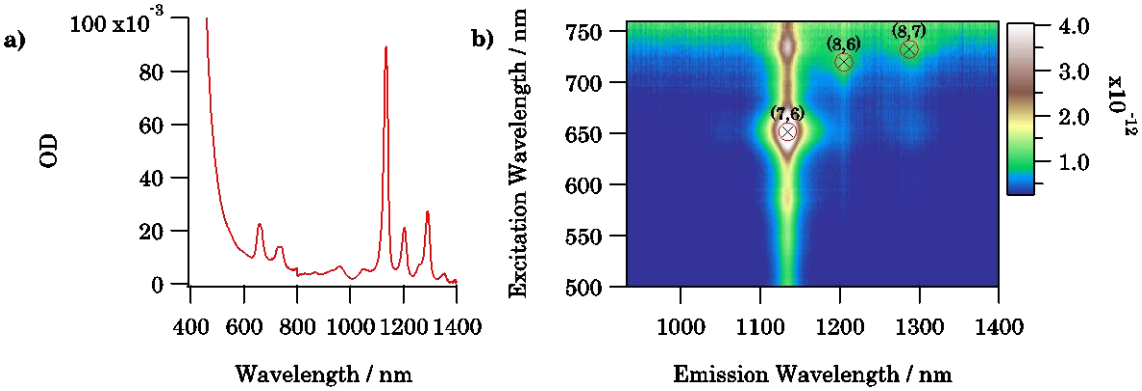

Figure 4.18: a) Optical density and b) PLE Spectra of the PFOBPh wrapped CVD750 SWNTs.

As expected, the dominant chirality dispersed with PFOBPh from CVD750 raw material is (7,6). The absence of (6,5) tubes, which were the most abundant chirality for CoMoCAT SWNTs wrapped with PFOBPh, shows that its presence was due to statistical dominance rather than the preference of the wrapping polymer.

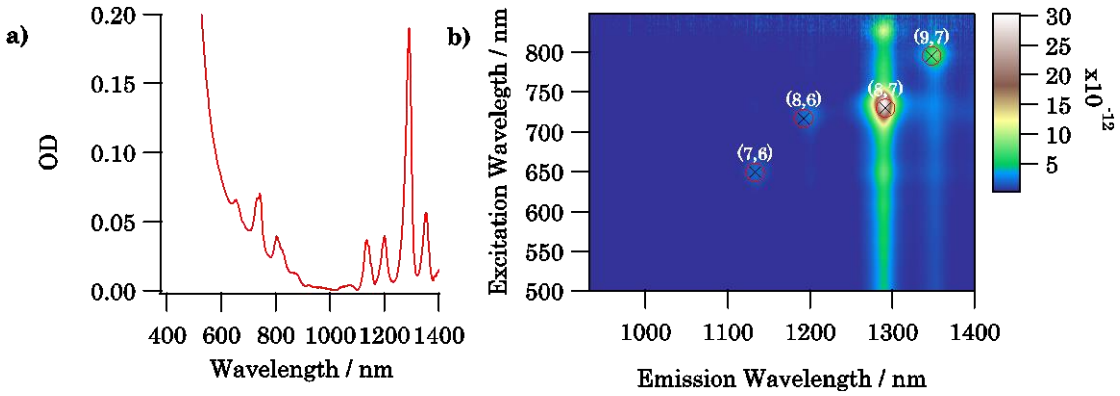

Figure 4.19: a) Optical density and b) PLE Spectra of the PFOBPh wrapped CVD850 SWNTs.

The dispersion obtained from CVD850 raw material has (8,7) as the dominant chirality. As minor SWNTs, (9,7), (8,6) and (7,6) tubes are also present in the dispersion. According to Figure 4.18, (9,7) is a minor species with less than 1 percent abundance in the raw material. Enrichment and appearance of (9,7) SWNTs together with dominance of (8,7) SWNTs emphasize the validity of the hypothesis which stated that PFOBPh tends to disperse large diameter SWNTs.

4.4 Summary of Insights into Polymer Wrapping

Here, 6 polymers with different polymer backbones were used in order to selectively disperse semiconducting SWNTs. Fluorine and carbazole were coupled with pyridine, thiophene or phenyl units. For each polymer, the concentration was increased in order to change the chiral sorting of SWNTs. Dispersed SWNTs were monitored with absorption and photoluminescence spectroscopy (Figure 4.20).

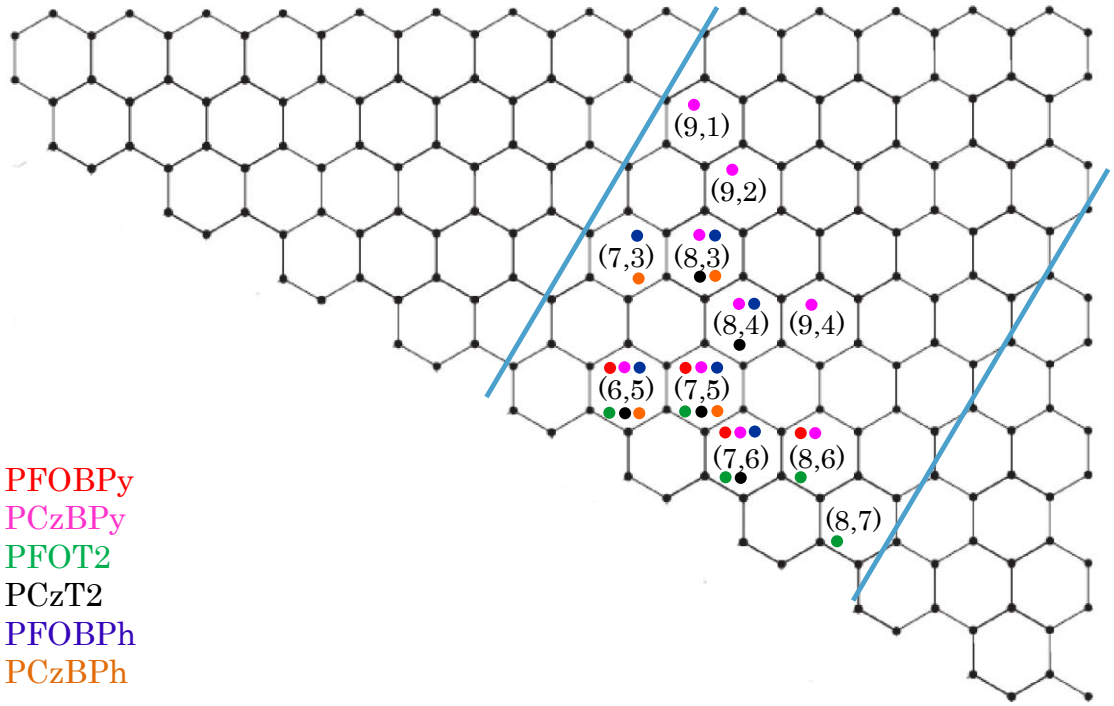

Figure 4.20: Dispersed SWNTs for polymers PFOBPy, PCzBPy, PFOT2, PCzT2, PFOBPh, and PCzBPh. Each polymer is represented with a color which is explained in the inlet of the figure. The diameter range of the CoMoCaT raw material is represented by blue lines. Metallic SWNTs are marked with blue hexagons and semiconducting SWNTs are marked with yellow.

Among all six polymers that were used as dispersing agents, (6,5) SWNTs were the most abundant chirality when CoMoCAT SWNTs were used as raw material. With PFOBPy, the highest selectivity for (6,5) tubes was observed. Dispersed carbon concentration for PFOBPy wrapped (6,5) SWNTs saturates at 1 $mgml^{-1}$. PCzBPy shows almost no chiral selectivity and its dispersions turned up to be the most polychiral dispersions among all 6 polymers.

PFOT2 disperses 5 different chiralities and at around 2 $mgml^{-1}$ saturation of the dispersed carbon concentration for all of the chiralities is seen. Unlike PFOT2, PCzT2 does not show any saturation for any of the dispersed chiralities.

With both phenyl containing polymers, dispersed carbon concentrations per chirality tend to increase linearly until around 2 $mgml^{-1}$ polymer, where, dispersed SWNT concentration reaches a plateau. The selectivity for (6,5) is higher for PFOBPh than PCzBPh. Saturation points for dispersed carbon concentration for (6,5) tubes wrapped with each polymer are summarized in Table 4.1.

Table 4.1: Summary of saturation points of dispersed carbon concentration for (6,5) tubes depending on the homopolymer (fluorene, carbazole) and copolymer (bipyridine, bithiophene, biphenyl) units.

	Bipyridine	**Bithiophene**	**Biphenyl**
Fluorene	1$mgml^{-1}$	2 $mgml^{-1}$	2 $mgml^{-1}$
Carbazole	After 7 $mgml^{-1}$	After 7 $mgml^{-1}$	3–4 $mgml^{-1}$

From the table, it can be seen that whether there are a fluorene or carbazole units in the polymer determines the saturation point of the

dispersed carbon concentration. The presence of the bipyridine, bithiophene or biphenyl unit is only of secondary importance for that matter, in order to determine the dispersion efficiency. Also, carbazole containing polymers reach saturation in the dispersed SWNTs, possibly due to the sp^2 hybridization of the N–bridging atom, different from the sp^3 hybridized C–bridging atom in fluorine unit, which reduces the steric hindrance of that position [102].

The preference of the PFOBPh to disperse large diameter SWNTs was tested by dispersing SWNT raw materials with a higher composition of large diameter SWNTs. It is found out that PFOBPh prefers to enrich the SWNT that has the largest diameter of the raw material. Obtaining a monochiral dispersion is found to be highly dependent on the used raw material in combination to the preferred polymer.

To sum up, the information obtained from PLE maps of the dispersions, there is an energy transfer seen for thiophene-containing polymers PFOT2 and PCzT2. This energy transfer was already reported in the literature for PFOT2 [84] and within this study, it is observed that same phenomenon is seen also between the carbazole containing homolog and dispersed SWNTs.

From photoluminescence and absorption data, photoluminescence quantum yields were calculated and concentrations for the start of re–bundling due to increased medium density was determined. Fluorene containing polymers are found to be superior to their carbazole containing homologs with almost an order of magnitude higher PLQY, possibly due to lower metallic SWNT content in their dispersions. Maximum PLQY is reached before 2 $mgml^{-1}$ polymer concentration in every case which points out a limit to be considered for the future dispersion studies and corresponding applications.

5. Optical and Electronic Transport Properties of 8 to 755 nm thick (6,5) SWNT film Networks

5.1 State of the Research and Purpose of this Study

For a thin film field effect transistor of a random SWNT network, in which the channel length is much larger than the average tube length, many SWNTs are involved in transport between the source and drain. Charge carriers are transported from the source to the drain through a percolating channel, therefore, electrical properties of the transistor are highly depending on the inter–tube junctions. Metallic–semiconducting SWNT junction resistance, which is 2 orders of magnitude higher than for junctions of the same type [140], makes the post-synthesis electronic purification methods crucial for higher device efficiencies. As it is already discussed in chapter four, polymer wrapping with a fluorene containing polymer, PFOBPy, is a suitable method for obtaining a chiral enriched dispersion of (6,5) semiconducting SWNTs with a semiconducting tube abundance of almost 99.9% [14]. Measuring short–channel transistor device performance of PFOBPy wrapped (6,5) SWNTs is an effective way to validate the high semiconducting purity of enriched s–SWCNTs samples.

Their strong inter–tube interactions make it difficult to deposit SWNTs homogeneously, with moderate to high coverage and without a significant presence of bundles [24]. The abundance of the bundles and inter–tube junctions increase thin film resistance. In order to improve the performance of SWNT network thin film transistors, efforts are focusing on decreasing the resistance via the number of inter–tube junctions while obtaining high coverage and homogeneous films [24, 25, 162].

Wet transfer of a vacuum filtered SWNT film was first applied by Wu et al. [141] in order to produce thin films of surfactant dispersed SWNTs in water. In contrast to aqueous dispersions, polymer-wrapped dispersions of s-SWNTs have higher tube concentration and no significant ionic component, leaving one to deal with a broader range of conditions in order to optimize thin–film formation. Very little has been reported regarding the thin–film formation of these types of polymer-wrapped tube dispersions on different substrates. In this study, the vacuum filtration wet transfer technique [141] was modified for PFOBPy selected SWNT suspension in order to prepare transparent semiconducting (6,5) enriched SWNT thin films on glass, sapphire and SiO_2 substrates. Because of the unique film structure obtained by vacuum filtration, SWNT film thickness is expected to become an important factor that needs to be considered for, in order to monitor the field effect transistor mobilities (μ_{FET}) for linear and saturation regimes.

Photophysical properties of carbon nanotube thin films are affected by their dimensions. For most thin film applications, two dimensions of the SWNT film are already optimized: the length and the width. The thickness of the film is mostly ignored as it is supposed to be too small compared to the other two dimensions. This assumption is valid for most of the direct deposition techniques. However, for vacuum filtration transfer deposition, there is a much higher limit for the obtainable thickness. Especially for applications where there is a channel or active area in the size of micrometers, hundreds of nanometers of film thickness suddenly become important for the evaluation of the thin film properties. Film characteristics should be monitored in vertical scaling for enhanced vertical scalability without compromising the film homogeneity.

Here, (6,5) enriched PFOBPy wrapped SWNT suspension is used in order to prepare thin, transparent semiconducting films using vacuum filtration wet transfer technique. Absorption, radiative and non–radiative decay from thin films were probed by absorption and photoluminescence

spectroscopy. Room and lower temperature photoluminescence measurements of neat SWNT films were performed on glass and sapphire substrates, in order to identify processes which may affect device performance and impose limitations on the use of SWNT thin films as active layers.

With the minimization of metallic SWNT content with PFOBPy wrapping and application of vacuum filtration wet transfer for film fabrication, SWNT field effect transistors with a bottom gate top electrode architecture were prepared. Obtained field effect transistor charge carrier mobilities (μ_{FET}) for linear and saturation regimes as well as on/off current ratios were monitored in order to observe the effect of vertical scaling in thin film transistors.

5.2 Optical Properties of (6,5) SWNT Thin Films

5.2.1 Absorption and Topography of (6,5) SWNT Thin Films

Absorption spectra of the prepared thin films were taken for the range of 300 to 1400 nm (Figure 5.4). Films were fixed perpendicularly to the light path and measured using a circular measurement area with the diameter of 1 mm. Homogeneity of the SWNT thin films and reliability of each measurement was controlled by respective absorption (and photoluminescence) spectra in 5 different regions of interests on each film, which ended up with ±0.5% intensity difference in absorption and photoluminescence of S_1 transitions of (6,5) SWNTs.

Film thicknesses were measured using a DEKTAK profilometer. A scratch along the diameter of SWNT thin film was produced in order to section it vertically. The profile of the scratch was measured and averaged along the diameter.

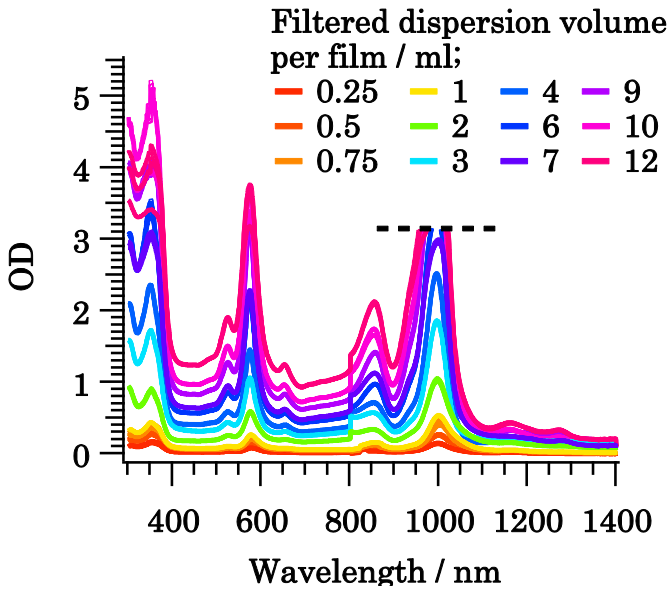

Figure 5.1: Absorption spectra for PFOBPy enriched (6,5) SWNT thin films prepared from a suspension of optical density 5. Filtrate volume is varied from 0.25 to 12 ml.

Optical densities of the films were determined by the S_{11} transition of the (6,5) tubes, seen in Figure 5.1 at 1000 nm. For the films with 7, 9, 10 and 12 ml filtrate, the optical density of the film was higher than the detection level (Figure 5.1). Accordingly, saturation in the spectra was observed. The detector change in the spectrometer is around 800 nm, therefore, corresponding optical density for these thin films was calculated from the extrapolation of the intensity of the phonon sideband that lies on the blue side (≈ 850 nm) of the S_1 transition.

Optical densities of the thin films were used in order to calculate the number of moles of carbon per film area (SWNT films have an area of 2.5×10^2 mm^2). The correlation between filtrate volume, film thickness, the optical density of the S_1 transition of (6,5) SWNTs and the amount of carbon per film area (mol C/mm^2) is exposed in Figure 5.2.

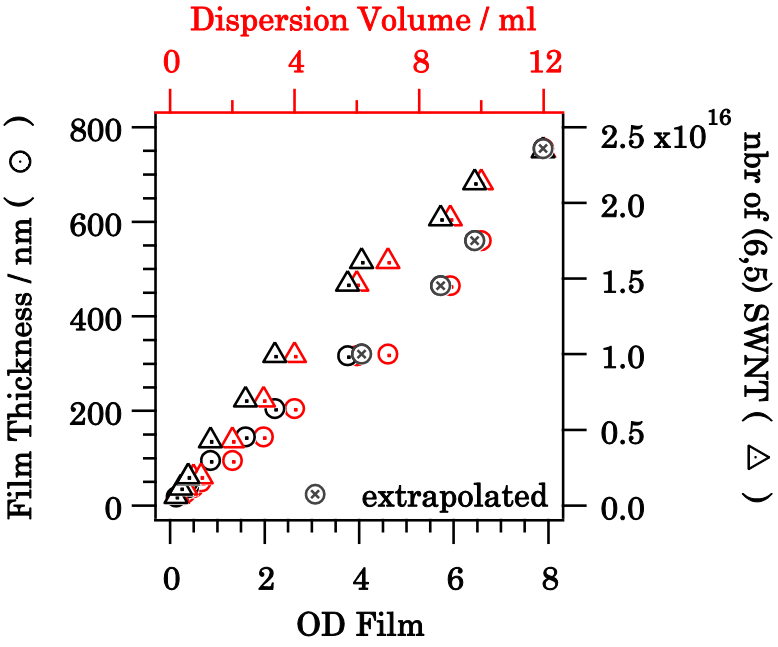

Figure 5.2: Linear correlation between the increase of filtrate volume and film thickness (red circles), increase of film thickness and optical density of the film (black circles), filtrate volume and number of SWNT (red triangles) and optical density of the film and number of SWNT (black triangles). Extrapolated optical densities for the four thickest films are marked in the figure as shown.

Increasing filtrate volume increases the film thickness linearly. An increase in the film thickness, which was obtained by profilometer measurements, causes a linear increase in the optical density of the film. The number of (6,5) SWNT is increasing linearly with increasing film optical density. All of these four factors being linearly dependent on each other is a rare condition for a thin film production method. Using spin coating, due to loss of most of the filtrate volume in film production, there is no linear dependence on filtrate volume and obtained film thickness [160]. In drop casting or doctor blading, the problem with material loss during film production is mostly solved but increasing film thickness does not mean a linear increase in film optical density as the aggregation is stronger with increasing amounts of suspension [162]. In comparison to these commonly used film production techniques, the vacuum filtration wet transfer technique provides an easy, reproducible, scalable method of producing homogeneous PFOBPy wrapped (6,5) SWNT thin films.

Evaluation of the filling volume of PFOBPy wrapped SWNTs in a vacuum filtration thin film in combination with its topography is important in order to designate the change in porosity with increasing thickness. The fraction of volume in a structure, occupied by constituent particles can be expressed by the term Volume Fraction (Φ) [167,168]. The volume fraction of SWNTs for every film can be calculated using the following formula:

$$\Phi = \frac{V_{SWNT}}{V_{FILM}}.100 \qquad (5.1)$$

where V_{SWNT} is the volume (6,5) SWNTs are occupying. It is calculated by the volume of a (6,5) SWNT with an average length of 400 nm [151] multiplied by the number of SWNTs present (Figure 5.2). V_{FILM} is the total cylindrical volume calculated using the radius (9 mm) and the thickness of each film (Figure 5.5). The resulting volume fraction with respect to increasing film thickness can be seen in Figure 5.3.

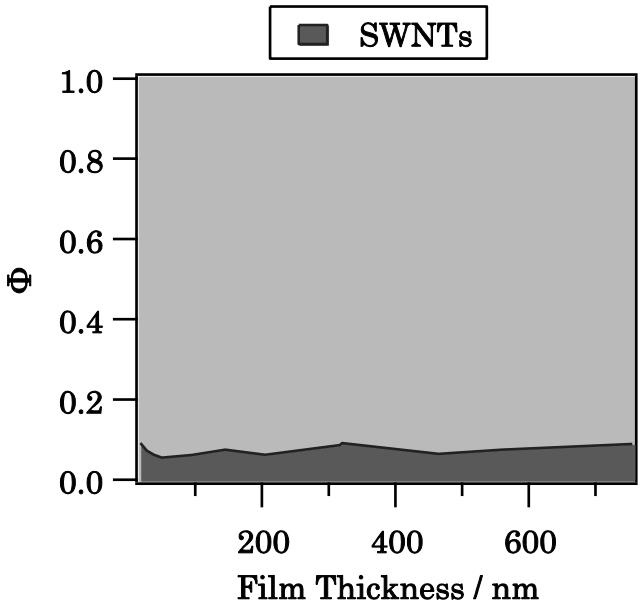

Figure 5.3: Volume fraction (Φ) of SWNTs in the volume of the thin film against increasing film thicknesses.

For the vacuum filtration wet transfer thin films with thickness from 18 ± 5 to 755 ± 5 nm, the volume fraction of SWNTs in films was found to be around 0.1. This value shows the open structure of the films, which stays almost constant over the entire range of thickness explored here.

Next, the topography of films was examined using atomic force microscopy. Squares of 2.2 µm on the film surface were scanned with a silicon tip. Tapping mode was used with a scanning speed of 1 sec/pixel. Texture and roughness of the surfaces were calculated from the obtained AFM images for every thickness using the software Gwyddion. In this software, Average Roughness (R_a) and Root Mean Square Roughness (R_{rms}) were calculated using the following equations:

$$R_a = \frac{1}{n}\sum_{i=1}^{n}|y_i| \qquad (5.2)$$

$$R_{rms}=\sqrt{\frac{1}{n}\sum_{i=1}^{n} y_i^2} \quad (5.3)$$

AFM images for the films on glass substrates are shown in Figure 5.4. Pores of the filter paper which was used as a dummy substrate to prepare the SWNT film are easily recognizable in images of vacuum filtration films in (a) and (b). As a reference, same (6,5) SWNT suspension (OD=5) was drop cast on a glass substrate. As surface roughness may increase by spin coating with successive layers of films due to the interaction of SWNTs in different layers, a monolayer coating was applied. Resulting film thickness was 10 ± 5 nm (c).

Another proof that vacuum filtration wet transfer films are highly vertically scalable is seen in the plots of surface texture and roughness in Figure 5.5. Although the patterning with the filter may have affected the surface roughness during the production of the films, due to the high pressure, average roughness (R_a) of the films are around 0.7 for both films. Constant surface roughness with increasing film thickness claims that the thickness of the film does not affect the topography of the surface.

Average roughness (R_a) of the spin-coated film was found to be 1.49 nm. In this monolayer spin-coated thin film, roughness is increased mostly by the aggregates of SWNTs on the film surface, due to the high concentration of the suspension. In comparison to spin coating, the vacuum filtration wet transfer is a more suitable method for production of vertically scalable films from high OD suspensions of SWNTs. The summary of the comparison of thinnest and thickest vacuum filtration film against spin-coated film can be seen in Table 5.1.

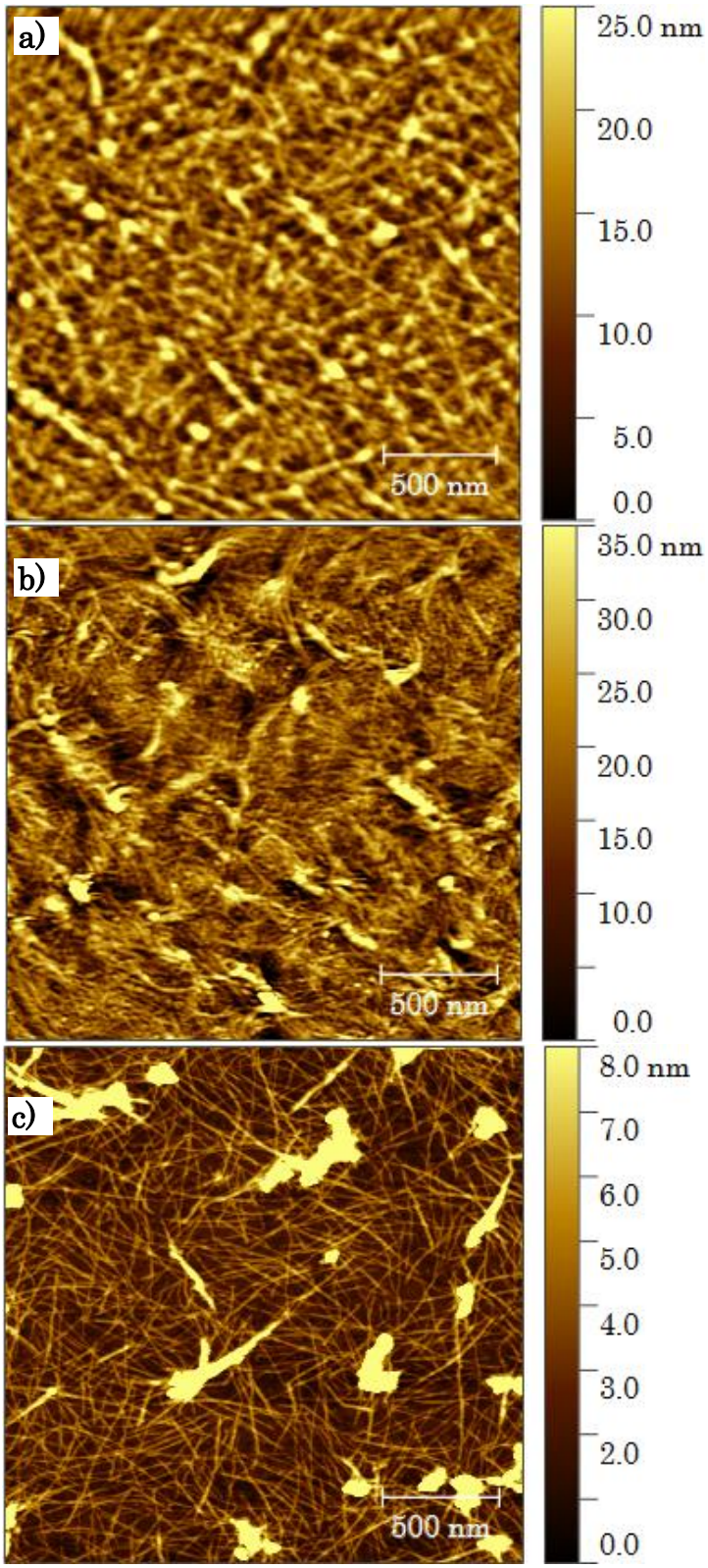

Figure 5.4: Topography of films from (a) 0.25 ml and (b)12 ml dispersion. Corresponding thickness from the thinnest film is 18 ± 5 nm and the thickest film is 755 ± 5 nm. (c) The spin-coated film with a thickness of 10 ± 5 nm.

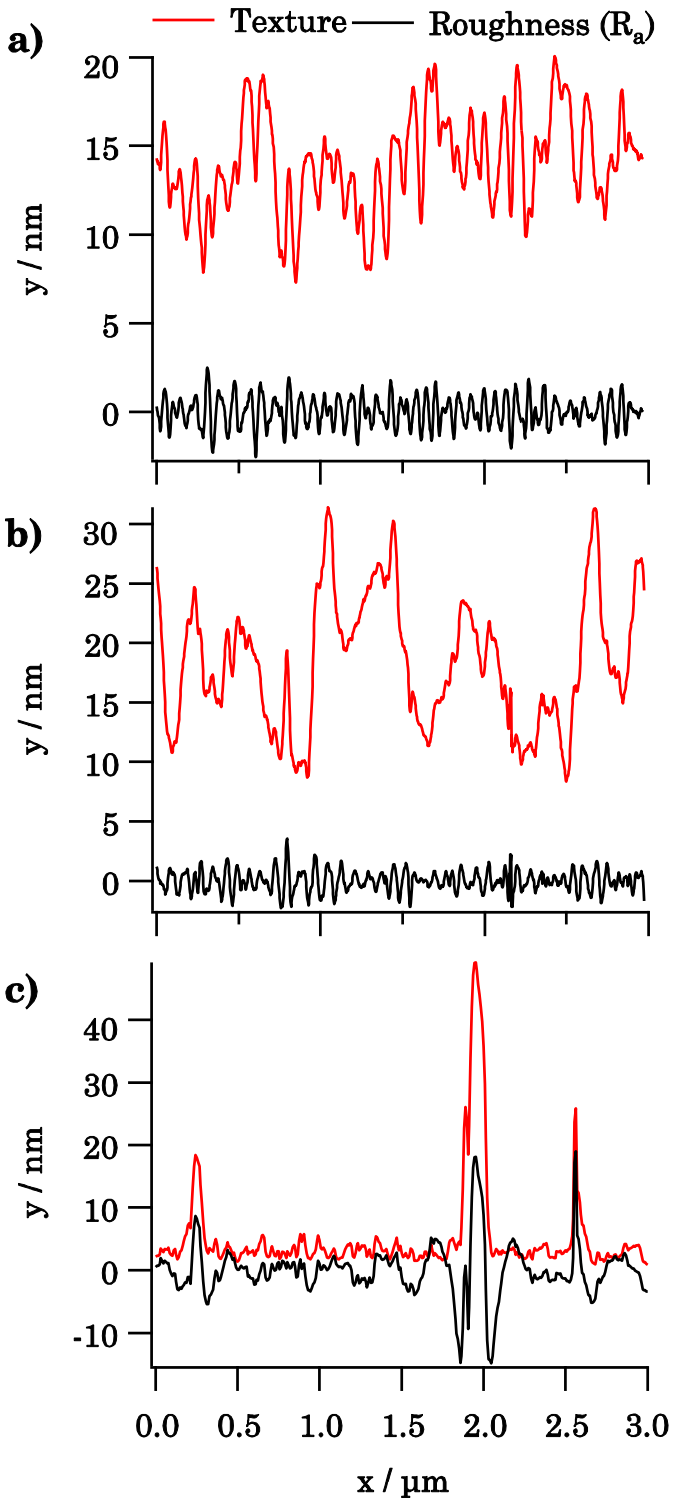

Figure 5.5: Roughness and texture of the surface of the vacuum filtration wet transfer films of (a) 18 ± 5 nm (b) 755± 5 nm thickness and (c) spin-coated film of 10 ± 5 nm thickness. X axis is along the film surface whereas y-axis lies vertically to the surface of the thin films.

Table 5.1: Comparison of Film thickness and roughness of thinnest and thickest vacuum filtration film transfer films against spin-coated films.

	Film with 0.25 ml filtrate	**Film with 12 ml filtrate**	**Spin-coated film**
Film thickness	18 ± 5 nm	755 ± 5 nm	10 ± 5 nm
R_a	0.69 nm	0.69 nm	1.49 nm
R_{rms}	0.85 nm	0.87 nm	2.29 nm

5.2.2 Photoluminescence from (6,5) SWNT Thin Films

Photoluminescence measurements were performed on SWNT films. The excitation wavelength was varied from 500 to 700 nm, measuring photoluminescence emission over the range of 928 to 1468 nm.

In Figure 5.6, PLE maps of 18 ± 5 nm, 317 ± 5 nm and 755 ± 5 nm films are shown. In addition to the expected increase in the intensity of the transition for (6,5) SWNTs which appears around 1010 nm for SWNT films on a glass substrate, the appearance of the side peaks around 1150 nm is observed.

In order to examine peak width and maxima of the S_{11} transition of (6,5) SWNTs and to monitor side peaks more accurately, line profiles from the excitation at 568 nm were extracted from PLE maps (Figure 5.7).

Increasing the film thickness increases the photoluminescence intensity of the S_{11} transition of (6,5) SWNTs. However, this increase in photoluminescence intensity is higher from 18 ± 5 to 320 ± 5 nm films thickness than the following spectra from 320 to 755 nm. There is an apparent red shift in the transition from thinner to thicker films. What's more, these already mentioned sidebands are more emphasized with

increasing film thickness. It can be seen more clearly from Figure 5.8 where the transition maxima in each spectrum are normalized to 1.

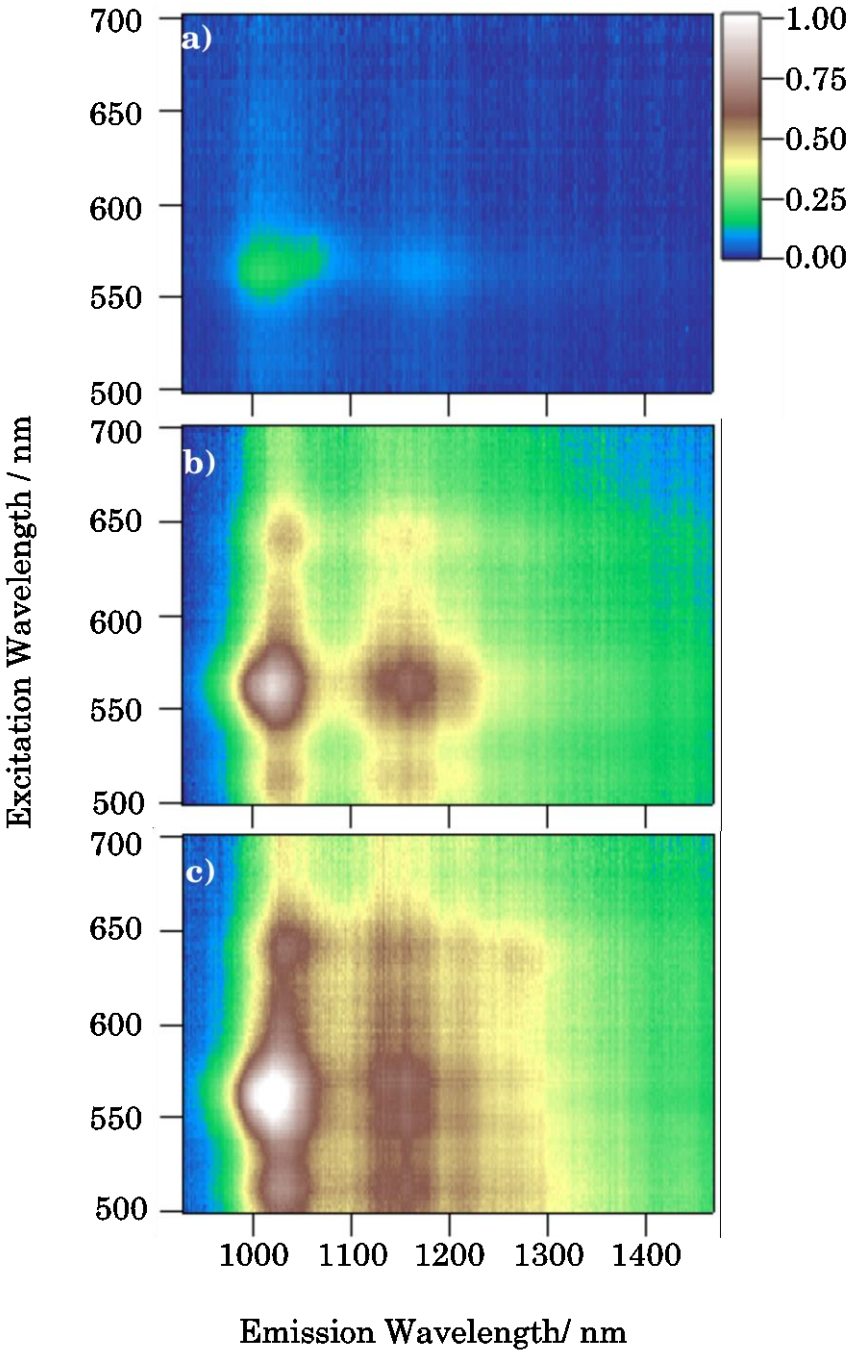

Figure 5.6: PLE Maps from the (a) 18 ± 5 nm, (b) 317 ± 5 nm and (c) 755 ± 5 nm thin films of PFOBPy wrapped (6,5) SWNTs.

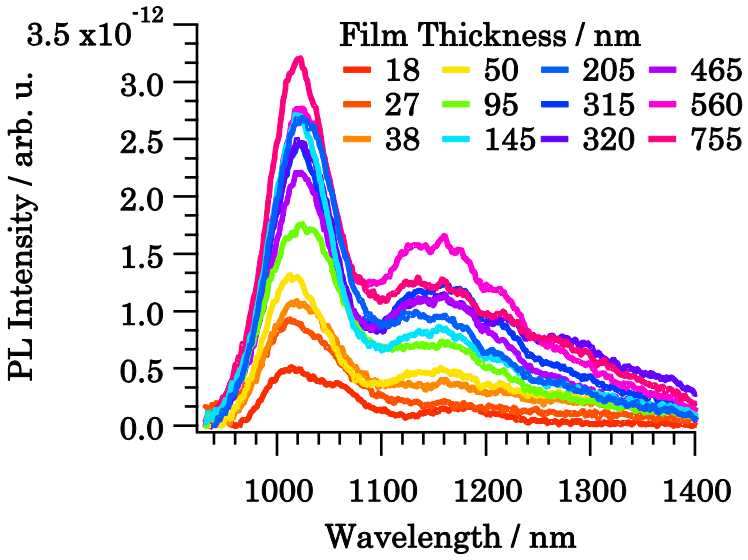

Figure 5.7: Emission line profiles of SWNT films of increasing film thickness. Films were excited at 568 nm.

There can be different reasons for the appearance of the sidebands in the photoluminescence spectra. The origin of the sideband was suggested by Murakami et. al. to be due to the coupling of K point phonons with emitted photons in order to emit in this red-shifted wavelength [163]. But in this case, the intensity of the peak is not expected to be this much affected by the increase in film thickness.

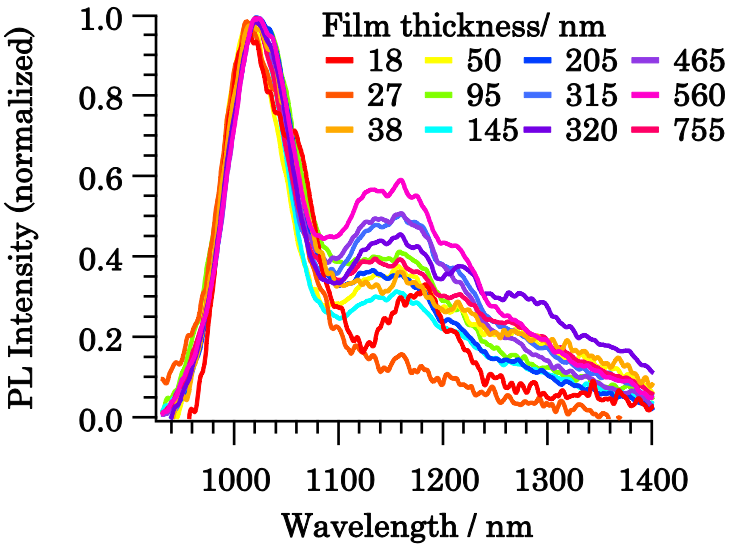

Figure 5.8: Emission line profiles normalized to the S_{11} transition of (6,5) tubes.

The second reason for the emphasized side peaks appearing at thicker films can be the reabsorption occurring more pronouncedly in thicker films. The phenomenon of reabsorption of photoluminescence arises because fluorescence excited within the body has to pass through part of the sample before detection. Where the absorption spectrum of a species overlaps its fluorescence spectrum, the fluorescence in this wavelength region may be reabsorbed. The concept of reabsorption has been the point of interest for solutions of high concentration for more than 40 years [139]. Reabsorption corrections for SWNT thin films have not been discussed often due to lack of thin film preparation methods that enable preparation of thick enough films for the reabsorption phenomena to occur.

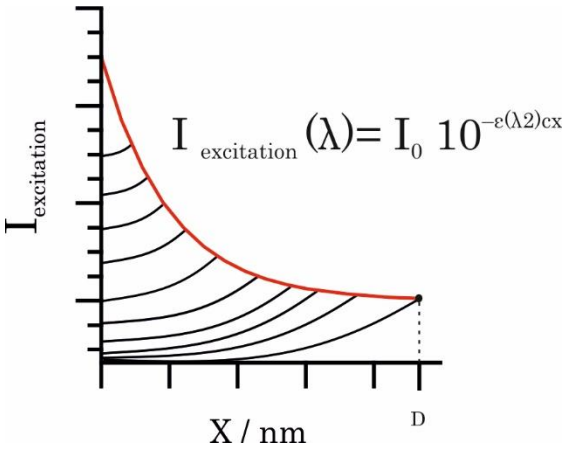

Figure 5.9: The hypothetical curve of the intensity of excitation through the film with a thickness D (red).

The intensity of excitation light is going to decrease exponentially with the depth of the material as it can be seen in Figure 5.9. If we assume total reabsorption of the photoemitted light while passing through the thickness D, the intensity of detected photoluminescence (I_{PL}) as a function of wavelength (λ) and the path the light has traveled (x) is :

$$I_{PL}(\lambda, x) = I_0 I_{PL-corr}(\lambda) 10^{-\varepsilon(\lambda_2)cx} 10^{-\varepsilon(\lambda)cx} \quad (5.4)$$

where $I_{PL-corr}$ is the reabsorption corrected photoluminescence intensity, I_0 is the incident light, ε is the molar extinction coefficient for the PFOBPy wrapped SWNTs and c is the SWNT concentration.

For the mentioned equation, if we integrate over x:

$$I_{PL}(\lambda) = I_0 I_{PL-corr}(\lambda) \int_0^D 10^{-(\varepsilon(\lambda_2)+\varepsilon(\lambda))cx}\, dx \quad (5.5)$$

And have the spatial boundaries from 0 to thickness D:

$$I_{PL-corr}(\lambda) \approx I_{PL}(\lambda) \frac{[(\varepsilon(\lambda_2)+\varepsilon(\lambda))c]}{[1-10^{-(\varepsilon(\lambda_2)+\varepsilon(\lambda))cD}]} \quad (5.6)$$

Considering that optical density is linearly dependent on the concentration and the path light passes through:

$$OD=\varepsilon cD \tag{5.7}$$

$$I_{PL-corr}(\lambda) \approx I_{PL}(\lambda)\frac{[(OD(\lambda_2)+OD(\lambda))D^{-1}]}{[1-10^{-(OD(\lambda_2)+OD(\lambda))}]} \tag{5.8}$$

Reabsorption corrected photoluminescence spectra using Equation 5.10 can be seen in Figure 5.10. Sidebands have apparently got reduced in intensity with reabsorption correction. The photoluminescence intensity of the S_1 transition has increased considerably.

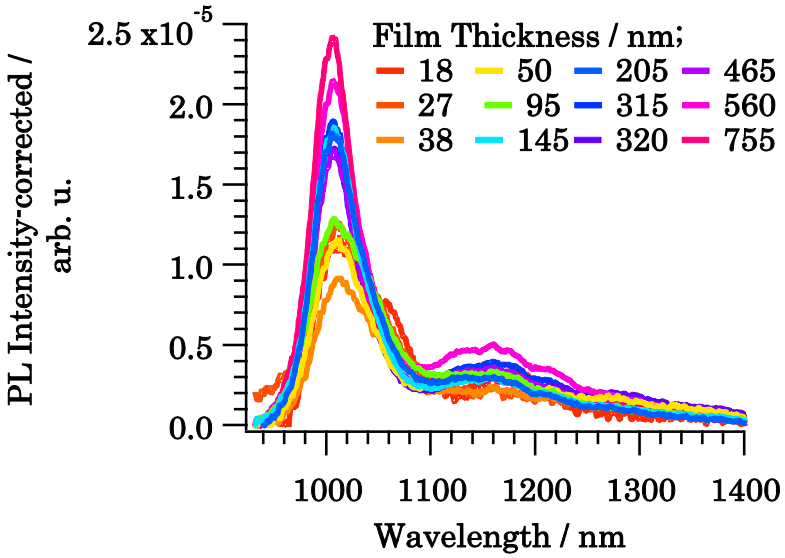

Figure 5.10: Reabsorption corrected photoluminescence spectra of SWNT thin films with thickness varying from 18 ± 5 to 755 ± 5 nm.

The change of photoluminescence peaks of the S_{11} transition is shown in Figure 5.11. Measured photoluminescence increases up to almost 200 nm of film thickness, then reabsorption comes in play and photoluminescence

reaches a plateau. For the reabsorption corrected photoluminescence, there is an increase of photoluminescence with increasing film thickness and a plateau does not appear.

Normally, saturation in the photoluminescence intensity for thicker films is highly related to a change in film density due to high aggregation or a decrease of electronic homogeneity of the SWNTs. In this case, the correction for reabsorption was enough to end up with almost linearly increasing photoluminescence intensity, suggesting that perfect upscaling was performed in terms of reproducible film quality. In order to avoid the reabsorption effects which might be problematic for applications that require higher photoluminescence efficiency, thicknesses lower than 200 nm should be chosen for the thin films.

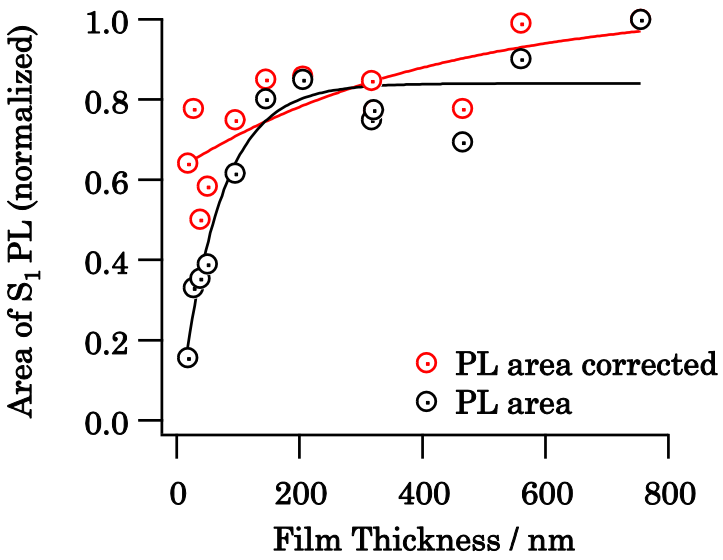

Figure 5.11: Dependence of photoluminescence intensity on film thickness for measured (black) and reabsorption corrected (red) photoluminescence spectra.

From the reabsorption corrected photoluminescence spectra, FWHM and peak maxima values are imported to Figure 5.12. With increasing film

thickness from 18 ± 5 to 100 ± 5 nm, there is a sharp decrease in peak widths with a complementing blue shift in the peak maxima. This is followed by an almost constant course for film thicknesses between 100 and 755 nm for these two criteria. This might be related to the remaining polymer content in the film after vacuum filtration. For the thinner films, where the SWNT–PFOBPy complex concentration is lower, removal of excess polymer from the pores is easier and there is no physical obstacle in the pores. With increasing filtrate volume, vacuum removal of excess polymer gets more difficult and due to a changing dielectric constant of the environment of the SWNTs, there is an abrupt change in peak widths and maxima. At around 100 nm, the ratio between SWNT and PFOBPy reaches a plateau and stays constant which stabilizes the peak maxima and FWHM values.

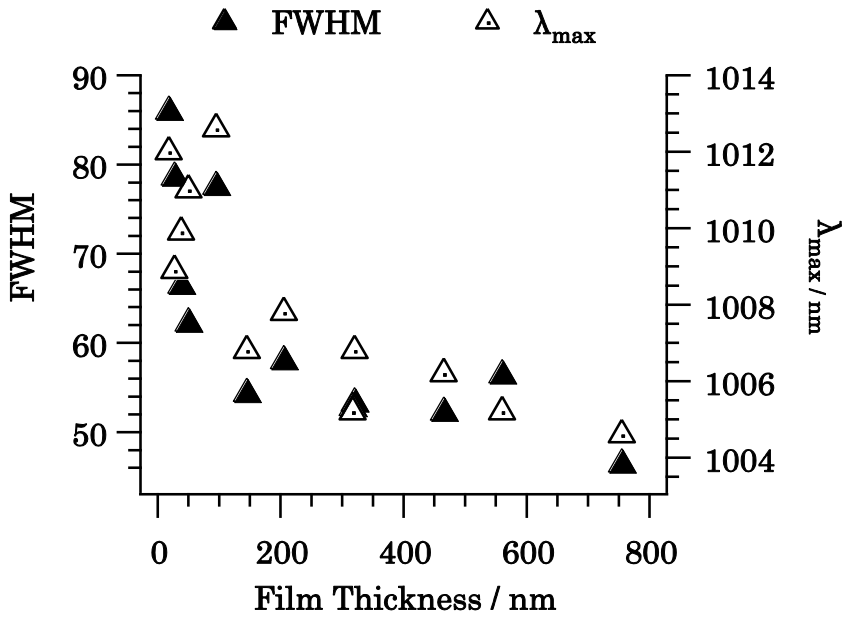

Figure 5.12: Peak width (full triangles) and maxima (empty triangles) of the reabsorption corrected photoluminescence spectra of the vacuum filtration wet transfer films with increasing film thickness.

Examining the ratio between the optical density of PFOBPy to S_1 peak of (6,5) SWNTs with increasing film thickness (Figure 5.13), it is seen that the curve has a similar trend like FWHM and maxima of the photoluminescence peaks. This supports the stated relationship between a change in the dielectric environment with a decrease in polymer content and obtained peak narrowing accompanied with a blue shift.

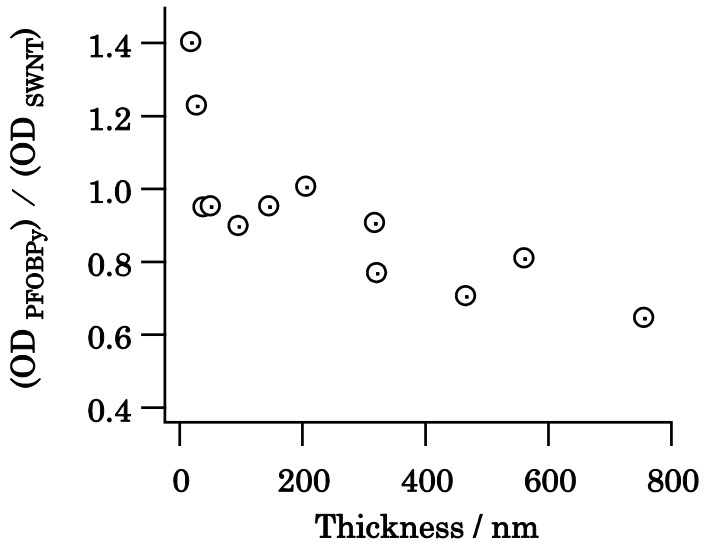

Figure 5.13: Change in the ratio of optical density of wrapping polymer (Absorption max. at 350 nm) to SWNTs (Absorption max. at 997 nm) in absorption spectra.

From the photoluminescence intensities from measured and reabsorption corrected photoluminescence spectra and optical densities from absorption spectra, photoluminescence quantum yields (PLQY) for each film from the S_1 transition were calculated. For this purpose, the already mentioned formula was applied and the resulting yield values are plotted against increasing film thickness in Figure 5.14.

Examining PLQY by studying its dependence on the thickness of monochiral SWNT films is of particular interest in this context. For thicker

films, a pronounced decrease in the PL quantum yield (QY) for emission from the first subband S_1 exciton state is observed. However, the total PLQY is much less strongly affected by interactions within the thin film network because of a considerable shift of PL intensity to lower lying states. Some of the lower energy emission resembles PL phonon–sidebands of the first subband exciton which was previously attributed to the coupling between K–point phonons and dark excitons by Murakami et. al [163].

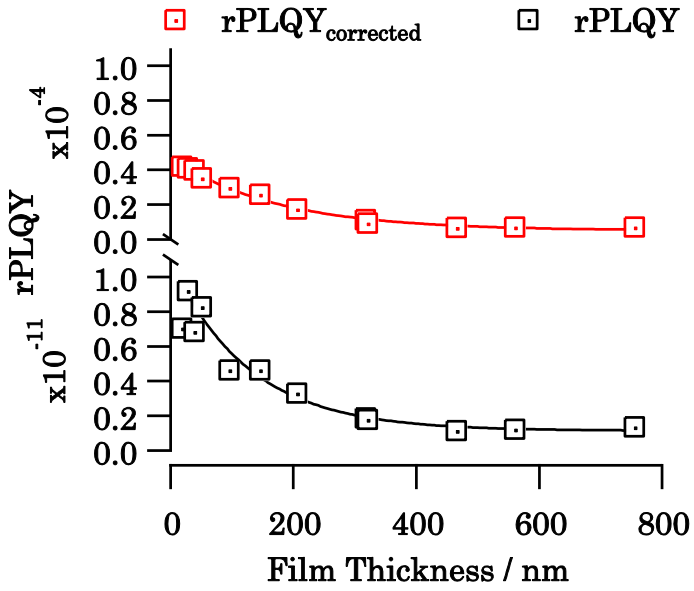

Figure 5.14: PLQY values obtained from measured and reabsorption corrected PL spectra.

a. Photoluminescence from (6,5) SWNT Thin Films at Low Temperatures

Carbon nanotube films are theoretically proven to be advantageous materials in order to be used for low-temperature optoelectronics due to the intrinsic conduction of the sp^2 lattice, unlike silicon, which needs thermal excitation for a carrier transfer from contact electrodes. For this reason, electron-phonon interactions should be carefully examined the effect of

temperature on the PL electronic band gap E_g of carbon nanotubes [2]. The difficulty in experimentally determining the behavior of optical transitions in lower temperatures lies in the surrounding of the SWNTs and therefore vacuum filtration wet transfer films of PFOBPy wrapped (6,5) films are good candidates to monitor the course of the change from radiative to non−radiative emission in increasing temperatures. It is already reported that measurements at low temperatures provide information about the exciton structure and low-lying states of SWNTs [107].

Here, a temperature range from 8.00 to 298.15 K was used in order to monitor the intensity and shift of S_{11} lines. PFOBPy wrapped (6,5) SWNT films of 18 ± 5, 317 ± 5 and 755 ± 5 nm thickness were deposited on sapphire substrates using the vacuum filtration wet transfer. Photoluminescence from the films was recorded using an excitation from 500 to 700 nm, monitoring the emission of first subband excitonic states between 900 and 1400 nm for temperatures from 8.00 to 298.15 K.

In Figure 5.15, PLE Maps of above-mentioned films at 8.00 K and 298.15 K are presented in order to show the change in peak intensity of transitions from the excitonic subband and lower lying bands. Line profiles for each temperature at the excitation maximum of the S_{11} transition of (6,5) SWNTs are plotted against emission wavelengths and shown in Figure 5.16 in order to present course of the change in photoluminescence peaks with changing temperature.

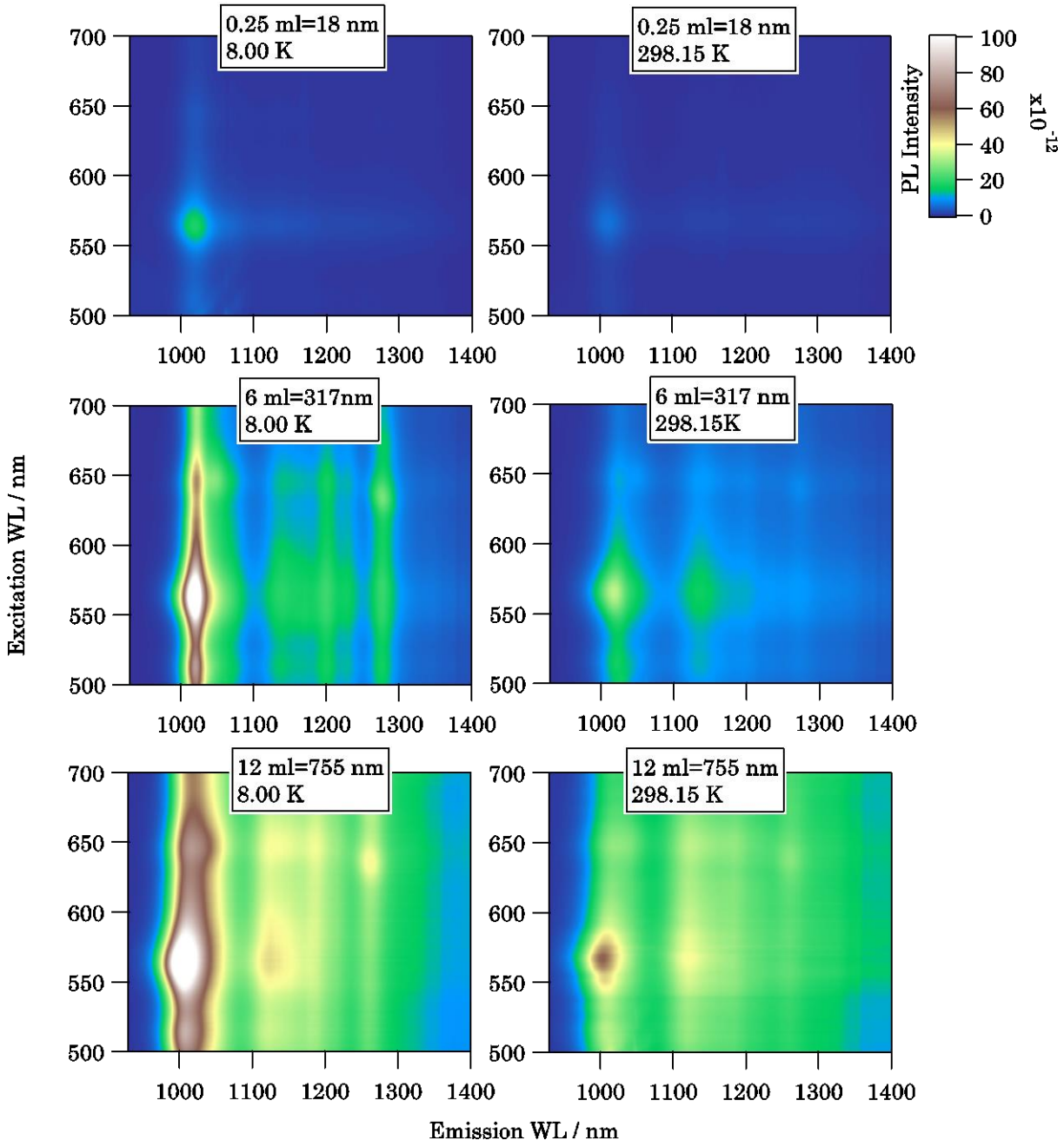

Figure 5.15: PLE Maps of (a)18 ± 5, (b)317 ± 5 and (c)755 ± 5 nm thick (6,5) SWNT films on a sapphire substrate. Photoluminescence is measured at room temperature (left) and at 8.00 K (right) for each film.

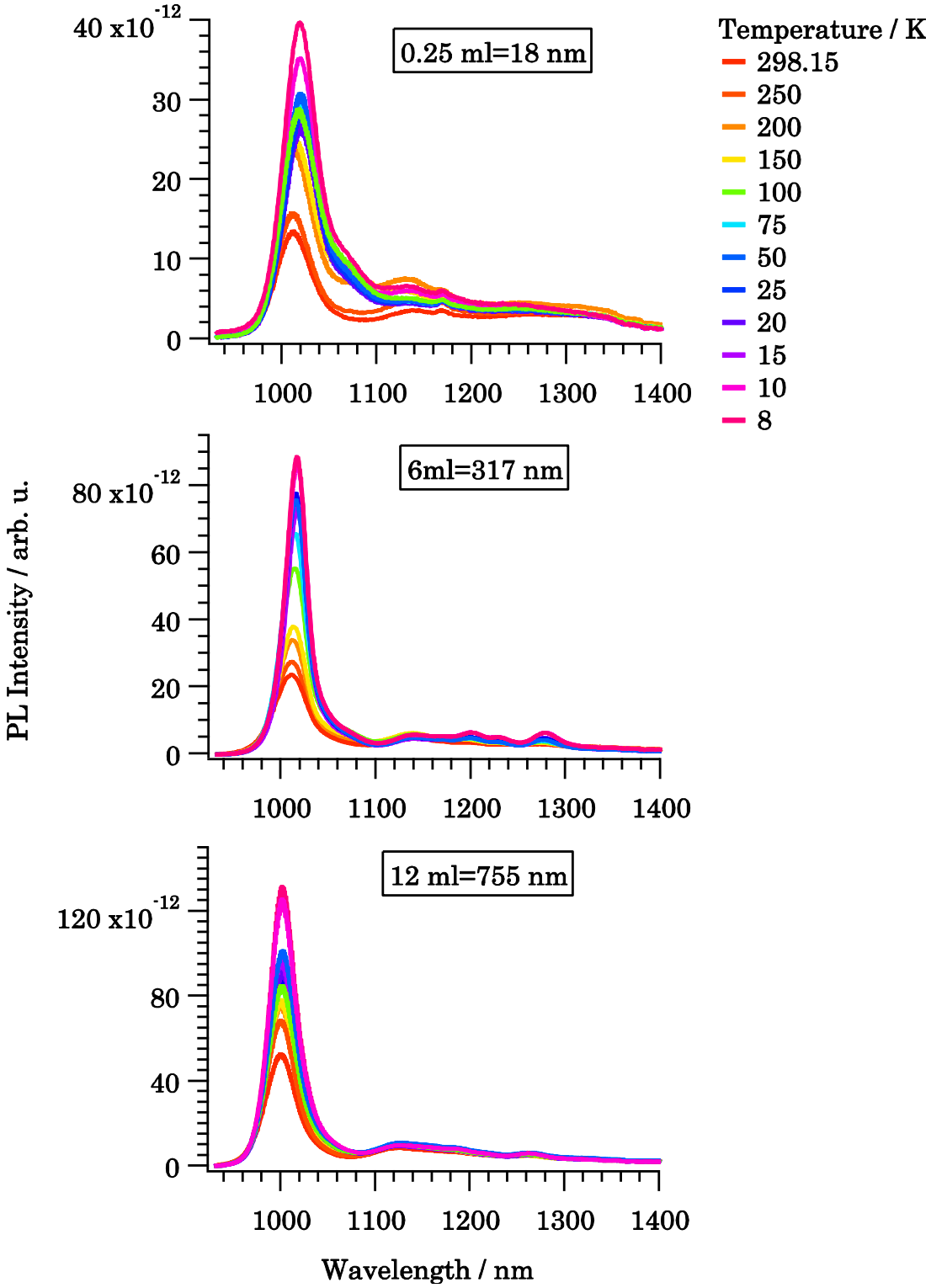

Figure 5.16: Line profiles of PLE Maps at 568 nm excitation for thin films of 18 ± 5, 317 ± 5 and 755 ± 5 nm thickness at temperatures between 8.00 and 298.15K.

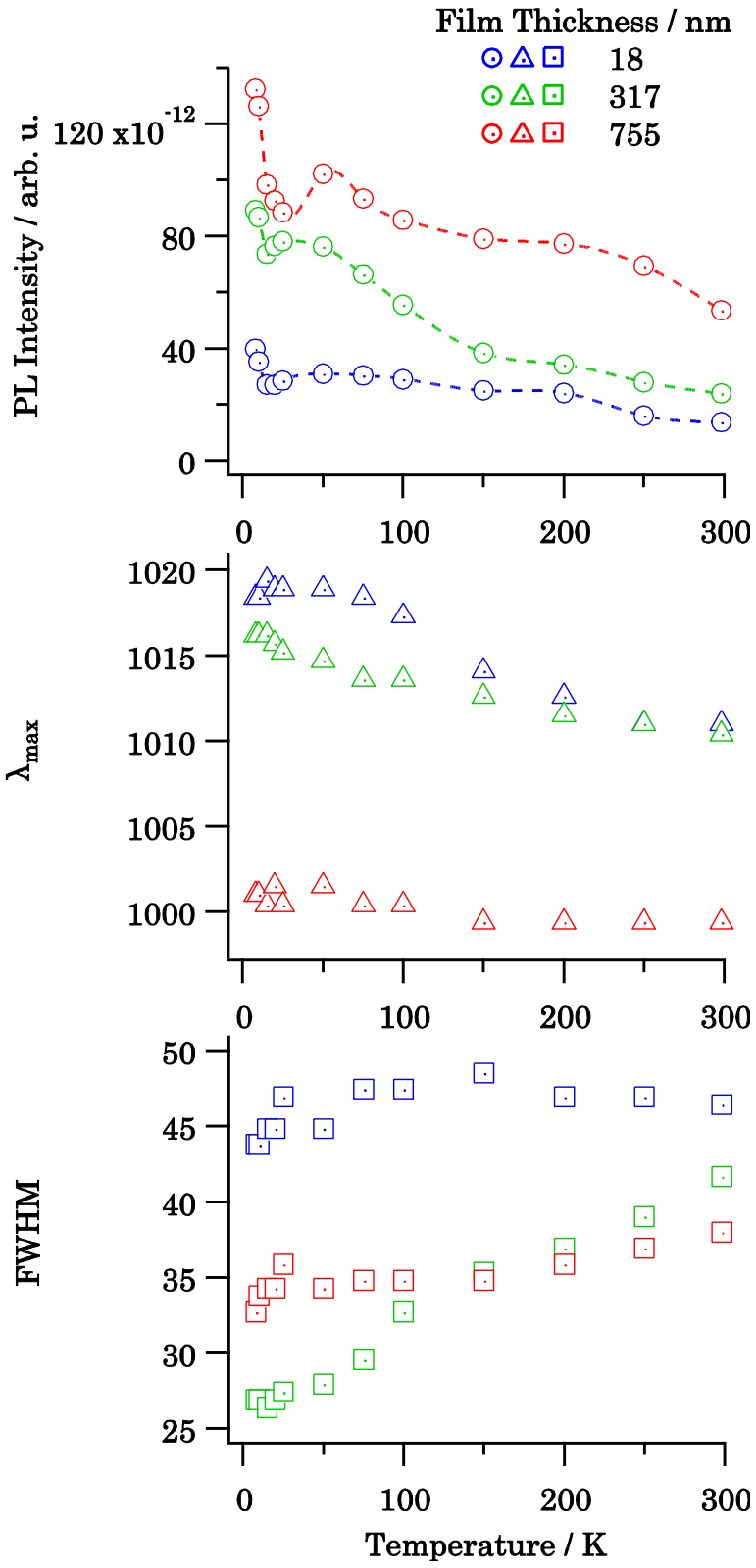

Figure 5.17: Integrated photoluminescence intensity, central wavelength and peak width of films of 18 ± 5, 317 ± 5 and 755 ± 5 nm thicknesses in a temperature range of 8.00 to 298.15 K.

The integrated PL intensity can be seen from Figure 5.17a. The trend of this curve mostly fits the explanation concerning the dependence of exciton distribution on thermal energy [116]. If excitons are fully thermalized between the bright and dark states, the PL intensity of carbon nanotubes can be expressed as:

$$I_b \alpha \frac{1}{\sqrt{T}} \times \frac{exp^{\frac{-\Delta_{bd}}{kT}}}{1+exp^{\frac{-\Delta_{bd}}{kT}}} \tag{5.9}$$

where $\sqrt{T}$ comes from the radiative recombination rate of one−dimensional excitons [122,123]. However, saturation around 50 K and the abrupt decrease immediately afterward cannot be explained only with bright excitons. For this purpose, Perebeinos et. al. and Spataru et. al. proposed a thermalization between dark and bright excitonic states and thus obtained temperature dependent decay rates [111,112]. Matching to their predictions about lower energy states being related to excitonic levels, Hagen et. al. reasoned this decrease in PL intensity with the presence of multiple peaks for spun (6,4) SWNTs with a transfer of population to the lower energy peak as the temperature decreases [117]. The dark exciton brightening was induced by symmetry breaking due to some defects or impurities [124,125]. The experimentally obtained non-zero PL intensities after the dip for PL intensity at temperatures between 50 and 8 K might be due to the slow exciton scattering between the bright and dark states as it was proposed by Matsunaga et. al. for PFO wrapped (7,6) SWNTs [126].

For the three vacuum filtration wet transfer (6,5) SWNT films, S_{11} transitions were found to have redshifts with decreasing temperature. Shift energies were found to be increasing with increasing film thickness. A spectral shift of the S_{11} lines of SWNTs with temperature change was observed by Berger et.al [108], where they used gelatin-based composite thin films of HiPCO SWNTs. For the SWNTs with q=(n−m)=1, like (6,5) SWNTs, a red shift in the S_{11} transition was seen when going from room temperature to lower temperatures. On the other hand, for q=2, same

measurements end up with a blue shift. The reason for this difference between SWNTs was related to the axial strain of SWNTs from different chiral families. Finally, the magnitude of the spectral shift was reported to be dependent on the chiral angle of SWNTs and was found to be larger for smaller chiral angles [108–110]. In this case, where all three films are made up of monochiral SWNTs with identical chiralities, differences in the magnitude of the shift can be interpreted as a consequence of high biaxial tension operating on the film and dielectric screening of the Coulomb interaction in the nanotube through its environment for higher film thicknesses [108].

Photoluminescence FWHM is reduced with decreasing temperature from room temperature to 8 K. This behavior was already reported by different groups and explained to be a result of the increased coupling between bright excitons and acoustic phonons with increasing temperature [113–115].

5.3 Electronic Properties of (6,5) SWNT Thin Films

In order to monitor the electronic properties of (6,5) SWNT thin films, 270 transistors with channel lengths (L_{CH}) of 30, 40, 50, 80 and 100 µm and channel widths (W_C) of 1000 µm were fabricated as explained in Section 3.5. They have vacuum filtration wet transfer thin films of (6,5) SWNTs with increasing film thickness (from 8 to 80 ± 5 nm) as semiconducting layers. These films with high SWNT density per channel area are promising due to the efficient electrostatic coupling between the gate and the SWNTs.

The topography of the fabricated films was examined using AFM and SEM measurements. In Figure5.18 and 5.19, AFM and SEM images of the thinnest and thickest SWNT films for field effect transistor fabrication can be seen.

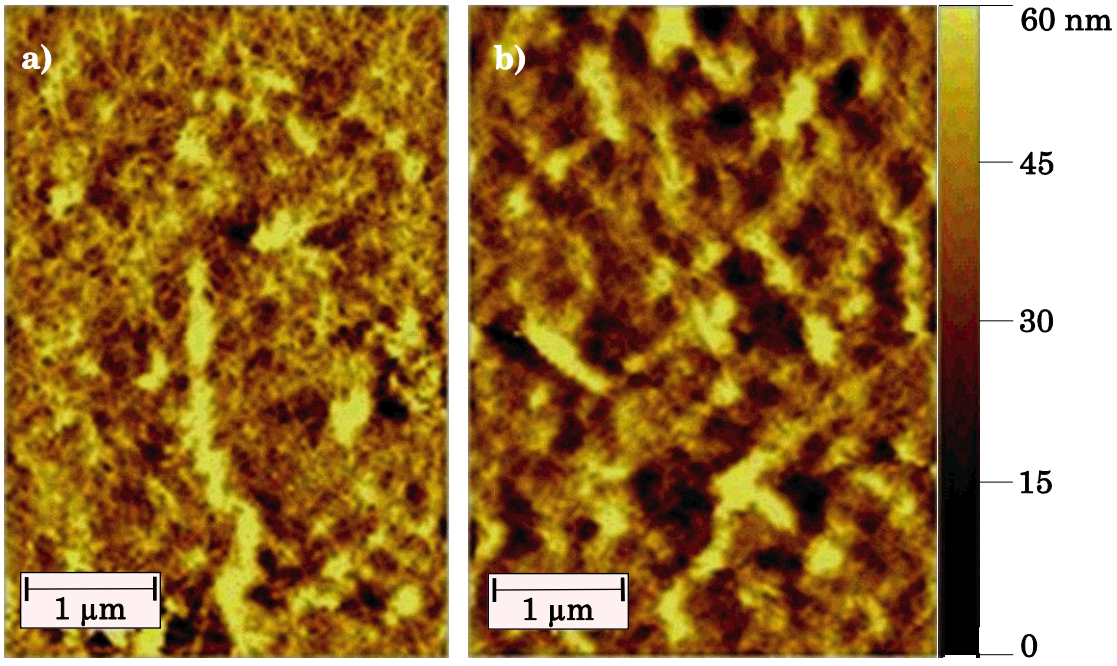

Figure 5.18: AFM images of PFOBPy wrapped (6,5) films on a SiO_2 substrate with 8 ± 5 (a,) and 80 ± 5 (b) nm thickness.

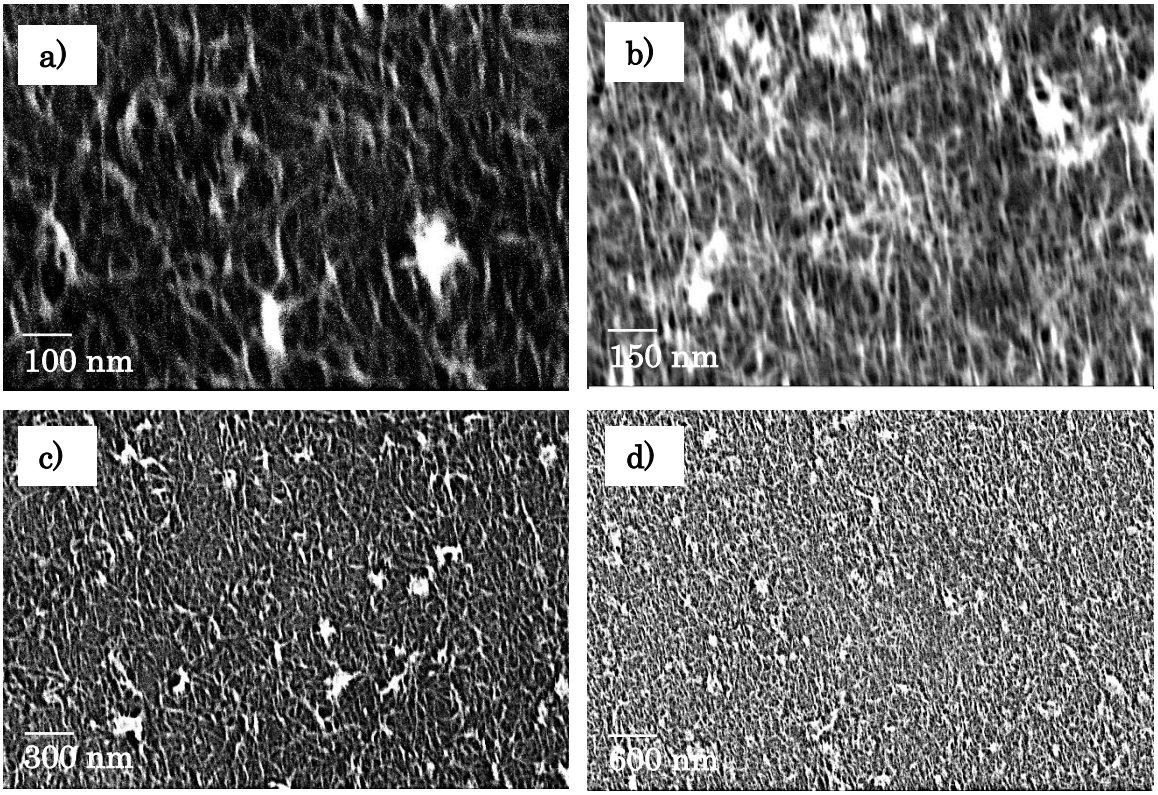

Figure 5.19: SEM images of PFOBPy wrapped (6,5) SWNT films on a SiO_2 substrate with 8 ± 5 (a,c) and 80 ± 5 (b,d) nm thickness.

5.3.1 Transfer and Output Characteristics of the SWNT Field Effect Transistors

Figure 5.20 shows representative sets of the transfer and output characteristics, measured for a solution–processed bottom gate top contact FET with L_{CH}/W_{CH} = 50/1000 µm.

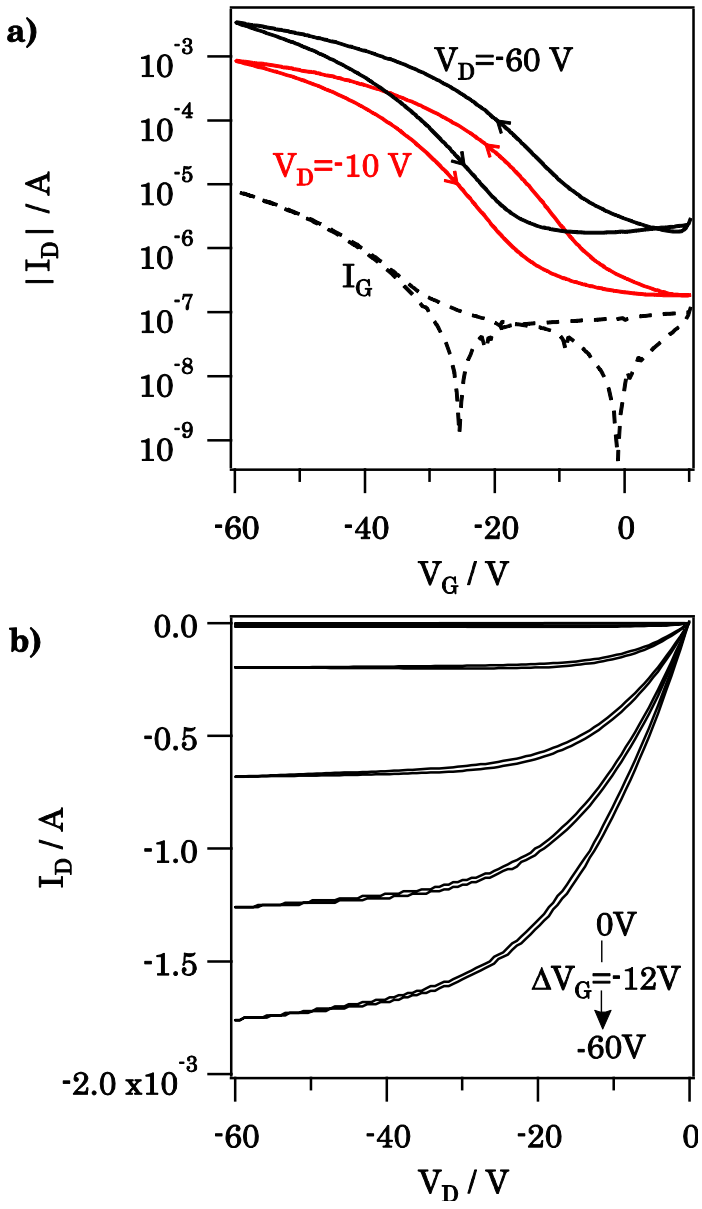

Figure 5.20: (a) Transfer characteristics of a PFOBPy sorted (6,5) SWNTs bottom–gate top contact transistor (b) corresponding transistor output characteristics.

The device exhibits a strong p–type character with an operating voltage of –60V. The main reason for this dominant p–type character may be the electron trapping nature of SWNT/SiO_2 interface. High SWNT densities obtained with vacuum filtration films have caused the increase in

operating voltage compared to spun SWNT films [138]. Use of high work function electrodes (Au ≈5 eV) and the presence of atmospheric oxidants which are known to behave as electron traps may also have contributed to the p–type character [131,132]. Use of a suitable dielectric, change of device architecture or electrode material may lead to a change in the behavior of device or improvement in the operating voltage [133–135]. Here, optimization of the device architecture is beyond the scope of this study.

Hysteresis in the operation is observed in all transistors which are attributed to the surface adsorbates and water on the surface between SiO_2 and SWNTs [136,137]. In fact, the hysteresis with vacuum filtration films was found to be less than with the spun films of PFOBPy wrapped (6,5) SWNT random network transistors [138]. This improvement is attributed to the wet transfer with toluene on SiO_2 which improves the dielectric–semiconductor interface.

The representative device exhibits appreciable channel current on/off ratio ($I_{ON}/I_{OFF}>10^4$). Linear (l_{LIN}) and saturation (l_{SAT}) hole mobilities were calculated to be 4.4 $cm^2\ V^{-1}\ s^{-1}$ and 5.9 $cm^2\ V^{-1}\ s^{-1}$ respectively. Current on/off ratio and hole mobility values for all transistors will be calculated and statistically examined in Section 5.3.4.

Transmission line model analysis can be used in order to examine the behavior of large collections of SWNT network field effect transistors of high uniformity. The analysis of the device resistance can be made by determining the resistance of conduction pathways. For this purpose, semiconducting resistance (R_{ON}) is calculated with Ohm's Law using I_{ON}.

For the case in Figure 5.20, R_{ON} was calculated as $5.7\times10^6\ \Omega$. R_{ON} is the sum of channel and contact resistances:

$$R_{ON}= R_c + R_{CH} \tag{5.10}$$

In order to find the contact resistance, R_c, the following formula should be applied:

$$2R_c = \frac{V_{DS}}{I_{DS}} - \frac{V_{DS}}{g_{CH}(V_{GS}+V_{th})} \quad (5.11)$$

where g_{CH} is the conductance of channel formulated using the carrier mobility μ, dimensions of the channel and capacitance of the SiO_2 is calculated as 3.9×10^6 S for this example (g_{CH} = μ(W/L)C_{ox}).

V_{th} is the threshold voltage and is determined from the x−axis intercept from the plot of the square root of I_D measured in saturation versus V_G (Figure 5.24a). It is found to be −1.2V. This low value of V_{th} albeit the high operating voltage is at the first glance attributed to the use of doped Si substrate as the gate material. Its suitable work function and increased ion implantation through doping silicon results with a low V_{th}.

V_{th} is further used to calculate contact resistance (R_c) which is found to be 0.7×10^6 Ω (Equation 5.13). Consequently, channel resistance (R_{CH}) is found to be 5.1×10^6 Ω (Equation 5.12).

The results show that the gate voltage significantly modulates the conductance of the s−SWNTs and that the contact resistance is negligible compared to the channel resistance for L_{CH} larger than L_S (~600 nm) [129, 151].

Using the experimentally determined V_{th} the density of trapped charges ($n_{trapped}$) can be estimated by using the formula;

$$n_{trap} = \frac{(V_{th}\times C_i)}{e} \quad (5.12)$$

$n_{trapped}$ may also be estimated using the subthreshold slope (SS);

$$n_{trap} = C_i \times \left(\frac{SS}{kTln10} - \frac{1}{e}\right) \quad (5.13)$$

Here, $n_{trapped}$ is found to be 1×10^{26} (Equation 5.14) and subthreshold swing is calculated as 95 mV/decade (Equation 5.15). One of the key parameters that characterize the switching behavior of a field effect transistor is the sub–threshold swing (SS) which measures how fast a FET can be switched from an off current or off–state to an on current or on–state. In general, the smaller the SS is, the faster the FET. For an ideal Si–FET at room temperature, the theoretical value for SS is 60 mV/decade.

5.3.2 Percolation in SWNT Thin Films

Percolation theory deals with homogeneous infinite networks. For applications of SWNTs in transistors, due to electronic heterogeneity, anisotropic alignment and dimensionality of the thin films, non–linear and finite sized percolation models are needed for assessment of the properties. [142–145] Key parameters are average tube length (L_s) and transistor channel width (W).

In the linear response region of field effect transistor operation, intra–tube transport can be described using drift–diffusion theory [151]:

$$J=\frac{q\mu n\, d\varphi}{ds} \tag{5.14}$$

Where J is the current density along the tube, q is the carrier charge, μ is the charge mobility, n is carrier density, φ is electro-potential and s is the length of the tube. When combined with dJ/ds=0, the current density equation is described with φ_i (electro-potential along each tube i) according to

$$\frac{d^2\varphi_i}{ds^2}-c_{ij}(\varphi_i-\varphi_j)=0 \tag{5.15}$$

where C_{ij} is the charge transfer coefficient between tube i and j, which is the ratio of mutual and self–conductance of the tubes $C_{ij}=\frac{G_0}{G_1}$ [146].

Reflecting boundary conditions for W was set at the edges of the network. For transport in random networks, this approach can successfully predict the scaling behavior with channel width, channel length, and density of SWNTs [146, 147].

In the saturation region of device operation, the conductance of the channel is no longer a constant but is proven to have the same exponent term as the linear regime [148], therefore the following formula can be used for both regimes:

$$I_D = \frac{k}{L_s}\left(\frac{L_s}{L_{CH}}\right)^m \tag{5.16}$$

where L_{CH} is the channel length and L_S is the average distance between tube junctions. Coefficient k (A cm) depends on the charge transfer coefficient, the nanotube diameter, the oxide capacitance, the channel width and bias conditions, while exponent m depends on the coverage and anisotropy of SWNTs.

In random SWNT networks, where there are a lot of SWNT junctions forming several conductive paths (high SWNT density) and channel lengths (L_{CH}) that are significantly larger than the average distance between tube junctions (L_S), coverage of SWNTs is higher than percolation threshold and m is taken as 1. In this case, Equation 5.16 simplifies into Ohm's Law and the SWNT network behaves as a 3D conductor. Current scaling behavior and consequently the charge carrier mobilities are only weakly dependent on channel length.

When the coverage is lower than the percolation threshold, m is higher than 1. In this case, the current between source and drain depends highly on the channel length. A decrease in the channel length would make the production of the conduction paths easier, therefore I_{DS} would increase. Investigation of the dependence of I_{DS} on L_{CH} would be an easy way to

monitor if the percolation threshold for metallic and semiconducting tubes is already reached for SWNT networks.

As it can be seen from Figure 5.21a, there is a weak dependence of current on the channel length, where on current decreases with increasing L_{CH} due to the corresponding reduction in the electric field along the channel. A distinct increase of on−off current ratio with increasing L_{CH} would have pointed out that metallic percolation paths are present. Percolation paths of m−SWNTs can form electrical shorts across the channel shunting the semiconducting SWNTs and drastically decrease the off current independent of the applied gate voltage. In our case, where on−off current ratio stays constant with increasing L_{CH}, there are no metallic conduction paths between the source and drain and charge transport is dominated by thermally excited carriers which are also responsible for the high off currents shown in Figure 5.21b [151].

The influence of film thickness on device current is exhibited in Figure 5.22. There is an increase in the on current with increasing film thickness corresponding to the increase in conduction paths, which will be explained in detail. The distinct increase in the off current with increasing film thickness is steeper than the increase in Figure 5.21a. Off current is roughly corresponding to the sum of metallic pathways from the source to drain according to the basic threshold model. The absence of metallic pathways inside the channel is already proven. Therefore, a more accurate model is needed.

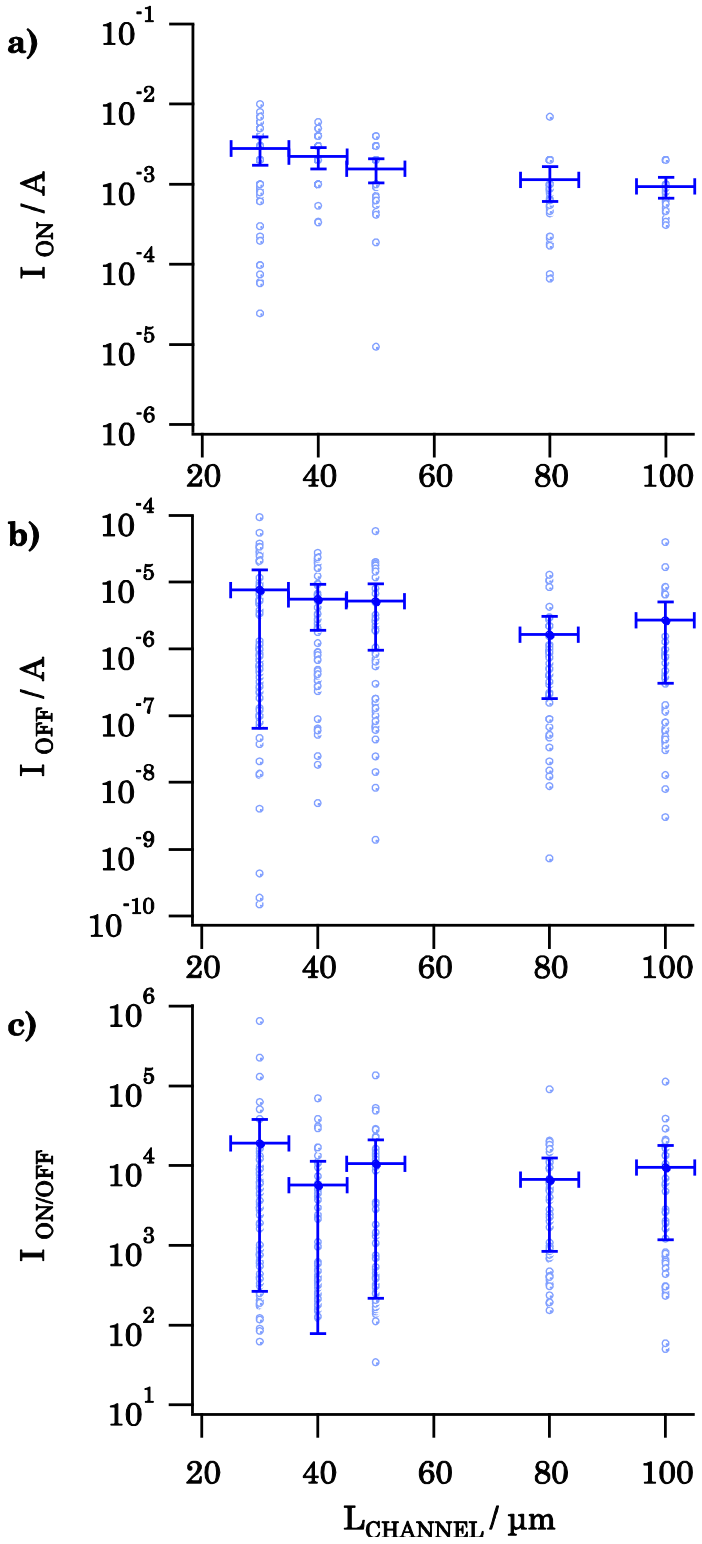

Figure 5.21: Course of on current, off current and on–off current ratio with increasing channel length for 270 field effect transistors. Semiconducting films of (6,5) SWNTs have a thickness in the range of 8 to 80 ± 5 nm.

According to the basic model, in an optimized channel, when the transistor is turned off, there is no conduction between drain and source. A more accurate model considers the effect of thermal energy on the Fermi–Dirac distribution of charge carrier energies which allow some more energetic charge carriers at the source enter the channel and flow to the drain. The result is the subthreshold current which increases exponentially with gate-source bias [153,154]:

$$I_D = I_{D_0} e^{\left(\frac{V_{GS}-V_{th}}{nV_T}\right)} \tag{5.17}$$

In the formula, I_{D_0} is the drain current when $V_{GS} = V_{th}$, V_T is the thermal voltage ($V_T = \frac{kT}{q}$) and $n = 1 + \frac{C_D}{C_{ox}}$ where C_{ox} is the capacitance of oxide layer C_D is the capacitance of depletion layer. Due to the last factor mentioned, the subthreshold current leakage causes off currents to increase with increasing SWNT film thickness [155,156]. Correspondingly, the on–off current ratio decreases with increasing film thickness (Figure 5.22c).

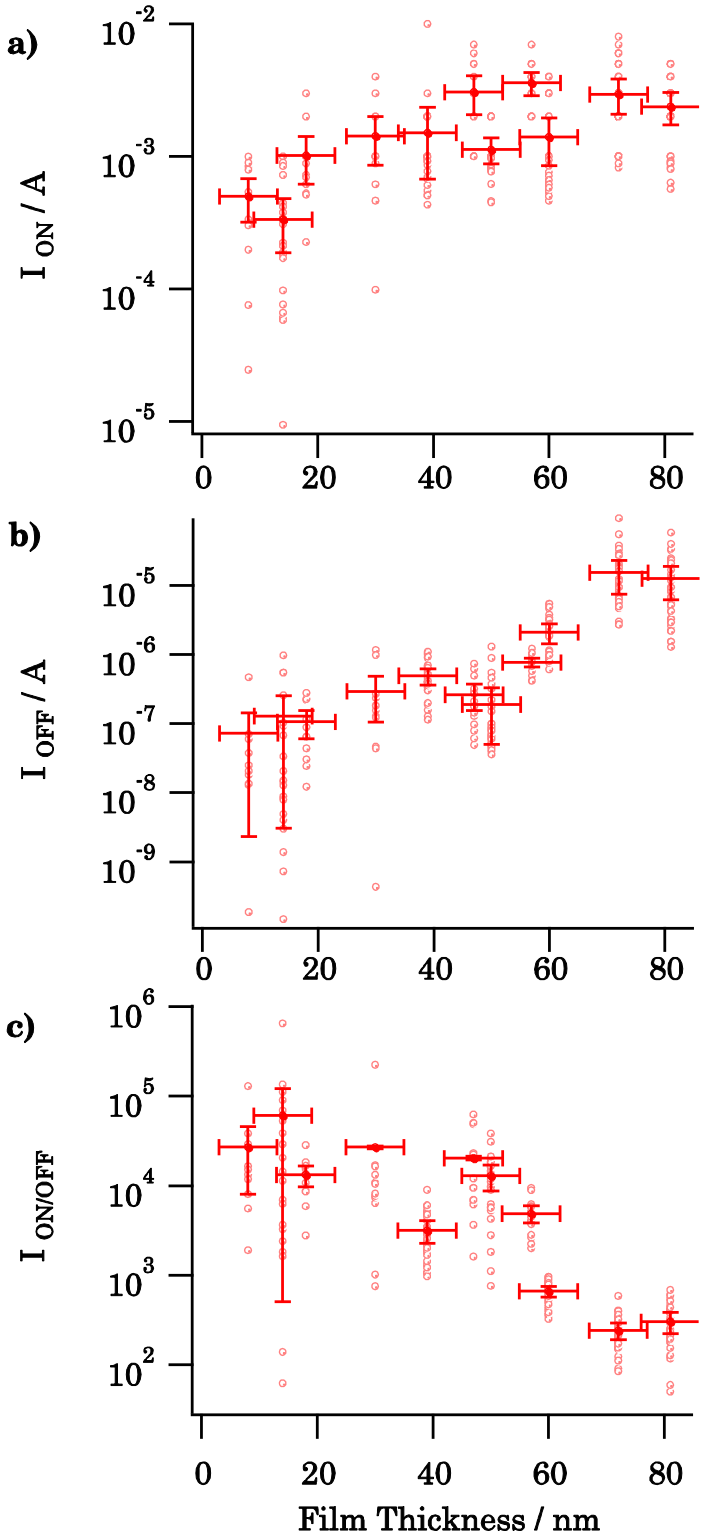

Figure 5.22: Course of on current, off current and on-off current ratio with increasing film thicknesses for 270 field effect transistors. Channel lengths of the transistors vary between 30 and 100 μm.

5.3.3 Hole Transport in SWNT Thin Films

Using Equation 5.21 and 5.22, linear and saturation hole mobility values for all 270 field effect transistors were calculated. As it can be seen in Figure 5.23, mobility in both regimes is correlated with SWNT thickness.

Charge carrier mobility is an intrinsic property and should be similar for every thickness value. However, the mobility of carriers is affected by the nature of the adjacent layer or surface. Even if the carrier does not transfer into the adjacent region, its wave function does extend over 1 to 10 nanometers, so that there is a non−zero probability that the particle is in the adjacent region. The net mobility is then a combination of the mobility in both layers. In this case, it is necessary to correct the mobility values for linear and saturation regimes with respect to increasing SWNT film thickness.

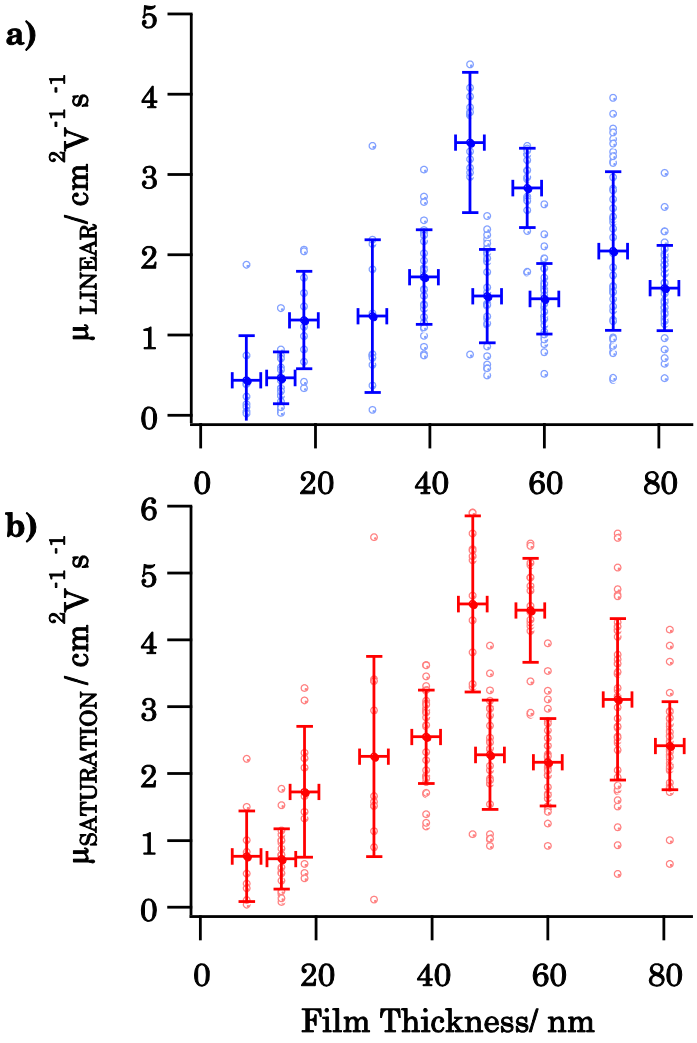

Figure 5.23: Linear and saturation regime hole mobilities for 270 field effect transistors with varying channel lengths from 30 to 100 μm. Mobilities are calculated using Equation 2.18 and 2.19 for SWNT films with varying thicknesses from 8 ± 5 to 80 ± 5 nm.

As it is already shown, contact resistance R_C is negligibly smaller than channel resistance R_{CH}, therefore, R_{ON} can be assumed to be equal to R_{CH}. The course of R_{CH} with increasing SWNT film thickness is shown in Figure 5.24. Here, the carrier mobility deserves further study since it is directly linked to the conductivity and resistivity of a semiconductor.

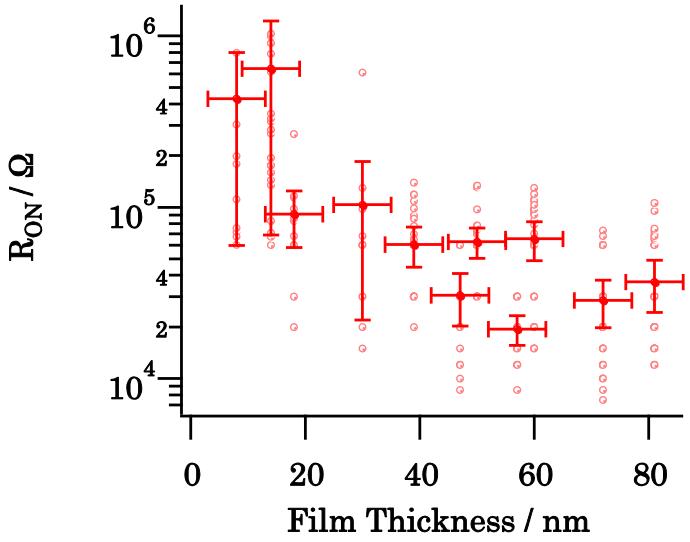

Figure 5.24: Decrease of R_{ON} with increasing film thickness for 270 field effect transistors with varying channel lengths from 30 to 100 μm.

According to the formula R=ρ (l/*A*), where ρ is the material specific electrical resistivity, l is the distance between two electrical contacts and *A* is the area of the cross-section, the resistance of a given object depends on two factors: the type of the material and its dimensions. In order to normalize for the effects of the dimension change of the semiconductor in field effect transistors (in the percolation conduction regime [151]), two dimensions of the resistor are considered: l, which corresponds to L_{CH} and W_{CH}. The thickness of the semiconductor is not included in the formula for charge carrier mobility calculations, which causes the increase.

As it was discussed in the dependence of off current on SWNT film thickness, carrier diffusion is due to the thermal energy, *kT*, which causes the carriers to move at random even when no field is applied. When the relation between the diffusion constant and the mobility is further explored, at first it seems that there should be no relation between the two since their driving forces are distinctly different. Diffusion is caused by

thermal energy while an externally applied field causes drift. However, they have a common parameter of collision time which is independent of the carrier motion. The total current is obtained by subtracting the current due to diffusion from the drift current. Subtracting an exponentially increasing data set from a linearly increasing one would end up contributing to the power dependence of mobility on film thickness.

A fit for hole mobilities, with increasing film thickness, is shown in Figure 5.25. Pearson correlation coefficient analysis [169] was performed for assessing the validity of the power fit to the data. In this analysis, coefficient values range from −1 to +1, +1 meaning a total correlation between two sets of data. A coefficient of 0.62 was found between the fit and the mobility data, which shows a good correlation, meaning that mobility increases with the power law with increasing film thickness.

The equations of the fit for linear and saturation regime mobilities are:

$$\mu_{LINEAR} = (0.16 \pm 0.14)\ (\text{Thickness})^{0.59 \pm 0.22} \quad (5.18)$$

$$\mu_{SATURATION} = (0.27 \pm 0.20)\ (\text{Thickness})^{0.57 \pm 0.19} \quad (5.19)$$

This effect is important in order to interpret mobility values reported from films with different thicknesses for the transistors in the percolation conduction regime. This effect applies distinctly to thinner films and starts slowly to saturate for thicker films. As most of the transistors are prepared by methods resulting in films thinner than 10's of nm's, careful consideration and correction for the film thickness and comparison with the reported values should be done.

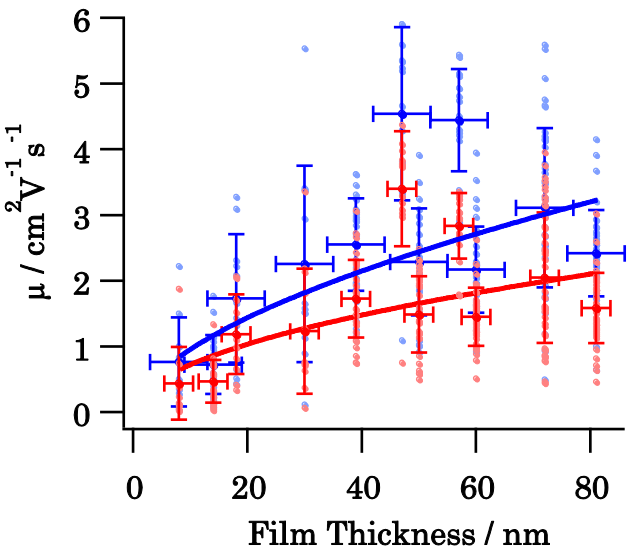

Figure 5.25: The course of linear and saturation regime hole mobilities with increasing film thickness.

5.4 Summary of Optical and Electronic Transport Properties of 8 to 755 nm thick (6,5) SWNT film Networks

In this chapter, PFOBPy wrapped (6,5) SWNT thin films were prepared using vacuum filtration wet transfer film fabrication. The thicknesses of the films were varied between 18 ± 5 to 755 ± 5 nm on glass or sapphire substrates and between 8 ± 5 and 80 ± 5 nm on SiO_2 substrates by changing the filtrate volume. Optical properties of films on glass substrate were examined by absorption and photoluminescence spectroscopy.

The topography of the films was characterized by AFM and SEM measurements. Resembling topographic images and constant roughness values were obtained for thin and thick films. The optical density of the films, as well as the number of carbon nanotubes per film, was found to increase linearly with increasing film thickness. In addition to all these, volume fractions of SWNTs for the prepared vacuum filtration thin films were found to be almost constant for all of the films, pointing out the

homogeneity of the obtained films and scalability of this thin film fabrication method successfully for a wide range of thicknesses.

Photoluminescence of the S_1 transition of PFOBPy wrapped (6,5) SWNTs on the film was monitored. Enhanced appearance of side peaks, which was found to be due to the K point phonon−photon coupling was studied. The enhancement was attributed to the reabsorption effect which gets more emphasized with thicker films. Necessary corrections were made on the photoluminescence spectra of the SWNT thin films in order to obtain central wavelengths, peak widths and relative photoluminescence quantum yields from the transition peaks. The yield of the radiative decay, which was decreasing gradually before reabsorption corrections, stayed almost constant through the whole thickness range. A blue shift in the transition maxima was complemented with a decrease in FWHM with increasing film thickness.

In low-temperature photoluminescence measurements, photoluminescence intensity was found to decrease with decreasing temperature. There was a dip in the intensities around 50 K which was already reported in the literature [126]. Surprisingly, for tightly packed PFOBPy wrapped (6,5) SWNT films, the PL intensities were not close to zero for temperatures below this dip, which was attributed to the slow exciton scattering between the bright and dark states due to polymer wrapping. A red shift in the photoluminescence maxima was observed when going to lower temperatures and the magnitude of the redshift was correlated with the thickness of the film, thicker films having a high dielectric screening of the Coulomb interaction in the nanotube through its environment.

Electronic properties of PFOBPy wrapped (6,5) monochiral SWNT films were measured by constructing bottom gate top contact field effect transistors with increasing semiconductor thickness. Transfer and output characteristics of 270 transistors were analyzed in order to find out the percolation behavior and charge carrier mobility of the SWNT films with

increasing thickness. Strong p−type behavior was observed in all transistors. Hysteresis, which is due to adsorbents on the semiconductor-dielectric interface, was reduced with respect to the spin-coated thin films.

With a transmission line model analysis, contact resistances were found to be negligibly smaller than the channel resistance that is caused by the tube junctıons inside the SWNT films. Consecutively, a high operating voltage (−60V) was needed. In order to obtain reasonable device efficiencies, Si^{++} was used as a back gate which enabled a low threshold voltage of −1.2 V for the examined transistor. The subthreshold slope for the same transistor was calculated to be 95 mV/decade, which is a promising switching time for an SWNT transistor.

Percolation behavior of the SWNTs was analyzed by monitoring the dependence of on and off currents with respect to increasing channel length. In literature, it was reported that three regimes for percolation behavior exist and due to the independence of on and off currents from channel length, transistors in this study were found to be operating in the regime where thermally excited charge carriers are transported. This contributes to the increasing off current with increasing junction depth and the resulting diffusion of electrons plays an important role in the course of hole mobilities.

Surprisingly, hole mobilities for linear and saturation regimes were found to be increasing in the thickness scale which was explained as the effect of decreasing R_{ON} and increasing thermal electron diffusion acting against each other for the porous SWNT films. These results are important in order to interpret the mobility values reported for SWNT field effect transistors. It is crucial to correct the mobility values for the thickness of the SWNT thin film in order to eliminate the artificially high mobility values and focus on the structural limitations on reaching bulk mobility values.

6. Summary

In order to shrink the size of semiconductor devices and improve their efficiency at the same time, silicon-based semiconductor devices have been engineered, until the material almost reaches its performance limits. As the candidate to be used next in semiconducting devices, single-wall carbon nanotubes show a great potential due to their promise of increased device efficiency and their high charge carrier mobilities in the nanometer size active areas. However, there are material based problems to overcome in order to imply SWNTs in the semiconductor devices. SWNTs tend to aggregate in bundles and it is not trivial to obtain an electronically or chirally homogeneous SWNT dispersion and when it is done, a homogeneous thin film needs to be produced with a technique that is practical, easy and scalable. This work was aimed to solve both of these problems.

In the first part of this study, six different polymers, containing fluorene or carbazole as the rigid part and bipyridine, bithiophene or biphenyl as the accompanying copolymer unit, were used to selectively disperse semiconducting SWNTs. With the data obtained from absorption and photoluminescence spectroscopy of the corresponding dispersions, it was found out that the rigid part of the copolymer plays a primary role in determining its dispersion efficiency and electronic sorting ability. Within the two tested units, carbazole has a higher π electron density. Due to increased π–π interactions, carbazole containing copolymers have higher dispersion efficiency. However, the electronic sorting ability of fluorene containing polymers is superior. Chiral selection of the polymers in the dispersion is not directly foreseeable from the selection of backbone units. At the end, obtaining a

monochiral dispersion is found to be highly dependent on the used raw material in combination to the preferred polymer.

Next, one of the best performing polymers due to high chirality enrichment and electronic sorting ability was chosen in order to disperse SWNTs. Thin films of varying thickness between 18 ± 5 to 755 ± 5 nm were prepared using vacuum filtration wet transfer method in order to analyze them optically and electronically.

The scalability and efficiency of the integrated thin film production method were shown using optical, topographical and electronic measurements. The relative photoluminescence quantum yield of the radiative decay from the SWNT thin films was found to be constant for the thickness scale. Constant roughness on the film surface and linearly increasing concentration of SWNTs were also supporting the scalability of this thin film production method. Electronic measurements on bottom gate top contact transistors have shown an increasing charge carrier mobility for linear and saturation regimes. This was caused by the missing normalization of the mobility for the thickness of the active layer. This emphasizes the importance of considering this dimension for comparison of different field effect transistor mobilities.

7. Zusammenfassung

Um die Verkleinerung in Halbleiterbauelementen zu erreichen und gleichzeitig ihre Effizienz zu verbessern, wurden Halbleiter-bauelemente auf Siliziumbasis entwickelt, bis das Material seine Leistungsgrenzen nahezu erreicht hat. Als zukünftiger Kandidat, der in halbleitenden Geräten Verwendung finden wird, zeigen einwandige Kohlenstoff–Nanoröhren ein großes Potenzial für eine erhöhte Geräteeffizienz. Grund dafür sind ihre hohen Ladungsträger–Mobilitäten in den ein paar Nanometergroßen aktiven Flächen. Allerdings gibt es materialbasierte Probleme zu überwinden um SWNTs in den Halbleiterbauelementen zu implizieren. SWNTs neigen dazu in Bündeln zu aggregieren. Eine Herausforderung ist zudem eine elektronische oder chiral homogene Kohlenstoffnanorohr–Dispersion zu erhalten. Ein weiteres Problem ist, aus diesen Kohlenstoffnanorohr–Dispersion einen homogenen Dünn–Film mit einer Technik herzustellen die praktisch, einfach und skalierbar ist. Diese Arbeit zielte darauf ab, diese beiden Probleme zu lösen.

Im ersten Teil dieser Arbeit wurden sechs verschiedene Polymere, die Fluoren oder Carbazol als starren Teil und Bipyridin, Bithiophen oder Biphenyl als begleitende Copolymereinheit enthielten, verwendet um selektiv halbleitende SWNTs zu dispergieren. Mit den aus der Absorptions– und Photolumineszenzspektroskopie erhaltenen Daten der entsprechenden Dispersionen wurde herausgefunden, dass der starre Teil des Copolymers eine primäre Rolle bei der Bestimmung seiner Dispersionseffizienz und der elektronischen Sortierfähigkeit spielt. Innerhalb der beiden getesteten Einheiten hat Carbazol eine höhere π–Elektronendichte. Aufgrund erhöhter π–π Wechselwirkungen

haben Carbazol–haltige Copolymere eine höhere Dispersionseffizienz. Die elektronische Selektivität von fluorenhaltigen Polymeren ist gegenüber Carbazol enthaltenden Polymeren höher. Die chirale Selektivität der Polymere in der Dispersion ist nicht direkt vor der Auswahl der Grundgerüsteinheiten vorhersehbar. Am Ende wird das Erhalten einer monochiralen Dispersion im hohen Maße von den verwendeten Rohmaterialien in Kombination mit dem bevorzugten Polymer abhängig gemacht.

Im nächsten Schritt wurde ein Polymer ausgewählt der durch eine hohe Chiralitätanreicherung besticht und zudem eine gute elektronische Sortierfähigkeit besitzt, um SWNTs zu dispergieren. Dünnfilme unterschiedlicher Dicke, zwischen 18 ± 5 bis 755 ± 5 nm, wurden unter der Verwendung eines Vakuumfiltrations–Nassübertragungsverfahrens hergestellt um sie daraufhin optisch und elektronisch zu analysieren.

Die Skalierbarkeit und Effizienz des integrierten Dünnschicht-herstellungsverfahrens wurde anhand optischer, topographischer und elektronischer Messungen gezeigt. Die relative Photolumineszenz-quantenausbeute des Strahlungsabfalls aus den SWNT–Dünnfilmen wurde für den Dickenmaßstab konstant gehalten. Eine konstante Rauigkeit auf der Filmoberfläche und eine linear zunehmende Konzentration von SWNTs unterstützten auch die Skalierbarkeit dieses Dünnfilmherstellungsverfahrens. Elektronische Messungen am „bottom gate – top contact Transistoren“ zeigten eine zunehmende Ladungs-trägermobilität für Linear– und Sättigungsregionen. Dies wurde durch die fehlende Normalisierung der Ladungsträgermobilität für die Dicke der aktiven Schicht verursacht. Betrachtet man die Wichtigkeit, diese Dimension für den Vergleich verschiedener Feldeffekttransistor–Mobilitäten zu betrachten, so deutet diese Feststellung auch darauf hin, dass es eine Skalierung in der Dicke in Bezug auf die berechneten Mobilitäten für die Feldeffekttransistoren gibt.

8. Acknowledgments

I would like to start by thanking my supervisor Prof. Tobias Hertel here for the chance he gave me to do my Ph.D. in his research group at the Institute of Physical and Theoretical Chemistry in University of Würzburg, Germany. I very much appreciate his help and guidance throughout the last 3 years for my scientific and personal development. Also thanks to him, I was part of an EU Marie Curie research project, called POCAONTAS and I was able to meet and share information with researchers and academicians from all over the world. I would like to thank all my project colleagues, especially Prof. Achim Hartschuh, Xian Shi, Prof. Jorge Morgado, Rajesh Veeravarapu, Prof. Thomas Anthopoulos, Francesca Bottacchi, Mirella El Gemayel, Prof. Vladimir Dyakonov and Alexey Gavrik for their help and the cooperation we held that made this work possible.

I would like to give big thanks to all of my colleagues and friends, who were a part of Hertel Research Group and who made it twice interesting to wake up and go to the lab in the morning. I have special thanks to Dr. Florian Späth and Dr. Friedrich Schöppler who always took time for me when I needed; for my questions during my Ph.D. and for the correction of this dissertation. Being so lucky, my office−mates, Dr. Florian Späth, Dr. Nicolas Rühl, Dr. Han Li, Kerstin Müller and Melanie Achsnich were always very friendly, helpful, understanding and kind to me. In addition to them, I cannot go on without mentioning Sabine Stahl, Matthias Kastner, Klaus Eckstein, Florian Oberndorfer and Pascal Kunkel, with whom I shared a lot of nice moments through my years in Würzburg. I would like to thank all of them for the fun we had and for the scientific problems, we solved together, both at work at lunchtime or at the evening by drinking beer.

I especially thank Sabine Walther for her competent and helpful attitude against all my administrative challenges. It was our luck that Sabine Fuchs, Belinda Böhm, as well as Peter Lang, Rainer Eck, Wolfgang Liebler and Katharina Schreckling were always there to help us with the technical problems.

Lastly, I would like to thank the most important people in my life; my boyfriend, my brother, my mom and my dad. I would like to start with my boyfriend, Matthias Schmitt who was there almost the whole time and always supporting me, helping in any way he could. I am very grateful that I have been sharing a life with him for the last 4 years.

I cannot imagine my life without my brother, Berk Namal, who is my "the partner in crime" since I was 5, my mom Fatma Namal who is my great teacher and role model in being ambitious and hardworking and my dad, Nedim Namal, who taught me how to take it easy and take a step back and rethink in the moments of crisis. I am thankful that they were always supportive and loving. I was strong in my hardest moments because I knew that I have them on my side.

9. References

[1]http://www.grandviewresearch.com/industry-analysis/personal-consumer-electronics-market

[2] C. Macilwain: Computer Hardware: Silicon Down to the Wire, Nature, 436, 22-23 (2005)

[3] Javey, A., Guo, J., Wang, Q., Lundstrom, M. & Dai, H.: Ballistic carbon nanotube transistors, Nature 424, 654–657 (2003).

[4] Javey, A., Wang, Q., Kim, W. & Dai, H. in 2003 Intl Electron Devices Meeting Tech. Digest 31–32 (IEEE, 2003).

[5] Appenzeller, J.: Carbon nanotubes for high-performance electronics—progress and prospect.: Proc. IEEE 96, 201–211 (2008).

[6] S. Iijima, T. Ichihashi, Nature, 363, 603(1993)

[7] R. Martel, T. Schmidt, H. R. Shea, T. Hertel, P. Avouris: Single- and multiwall carbon nanotube field-effect transistors, Appl. Phys. Lett. 73, 2447–2449 (1998) 455, 463, 467

[8] S.J. Tan, et al. Nature 386 (1998) 474.

[9] F. Kreupl, Nature 501 (2013) 495.

[10] M.M. Shulaker, et al. Nature 501 (2013) 526.

[11] P. Avouris, Z. Chen, V. Perebeinos, Carbon-based electronics, Nat. Nanotechnol. 2 (2007)605—615

[12] Chen, Fuming, Bo Wang, Yuan Chen, und Lain−Jong Li. „Toward the Extraction of Single Species of Single−Walled Carbon Nanotubes Using Fluorene−Based Polymers“. Nano Letters 7, Nr. 10 (1. Oktober 2007): 3013–17. doi:10.1021/nl071349o.

[13] A. Nish, J.−Y. Hwang, J. Doig, R.J. Nicholas, Nat. Nanotechnol.2 (2007) 640—646.]

[14] H. Ozawa, N. Ide, T. Fujigaya, Y. Niidome, N. Nakashima, One−pot Separation of Highly Enriched (6,5)−Single−walled Carbon Nanotubes Using a Fluorene−based Copolymer, Chem. Lett. 40 (2011) 239–241, DOI: 10.1246/cl.2011.239.

[15] J.−Y. Hwang, A. Nish, J. Doig, S. Douven, C.−W. Chen, L.−C. Chen, R. J.Nicholas, Polymer Structure and Solvent Effects on the Selective Dispersion of Single−Walled Carbon Nanotubes, J. Am. Chem. Soc. 130 (2008) 3543–3553, DOI: 10.1021/ja0777640

[16] Effect of Solvent Solubility Parameters on the Dispersion of Single−Walled Carbon Nanotubes Qiaohuan Cheng, Sourabhi Debnath, Elizabeth Gregan, and Hugh J. Byrne The Journal of Physical Chemistry C 2008 112 (51), 20154−20158 DOI: 10.1021/jp8067188

[17] S. J. Wind, J. Appenzeller, R. Martel, V. Derycke, P. Avouris: Vertical scaling of carbon nanotube field−effect transistors using top gate electrodes, Appl. Phys. Lett. 80, 3817–3819 (2002) 467

[18] K.S. Mistry, B.A. Larsen, J.L. Blackburn, High-yield dispersions of large-diameter semiconducting single-walled carbon nanotubes with tunable narrow chirality distributions ACS Nano 7 (2013)2231—2239.

[19] J. Gao, R. Annema, M. Loi, Tuning the physical parameters towards optimal polymer−wrapped single−walled carbon nanotubes dispersions, Eur. Phys. J. B 85 (2012) 1–5, DOI: 10.1140/epjb/e2012−30120−5.

[20] M. J. Shea, R. D. Mehlenbacher, M. T. Zanni, M. S. Arnold, Experimental Measurement of the Binding Configuration and Coverage of Chirality– Sorting Polyfluorenes on Carbon Nanotubes, J. Phys. Chem. Lett. 5 (2014) 3742–3749, DOI: 10.1021/jz5017813.

[21] Ding, J.; Li, Z.; Lefebvre, J.; Cheng, F.; Dubey, G.; Zou, S.; Finnie, P.; Hrdina, A.; Scoles, L.; Lopinski, G. P.; et al Enrichment of Large–diameter Semiconducting CNTs by Polyfluorene Extraction for High Network Density Thin Film Transistors. Nanoscale 2014, 6, 2328–39

[22] Rice, N. A. and Adronov, A. (2014), Selective interactions of a high–molecular–weight polycarbazole with different commercial nanotube samples. J. Polym. Sci. Part A: Polym. Chem., 52: 2738–2747. doi:10.1002/pola.27292

[23] E. Joselevich, H. Dai, J. Liu, K. Hata, A. H. Windle, *Carbon Nanotube Synthesis and Organization*, in *Topics in Applied Physics*, 111, pp. 101–164, Springer Berlin Heidelberg (2008).

[24] King, Benjamin, and Balaji Panchapakesan. "Vacuum Filtration Based Formation of Liquid Crystal Films of Semiconducting Carbon Nanotubes and High Performance Transistor Devices." Nanotechnology 25, no. 17 (2014): 175201.

[25] Wu, Z., et al. (2004). "Transparent, Conductive Carbon Nanotube Films." Science 305(5688): 1273-1276.

[26] R. B. Weisman, S. M. Bachilo, Dependence of Optical Transition Energies on Structure for Single–Walled Carbon Nanotubes in Aqueous Suspension: An Empirical Kataura Plot, Nano Lett. 3, 1235–1238 (2003).

[27] Fried J.R. "Polymer Science and Technology" (Pearson Prentice–Hall, 2nd edn 2003), p.27 ISBN 0–13–018168–4

[28] Xu et al. J. Phys. Chem. B 114, 11746–11752 (2010)

[29] A. D. McNaught and A. Wilkinson, IUPAC. Compendium of Chemical Terminology, the "Gold Book", Blackwell Scientific Publications, 2. Auflage, 1997, DOI:10.1351/goldbook

[30] Knaapila, M., D. W. Bright, R. Stepanyan, M. Torkkeli, L. Almásy, R. Schweins, U. Vainio, u. a. 2011. „Network Structure of Polyfluorene Sheets as a Function of Alkyl Side Chain Length". *Physical Review E* 83 (5). doi:10.1103/PhysRevE.83.051803.

[31]Chen, Jean−Hong, Chih−Shun Chang, Ying−Xun Chang, Chun−Yu Chen, Hsin−Lung Chen, und Show−An Chen. 2009. „Gelation and Its Effect on the Photophysical Behavior of Poly(9,9−Dioctylfluorene−2,7−Diyl) in Toluene". *Macromolecules* 42 (4): 1306–14. doi:10.1021/ma802408u.

[32] I. D. Morrison, S. Ross, *Colloidal Dispersions: Suspensions, Emulsions, and Foams*, 1. Auflage, John Wiley & Sons, New York, NY 2002.

[33] T. F. Tadros, *Polymer Surfactants*, in K. Holmberg (Hrsg.), *Handbook of Applied Surface and Colloid Chemistry*, Band 1, 1. Auflage, John Wiley & Sons, Chichester 2001.

[34] Jeng E S, Moll A E, Roy A-C, Gastala J B, and Strano M S 2006 Nano Lett. 6 371

[35] Fujigaya T, Yamamoto Y, Kano A, Maruyama A and Nakashima N 2011 Nanoscale 3 4352

[36] Stranks S D, Habisreutinger S N, Dirks B and Nicholas R J 2013Adv. Mater.25 4365

[37] Okamoto M, Fujigaya T and Nakashima N 2009 Small 5 735

[38] Izard N, Kazaoui S, Hata K, Okazaki T, Saito T, Iijima S and Minami N 2008 Appl. Phys. Lett. 92 243112

[39] Bisri S Z, Gao J, Derenskyi V, Gomulya W, Iezhokin I, Gordiichuk P, Herrmann A and Loi M A 2012 Adv. Mater. 24 6147

[40] Chen J, Liu H, Weimer W A, Halls M D, Waldeck D H and Walker G C 2002 J. Am. Chem. Soc. 124 9034

[41] J.−C. Charlier, X. Blase, and S. Roche, Electronic and transport properties of nanotubes, Reviews of Modern Physics 79, 677–732 (2007)

[42] J.−Y. Hwang, A. Nish, J. Doig, S. Douven, C.−W. Chen, L.−C. Chen, R.J. Nicholas, J. Am. Chem. Soc. 130 (2008)3543—3553.

[43] Berton, Nicolas, Fabien Lemasson, Angela Poschlad, Velimir Meded, Frank Tristram, Wolfgang Wenzel, Frank Hennrich, Manfred M. Kappes, and Marcel Mayor. 2014. „Selective Dispersion of Large−Diameter Semiconducting Single−Walled Carbon Nanotubes with Pyridine−Containing Copolymers“. Small 10 (2): 360–67. doi:10.1002/smll.201301295.

[44] Gu, Jianting, Jie Han, Dan Liu, Xiaoqin Yu, Lixing Kang, Song Qiu, Hehua Jin, Hongbo Li, Qingwen Li, and Jin Zhang. “Solution−Processable High−Purity Semiconducting SWCNTs for Large−Area Fabrication of High−Performance Thin−Film Transistors.” Small 12, no. 36 (September 2016): 4993–99. doi:10.1002/smll.201600398.

[45] Andor an Oxford Instruments Company. 2017. *Spectroscopy Solutions A Modular Approach*. [ONLINE] Available at: http://www.andor.com/pdfs/literature/Andor_Spectroscopy_Brochure.pdf. [Accessed 14 February 2017]

[46] Hain, TC, 2015. Entwicklung eines Experimentellen Aufbaus zur charakterizierung nanoskaliger systeme. PhD. Würzburg: University of Würzburg

[47]Richard, Cyrille, Fabrice Balavoine, Patrick Schultz, Thomas W. Ebbesen, and Charles Mioskowski. „Supramolecular Self−Assembly of Lipid Derivatives on Carbon Nanotubes“. Science 300, Nr. 5620 (2003): 775–78.

[48] S. Duesberg, G., M. Burghard, J. Muster, and G. Philipp. „Separation of carbon nanotubes by size exclusion chromatography“. Chemical Communications, Nr. 3 (1998): 435–36. doi:10.1039/A707465D.

[49] Burghard, Marko, Georg Duesberg, Guenther Philipp, Joerg Muster, and Siegmar Roth. „Controlled Adsorption of Carbon Nanotubes on Chemically Modified Electrode Arrays“. Advanced Materials 10, Nr. 8 (1998): 584–88.

[50] Islam, M. F., E. Rojas, D. M. Bergey, A. T. Johnson, and A. G. Yodh. „High Weight Fraction Surfactant Solubilization of Single−Wall Carbon Nanotubes in Water“. Nano Letters 3, Nr. 2 (1. February 2003): 269–73. doi:10.1021/nl025924u.

[51] Paredes, J. I., and M. Burghard. „Dispersions of Individual Single−Walled Carbon Nanotubes of High Length“. Langmuir 20, Nr. 12 (1. Juni 2004): 5149–52. doi:10.1021/la049831z.

[52] Moore, Valerie C., Michael S. Strano, Erik H. Haroz, Robert H. Hauge, Richard E. Smalley, Judith Schmidt, and Yeshayahu Talmon. „Individually Suspended Single−Walled Carbon Nanotubes in Various Surfactants“. Nano Letters 3, Nr. 10 (1. October 2003): 1379–82. doi:10.1021/nl034524j.

[53] Hough, L. A., M. F. Islam, B. Hammouda, A. G. Yodh, and P. A. Heiney. „Structure of Semidilute Single−Wall Carbon Nanotube Suspensions and Gels“. Nano Letters 6, Nr. 2 (1. February 2006): 313–17. doi:10.1021/nl051871f.

[54] Islam M F, Nobili M, Ye F, Lubensky T C and Yodh A G 2005 Phys. Rev. Lett. 95 148301 /1

[55] Ishibashi A and Nakashima N 2006 Chem. Eur. J. 12 7595

[56] Ishibashi A and Nakashima N 2006 Bull. Chem. Soc. Jpn.79 357

[57] Wenseleers W, Vlasov I I, Goovaerts E, Obraztsova E D, Lobach A S and Bouwen A 2004 Adv. Funct. Mater. 14 1105

[58] Kim Y, Hong S, Jung S, Strano M S, Choi J and Baik S 2006 J. Phys. Chem. B 110 1541

[59] Lisunova M O, Lebovka N I, Melezhyk O V and Boiko Y P 2006 J. Colloid Interface Sci. 299 740

[60] M.S. Arnold, A.A. Green, J.F. Hulvat, S.I. Stupp, M.C. Hersam,Nat. Nano 1 (2006) 60—65.

[61] T. Tanaka, H. Jin, Y. Miyata, S. Fujii, H. Suga, Y. Naitoh, T.Minari, T. Miyadera, K. Tsukagoshi, H. Kataura, Nano Lett. 9(2009) 1497—1500.

[62] S. Ghosh, S.M. Bachilo, R.B. Weisman, Nat. Nanotechnol. 5(2010) 443—450.

[63] H. Liu, D. Nishide, T. Tanaka, H. Kataura, Nat. Commun. 2(2011).

[64] C.Y. Khripin, J.A. Fagan, M. Zheng, J. Am. Chem. Soc. 135(2013) 6822—6825.

[65] J.A. Fagan, C.Y. Khripin, C.A. Silvera Batista, J.R. Simpson,E.H. Hároz, A.R. Hight Walker, M. Zheng, Adv. Mater. 26 (2014)2800—2804.

[66] Xia, Jiye, Guodong Dong, Boyuan Tian, Qiuping Yan, Han Zhang, Xuelei Liang, and Lianmao Peng. “Metal Contact Effect on the Performance and Scaling Behavior of Carbon Nanotube Thin Film Transistors.” Nanoscale 8, no. 19 (2016): 9988–96. doi:10.1039/C6NR00876C.

[67] S. J. Tans, A. R, M. Verschueren, C. Dekker: Room−temperature transistor based on a single carbon nanotube, Nature 393, 49–52 (1998) 455, 463, 467

[68] Q. Wang and H. Moriyama: Carbon Nanotube-Based Thin Films: Synthesis and Properties, InTech, (2011).DOI: 10.5772/22021.

[69] A. Javey, H. Kim, M. Brink, Q. Wang, A. Ural, J. Guo, P. McIntyre, P. McEuen, M. Lundstrom, H. J. Dai: High−kappa dielectrics for advanced carbon−nanotube transistors and logic gates, Nature Mater. 1, 241–246 (2002) 467, 468

[70] A. Javey, J. Guo, D. B. Farmer, Q. Wang, E. Yenilmez, R. G. Gordon, M. Lundstrom, H. J. Dai: Self−aligned ballistic molecular transistors and electrically parallel nanotube arrays, Nano Lett. 4, 1319–1322 (2004) 467

[71] F. Jakubka, S. P. Schießl, S. Martin, J. M. Englert, F. Hauke, A. Hirsch, J. Zaumseil, Effect of Polymer Molecular Weight and Solution Parameters on Selective Dispersion of Single−Walled Carbon Nanotubes, ACS Macro Lett. 1 (2012) 815–819, DOI: 10.1021/mz300147g.

[72] A. Javey, J. Guo, D. B. Farmer, Q. Wang, D. W. Wang, R. G. Gordon, M. Lundstrom, H. J. Dai: Carbon nanotube field−effect transistors with integrated ohmic contacts and high−k gate dielectrics, Nano Lett. 4, 447–450 (2004) 467

[73] O.Lee, J.Jung, S.Doo, S.−S. Kim, T.−H. Noh, K.−I. Kim, Y.−S. Lim, Effects of Temperature and Catalysts on the Synthesis of Carbon Nanotubes by Chemical Vapor Deposition, Met. Mater. Int, 16(4), 2010, pp. 663−667.

[74] R. Sharma, S.−W. Chee, A.Herzing, R.Miranda, P. Rez, Evaluation of the role of Au in Improving Catalytic Activity of Ni Nanoparticles for the Formation of One−Dimensional Carbon Nanostructures, *Nano Letter*s, 11, 2011, pp.2464−2471.

[75] R.L. Vander Wal, T. M. Ticich, V.E. Curtis, Substrate–support interactions in metal-catalyzed carbon nanofiber growth, Carbon, 39, 2001, pp. 2277–2289.

[76] B. Shukla, T. Saito, S. Ohmori, M. Koshi, M. Yumura, S. Iijima, Interdependency of Gas Phase Intermediates and Chemical Vapor Deposition Growth of Single-Wall Carbon Nanotubes, Chemistry of Materials, 22, 2010, 6035–6043.

[77] Rice, N. A., Subrahmanyam, A. V., Laengert, S. E. and Adronov, A. (2015), The effect of molecular weight on the separation of semiconducting single–walled carbon nanotubes using poly(2,7–carbazole)s. J. Polym. Sci. Part A: Polym. Chem., 53: 2510–2516. doi:10.1002/pola.27715

[78] Gomulya, W.; Costanzo, G. D.; de Carvalho, E. J. F.; Bisri, S. Z.; Derenskyi, V.; Fritsch, M.; Fröhlich, N.; Allard, S.; Gordiichuk, P.; Herrmann, A.; et al. Semiconducting Single–Walled Carbon Nanotubes on Demand by Polymer Wrapping. Adv. Mater. 2013, 25, 2948–2956.

[79]Nish, A.; Hwang, J. Y.; Doig, J.; Nicholas, R.J. Direct Spectroscopic Evidence of Energy Transfer from Photo–Excited Semiconducting Polymers to Single–Walled Carbon Nanotubes. Nanotechnology 2008, 19, 095603

[80] S.M. Bachilo, L. Balzano, J.E. Herrera, F. Pompeo, D.E. Resasco, R.B. Weisman, Narrow (n,m)–distribution of single–walled carbon nanotubes grown using a solid supported catalyst. J. Am. Chem. Soc. 125(37), 11186–11187 (2003). doi:10.1021/ja036622c

[81] Dependence of Optical Transition Energies on Structure for Single–Walled Carbon Nanotubes in Aqueous Suspension: An Empirical Kataura Plot R. Bruce Weisman* and Sergei M. Bachilo Nano Lett., Vol. 3, No. 9, 2003

[82] Naumov, A. V.; Ghosh, S.; Tsyboulski, D. A.; Bachilo, S. M.; Weisman, R. B. ACS Nano 2011, 5, 1639– 1648, DOI: 10.1021/nn1035922

[83] Hertel, Tobias, Sabine Himmelein, Thomas Ackermann, Dominik Stich, and Jared Crochet. „Diffusion Limited Photoluminescence Quantum Yields in 1–D Semiconductors: Single–Wall Carbon Nanotubes“. ACS Nano 4, Nr. 12 (28. December 2010): 7161–68. doi:10.1021/nn101612b.

[84] Energy Transfer from Photo–Excited Fluorene Polymers to Single–Walled Carbon Nanotubes FuMing Chen, Wenjing Zhang, Mingli Jia, Li Wei, Xiao–Feng Fan, Jer–Lai Kuo, Yuan Chen, Mary B. Chan–Park, Andong Xia, and Lain–Jong Li The Journal of Physical Chemistry C 2009 113 (33), 14946–14952 DOI: 10.1021/jp904431u

[85] Lebedkin, S.; Hennrich, F.; Kiowski, O.; Kappes, M. M. Photophysics of Carbon Nanotubes in Organic Polymer–Toluene Dispersions: Emission and Excitation Satellites and Relaxation Pathways. Phys. Rev. B: Condens. Matter Mater. Phys. 2008, 77, 165429.

[86] Y. Miyauchi and S. Maruyama, Phys. Rev. B 74, 035415 _2006_.

[87]F. Plentz, H. B. Ribeiro, A. Jorio, M. S. Strano, and M. A. Pimenta, Phys. Rev. Lett. 95, 247401 _2005_.

[88] R. Saito, G. Dresselhaus, and M. S. Dresselhaus, Physical Properties of Carbon Nanotubes _Imperial College, London, 1998_.

[89]H. Htoon, M. J. O'Connell, S. K. Doorn, and V. I. Klimov, Phys. Rev. Lett. 94, 127403 _2005_.

[90] J. Lefebvre and P. Finnie, Phys. Rev. Lett. 98, 167406 _2007

[91] Perebeinos, V.; Tersoff, J.; Avouris, P. Effect of Exciton–Phonon Coupling in the Calculated Optical Absorption of Carbon Nanotubes. Phys. Rev. Lett. 2005, 94, 027402.

[92] J. Jiang, R. Saito, K. Sato, J. S. Park, Ge. G. Samsonidze, A. Jorio, G. Dresselhaus, and M. S. Dresselhaus, Phys. Rev. B 75, 035405 (2007).

[93] X. Qiu, M. Freitag, V. Perebeinos, and Ph. Avouris, Nano Lett. 5, 749 (2005).

[94] S. G. Chou, F. Plentz, J. Jiang, R. Saito, D. Nezich, H. B. Ribeiro, A. Jorio, M. A. Pimenta, Ge. G. Samsonidze, A. P. Santos, M. Zheng, G. B. Onoa, E. D. Semke, G. Dresselhaus, and M. S. Dresselhaus, Phys. Rev. Lett. 94, 127402 _2005_.

[95] Torrens, O. N.; Zheng, M.; Kikkawa, J. M. Energy of K−Momentum Dark Excitons in Carbon Nanotubes by Optical Spectroscopy. Phys. Rev. Lett. 2008, 101, 157401.

[96] Murakami, Y.;Lu, B.;Kazaoui, S.;Minami, N.;Okubo, T.;Maruyama, S. Photoluminescence sidebands of carbon nanotubes below the bright singlet excitonic levels. Phys. Rev. B 2009, 79 (19).

[97]Blackburn, J. L.; Holt, J. M.; Irurzun, V. M.; Resasco, D. E.; Rumbles, G. Confirmation of K−Momentum Dark Exciton Vibronic Sidebands using 13C Labeled, Highly Enriched (6,5) Single−Walled Carbon Nanotubes. Nano Lett. 2012, 12, 1398−1403.

[98]Matsunaga, R.; Matsuda, K.; Kanemitsu, Y. Origin of Low− Energy Photoluminescence Peaks in Single Carbon Nanotubes: K −Momentum Dark Excitons and Triplet Dark Excitons. Phys. Rev. B: Condens. Matter Mater. Phys. 2010, 81, 033401.

[99] Kadria−Vili, Y.; Bachilo, S. M.; Blackburn, J. L.; Weisman, R. B.J. Phys. Chem. C 2016, 120, 23898−23904.

[100] Kastner M., Stahl S., Vollert I., Loi C., Rühl N., Hertel T. A comparison of Raman and photoluminescence spectra for the assessment

of single−wall carbon nanotube sample quality. Chem. Phys. Lett., 635 (2015), pp. 245–249

[101] Hunter, C. A.; Anderson, H. L.What is Cooperativity? Angew. Chem., Int. Ed. 2009, 48, 7488– 7499

[102] Lemasson, F.; Berton, N.; Tittmann, J.; Hennrich, F.; Kappes, M. M.; Mayor, M.Polymer Library Comprising Fluorene and Carbazole Homo− and Copolymers for Selective Single−Walled Carbon Nanotubes Extraction Macromolecules 2012, 45, 713– 722,

[103] Mehlenbacher, R. D.; Wu, M.; Grechko, M.; Laaser, J. E.; Arnold, M. S.; Zanni, M. T.Photoexcitation Dynamics of Coupled Semiconducting Carbon Nanotube Thin Films Nano Lett. 2013, 13, 1495– 1501

[104] Schöppler, Friedrich, Christoph Mann, Tilman C. Hain, Felix M. Neubauer, Giulia Privitera, Francesco Bonaccorso, Daping Chu, Andrea C. Ferrari, and Tobias Hertel. "Molar Extinction Coefficient of Single−Wall Carbon Nanotubes." The Journal of Physical Chemistry C 115, no. 30 (August 4, 2011): 14682–86. doi:10.1021/jp205289h.

[105] Franklin, A. D.; Wong, H. S. P.; Lin, A.; Chen, Z. H. "Current Scaling in Aligned Carbon Nanotube Array Transistors with Local Bottom Gating." IEEE Electron Device Lett. 2010 , 31, 644–646.

[106] Capaz, Rodrigo B., Catalin D. Spataru, Paul Tangney, Marvin L. Cohen, and Steven G. Louie. "Temperature Dependence of the Band Gap of Semiconducting Carbon Nanotubes." Physical Review Letters 94, no. 3 (January 25, 2005). doi:10.1103/PhysRevLett.94.036801.

[107] S. Berger,C. Voisin, G. Cassabois,C. Delalande, P. Roussignol, X. Marie, Temperature Dependence of Exciton Recombination in Semiconducting Single−Wall Carbon Nanotubes Nano Letters 2007 7 (2), 398−402.

[108] S. Berger, F. Iglesias, P. Bonnet, C. Voisin, G. Cassabois, J.−S. Lauret, C. Delalande, P. Roussignol, Optical properties of carbon nanotubes in a composite material: The role of dielectric screening and thermal expansion, Journal of Applied Physics 2009, 105, 094323.

[109] D. Karaiskaj, C. Engtrakul, T. McDonald, M. J. Heben, A. Mascarenhas, Intrinsic and Extrinsic Effects in the Temperature − Dependent Photoluminescence of Semiconducting Carbon Nanotubes, Physical Review Letters 2006, 96, 106805.

[110] R. B. Capaz, C. D. Spataru, P. Tangney, M. L. Cohen, S. G. Louie, Hydrostatic pressure effects on the structural and electronic properties of carbon nanotubes, Physica Status Solidi (b) 2004, 241, 3352–335

[111] V. Perebeinos, J. Tersoff, P. Avouris, Radiative Lifetime of Excitons in Carbon Nanotubes,Nano Letters 2005,5, 2495–2499.

[112] C. D. Spataru, S. Ismail−Beigi, R. B. Capaz, S. G. Louie, Theory and Ab Initio Calculation of Radiative Lifetime of Excitons in Semiconducting Carbon Nanotubes, Physical Review Letters 2005, 95, 247402.

[113] K. Matsuda, T. Inoue, Y. Murakami, S. Maruyama, Y. Kanemitsu, Exciton dephasing and multiexciton recombinations in a single carbon nanotube, Physical Review B 2008, 77, 033406.

[114] Y.−f. Xiao, M. D. Anderson, J. M. Fraser, Photoluminescence saturation independent of excitation pathway in air−suspended single−walled carbon nanotubes, Physical Review B 2014,89, 235440.

[115] J. Lefebvre, P. Finnie, Y. Homma, Temperature−dependent photoluminescence from single−walled carbon nanotubes, Physical Review B 2004,70, 045419

[116] J. Shaver, J. Kono, Temperature−dependent magneto−photoluminescence spectroscopy of carbon nanotubes: evidence for dark excitons, Laser & Photonics Reviews 2007, 1, 260–274.

[117] Hagen, Axel, Mathias Steiner, Markus B. Raschke, Christoph Lienau, Tobias Hertel, Huihong Qian, Alfred J. Meixner, and Achim Hartschuh. "Exponential Decay Lifetimes of Excitons in Individual Single−Walled Carbon Nanotubes." Physical Review Letters 95, no. 19 (October 31, 2005). doi:10.1103/PhysRevLett.95.197401.

[118] Burke, P. J. Ac Performance of Nanoelectronics: Towards a Ballistic Thz Nanotube Transistor. Solid−State Electron. 2004, 48, 1981–1986.

[119] Franklin, A. D.; Luisier, M.; Han, S. J.; Tulevski, G.; Breslin, C. M.; Gignac, L.; Lundstrom, M. S.; Haensch, W. Sub−10 nm Carbon Nanotube Transistor. Nano Lett. 2012, 12, 758– 762.

[120] Jie, Z.; Lin, A.; Patil, N.; Hai, W.; Lan, W.; Wong, H. S. P.; Mitra, S. Carbon Nanotube Robust Digital VLSI. IEEE Trans. CAD 2012, 31, 453–471.

[121] Guo, J.; Hasan, S.; Javey, A.; Bosman, G.; Lundstrom, M. Assessment of High−Frequency Performance Potential of Carbon Nanotube Transistors. IEEE Trans. Nanotechnol. 2005, 4, 715–721.

[122] Citrin, D. S. "Long Intrinsic Radiative Lifetimes of Excitons in Quantum Wires." Physical Review Letters 69, no. 23 (December 7, 1992): 3393–96. doi:10.1103/PhysRevLett.69.3393.

[123] H. Akiyama, S. Koshiba, T. Someya, K. Wada, H. Noge, Y. Nakamura, T. Inoshita, A. Shimizu, and H. Sakaki, Phys. Rev. Lett. 72, 924 _1994_.

[124] Mortimer, I. B., and R. J. Nicholas. "Role of Bright and Dark Excitons in the Temperature−Dependent Photoluminescence of Carbon Nanotubes."

Physical Review Letters 98, no. 2 (January 12, 2007). doi:10.1103/PhysRevLett.98.027404.

[125] J. Shaver, J. Kono, O. Portugall, V. Krstic, G. L. J. A. Rikken, Y.Miyauchi, S. Maruyama, and V. Perebeinos, Nano Lett. 7, 1851_2007_.

[126] R. Matsunaga, Y. Miyauchi, K. Matsuda, Y. Kanemitsu, Symmetry−induced nonequilibrium distributions of bright and dark exciton states in single carbon nanotubes, Physical Review B 2009,80, 115436.

[127] Qian, Dong, Gregory J Wagner, Wing Kam Liu, Min−Feng Yu, and Rodney S Ruoff. "Mechanics of Carbon Nanotubes." Applied Mechanics Reviews 55, no. 6 (2002): 495. doi:10.1115/1.1490129.

[128] Kocabas, C.; Pimparkar, N.; Yesilyurt, O.; Kang, S. J.; Alam, M. A.; Rogers, J. A. Experimental and theoretical studies of transport through large-scale, partially aligned arrays of single−walled carbon nanotubes in thin film type transistors.Nano Lett.2007, 7, 1195 1202.

[129] Alam, M. A.; Pimparkar, N.; Kumar, S.; Murthy, J. Theory of nanocomposite network transistors for macroelectronics applications. MRS Bull. 2006, 31, 466 470.

[130] Hur, S. −H.; Kocabas, C.; Gaur, A.; Shim, M.; Park, O. O.; Rogers, J. A. Printed thin film transistors and complementary logic gates that use polymer coated single−walled carbon nanotube networks. J. Appl. Phys. 2005, 98, 114302.

[131] Aguirre, Carla M., Pierre L. Levesque, Matthieu Paillet, François Lapointe, Benoit C. St−Antoine, Patrick Desjardins, and Richard Martel. "The Role of the Oxygen/Water Redox Couple in Suppressing Electron Conduction in Field−Effect Transistors." Advanced Materials 21, no. 30 (August 14, 2009): 3087–91. doi:10.1002/adma.200900550.

[132] Anthopoulos, Thomas D., G. C. Anyfantis, G. C. Papavassiliou, and Dago M. de Leeuw. “Air–Stable Ambipolar Organic Transistors.” Applied Physics Letters 90, no. 12 (March 19, 2007): 122105. doi:10.1063/1.2715028.

[133] Schießl, Stefan P., Nils Fröhlich, Martin Held, Florentina Gannott, Manuel Schweiger, Michael Forster, Ullrich Scherf, and Jana Zaumseil. “Polymer–Sorted Semiconducting Carbon Nanotube Networks for High–Performance Ambipolar Field–Effect Transistors.” ACS Applied Materials & Interfaces 7, no. 1 (January 14, 2015): 682–89. doi:10.1021/am506971b.

[134] Gwinner, Michael C., Florian Jakubka, Florentina Gannott, Henning Sirringhaus, and Jana Zaumseil. “Enhanced Ambipolar Charge Injection with Semiconducting Polymer/Carbon Nanotube Thin Films for Light–Emitting Transistors.” ACS Nano 6, no. 1 (January 24, 2012): 539–48. doi:10.1021/nn203874a.

[135] Street, R. A., and A. Salleo. “Contact Effects in Polymer Transistors.” Applied Physics Letters 81, no. 15 (October 7, 2002): 2887–89. doi:10.1063/1.1512950.

[136] Brady, Gerald J., Yongho Joo, Susmit Singha Roy, Padma Gopalan, and Michael S. Arnold. “High Performance Transistors via Aligned Polyfluorene–Sorted Carbon Nanotubes.” Applied Physics Letters 104, no. 8 (February 24, 2014): 083107. doi:10.1063/1.4866577.

[137] Kim, Woong, Ali Javey, Ophir Vermesh, Qian Wang, Yiming Li, and Hongjie Dai. “Hysteresis Caused by Water Molecules in Carbon Nanotube Field–Effect Transistors.” Nano Letters 3, no. 2 (February 2003): 193–98. doi:10.1021/nl0259232.

[138] Bottacchi, Francesca, Luisa Petti, Florian Späth, Imge Namal, Gerhard Tröster, Tobias Hertel, and Thomas D. Anthopoulos.

„Polymer–sorted (6,5) single–walled carbon nanotubes for solution–processed low–voltage flexible microelectronics“. Applied Physics Letters 106, Nr. 19 (2015): 193302.

[139] C. A. Parker, Photoluminescence of Solutions, pp. 225–23 1, Elsevier, Amsterdam,1968

[140] R. Zimmermann, W. Fichtner, IEEE J. Solid–State Circuits 32 (1997) 1079.

[141] Wu, Z. "Transparent, Conductive Carbon Nanotube Films." Science 305, no. 5688 (August 27, 2004): 1273–76. doi:10.1126/science.1101243.

[142] Alam, M.A., N. Pimparkar, S. Kumar, and J. Murthy. "Theory of Nanocomposite Network Transistors for Macroelectronics Applications." MRS Bulletin 31, no. 06 (June 2006): 466–70. doi:10.1557/mrs2006.120.

[143] Kumar, Satish, Muhammad A. Alam, and Jayathi Y. Murthy. "Computational Model for Transport in Nanotube–Based Composites With Applications to Flexible Electronics." Journal of Heat Transfer 129, no. 4 (2007): 500. doi:10.1115/1.2709969.

[144] Kumar, S., J. Y. Murthy, and M. A. Alam. "Percolating Conduction in Finite Nanotube Networks." Physical Review Letters 95, no. 6 (August 1, 2005). doi:10.1103/PhysRevLett.95.066802.

[145] Kumar, S., N. Pimparkar, J. Y. Murthy, and M. A. Alam. "Theory of Transfer Characteristics of Nanotube Network Transistors." Applied Physics Letters 88, no. 12 (March 20, 2006): 123505. doi:10.1063/1.2187401.

[146] Kumar, S., J. Y. Murthy, and M. A. Alam. "Percolating Conduction in Finite Nanotube Networks." Physical Review Letters 95, no. 6 (August 1, 2005). doi:10.1103/PhysRevLett.95.066802.

[147] Cao, Qing, Hoon−sik Kim, Ninad Pimparkar, Jaydeep P. Kulkarni, Congjun Wang, Moonsub Shim, Kaushik Roy, Muhammad A. Alam, and John A. Rogers. "Medium−Scale Carbon Nanotube Thin−Film Integrated Circuits on Flexible Plastic Substrates." Nature 454, no. 7203 (July 24, 2008): 495–500. doi:10.1038/nature07110.

[148] Cao, Qing, and John A. Rogers. „Ultrathin Films of Single−Walled Carbon Nanotubes for Electronics and Sensors: A Review of Fundamental and Applied Aspects". Advanced Materials 21, Nr. 1 (2009): 29–53. doi:10.1002/adma.200801995.

[149] Pimparkar, N., C. Kocabas, Seong Jun Kang, J. Rogers, and M.A. Alam. "Limits of Performance Gain of Aligned CNT Over Randomized Network: Theoretical Predictions and Experimental Validation." IEEE Electron Device Letters 28, no. 7 (July 2007): 593–95. doi:10.1109/LED.2007.898256.

[150] Pimparkar, Ninad, Jing Guo, and Muhammad A. Alam. "Performance Assessment of Subpercolating Nanobundle Network Thin−Film Transistors by an Analytical Model." IEEE Transactions on Electron Devices 54, no. 4 (April 2007): 637–44. doi:10.1109/TED.2007.891871.

[151]Bottacchi, Francesca, Stefano Bottacchi, Florian Späth, Imge Namal, Tobias Hertel, and Thomas D. Anthopoulos. „Nanoscale Charge Percolation Analysis in Polymer−Sorted (7,5) Single−Walled Carbon Nanotube Networks". Small 12, Nr. 31 (2016): 4211–21. doi:10.1002/smll.201600922.

[152] Xia, Jiye, Guodong Dong, Boyuan Tian, Qiuping Yan, Han Zhang, Xuelei Liang, and Lianmao Peng. "Metal Contact Effect on the Performance and Scaling Behavior of Carbon Nanotube Thin Film Transistors." Nanoscale 8, no. 19 (2016): 9988–96. doi:10.1039/C6NR00876C.

[153] P R Gray; P J Hurst; S H Lewis & R G Meyer (2001). Analysis and Design of Analog Integrated Circuits (Fourth ed.). New York: Wiley. pp. 66–67. ISBN 0−471−32168−0.

[154] P. R. van der Meer, A. van Staveren, A. H. M. van Roermund (2004). Low−Power Deep Sub−Micron CMOS Logic: Subthreshold Current Reduction. Dordrecht: Springer. p. 78. ISBN 1−4020−2848−2.

[155] Sandeep K. Shukla; R. Iris Bahar (2004). Nano, Quantum and Molecular Computing. Springer. p. 10 and Fig. 1.4, p. 11. ISBN 1−4020−8067−0.

[156] Ashish Srivastava; Dennis Sylvester; David Blaauw (2005). Statistical Analysis and Optimization For VLSI: Timing and Power. Springer. p. 135. ISBN 0−387−25738−1.

[157]Merchant, Christopher A., and Nina Marković. "Effects of Diffusion on Photocurrent Generation in Single−Walled Carbon Nanotube Films." Applied Physics Letters 92, no. 24 (2008): 243510. doi:10.1063/1.2949742.

[158] B. Kitiyanan, W. Alvarez, J. Harwell, D. Resasco, *Controlled production of single-wall carbon nanotubes by catalytic decomposition of CO on bimetallic Co−Mo catalysts*, Chem. Phys. Lett. 317, 497–503 (2000).

[159] Dan, Budhadipta, Anson W. K. Ma, Erik H. Hároz, Junichiro Kono, and Matteo Pasquali. "Nematic−Like Alignment in SWNT Thin Films from Aqueous Colloidal Suspensions." Industrial & Engineering Chemistry Research 51, no. 30 (2012): 10232–37. doi:10.1021/ie3001925.

[160] Zhou, Ying, and Reiko Azumi. "Carbon Nanotube Based Transparent Conductive Films: Progress, Challenges, and Perspectives." Science and Technology of Advanced Materials 17, no. 1 (January 2016): 493–516. doi:10.1080/14686996.2016.1214526.

[161]Peng, Lian−Mao, Zhiyong Zhang, and Sheng Wang. “Carbon Nanotube Electronics: Recent Advances.” Materials Today 17, no. 9 (November 2014): 433–42. doi:10.1016/j.mattod.2014.07.008.

[162]Hu, Liangbing, David S. Hecht, and George Grüner. “Carbon Nanotube Thin Films: Fabrication, Properties, and Applications.” Chemical Reviews 110, no. 10 (October 13, 2010): 5790–5844. doi:10.1021/cr9002962.

[163] Murakami, Yoichi, Benjamin Lu, Said Kazaoui, Nobutsugu Minami, Tatsuya Okubo, and Shigeo Maruyama. “Photoluminescence Sidebands of Carbon Nanotubes below the Bright Singlet Excitonic Levels”. Physical Review B 79, Nr. 19 (7. Mai 2009). doi:10.1103/PhysRevB.79.195407.

[164] Wang, Qiguan, and Hiroshi Moriyam. 2011. “Carbon Nanotube−Based Thin Films: Synthesis and Properties”. In Carbon Nanotubes − Synthesis, Characterization, Applications, Siva Yellampalli. InTech. doi:10.5772/22021.

[165] Muhlbauer, Rachel L., and Rosario A. Gerhardt. “A review on the synthesis of carbon nanotube thin films.” Carbon Nanotubes: Synthesis and Properties (2012): 107−156.

[166] Fu, L., and A. M. Yu. "Carbon nanotubes based thin films: fabrication, characterization and applications." Rev. Adv. Mater. Sci 36 (2014): 40−61.

[167] Aldalbahi, Ali, Jin Chu, Peter Feng, and Marc Panhuis. “Conducting Composite Materials from the Biopolymer Kappa−Carrageenan and Carbon Nanotubes.” Beilstein Journal of Nanotechnology 3 (May 23, 2012): 415–27. doi:10.3762/bjnano.3.48.

[168]Aldalbahi, Ali, and Marc Panhuis. “Electrical and Mechanical Characteristics of bucky papers and Evaporative Cast Films Prepared Using Single and Multi−Walled Carbon Nanotubes and the Biopolymer

Carrageenan." Carbon 50, no. 3 (March 2012): 1197–1208. doi:10.1016/j.carbon.2011.10.034.

[169] Benesty, Jacob, Jingdong Chen, Yiteng Huang, and Israel Cohen. "Pearson Correlation Coefficient." In Noise Reduction in Speech Processing, by Israel Cohen, Yiteng Huang, Jingdong Chen, and Jacob Benesty, 1–4. Berlin, Heidelberg: Springer Berlin Heidelberg, 2009. doi:10.1007/978–3–642–00296–0_5.

[170] Mouri, Shinichiro, Miyauchi, Yuhei and Matsuda, Kazunari "Dispersion-Process Effects on the Photoluminescence Quantum Yields of Single-Walled Carbon Nanotubes Dispersed Using Aromatic Polymers" *The Journal of Physical Chemistry C* **2012** *116* (18), 10282-10286 doi: 10.1021/jp212040y

[171]R. Saito, G. Dresselhaus, M. Dresselhaus, Physical Properties of Carbon Nanotubes. 1998, Imperial College Press, London.

[172] M. Dresselhaus, G. Dresselhaus, R. Saito, A. Jorio, Raman spectroscopy of carbon nanotubes, Physics Reports 2005, 409, 47–99.

[173] P. Avouris, Z. Chen, V. Perebeinos, Carbon-based electronics, Nat. Nanotechnol. 2 (2007)605—615.

[174] T. Ando, *Excitons in Carbon Nanotubes*, J. Phys. Soc. Jpn. 66 (1997) 1066–1073, DOI: 10.1143/JPSJ.66.1066.

[175] V. Perebeinos, J. Tersoff, P. Avouris, *Scaling of Excitons in Carbon Nanotubes*, Phys. Rev. Lett. 92 (2004) 257402, DOI: 10.1103/PhysRevLett. 92.257402.

[176] T. Hertel, *Photophysics*, in D. M. Guldi, N. Martín (Hrsg.), *Carbon Nanotubes and Related Structures: Synthesis, Characterization, Functionalization, and Applications*, 1. Auflage, Wiley–VCH, Weinheim 2010.

[177] C. Kittel, *Introduction to Solid State Physics*, 8. Auflage, John Wiley & Sons, Hoboken, NJ 2004.

[178] J. Kong, E. Yenilmez, T. W. Tombler, W. Kim, H. J. Dai, R. B. Laughlin, L. Liu, C. S. Jayanthi, S. Y. Wu: Quantum interference and ballistic transmission in nanotube electron waveguides, Phys. Rev. Lett. 87, 106801 (2001) 459

[179] A. Javey, J. Guo, Q. Wang, M. Lundstrom, H. J. Dai: Ballistic carbon nanotube field–effect transistors, Nature 424, 654–657 (2003) 459, 460, 461, 462, 476

[180] M. J. Biercuk, N. Mason, J. Martin, A. Yacoby, C. M. Marcus: Anomalous conductance quantization in carbon nanotubes, Phys. Rev. Lett. 94, 026801 (2005) 459, 476, 477, 483

[181] Z. H. Chen, J. Appenzeller, J. Knoch, Y. M. Lin, P. Avouris: The role of metal–nanotube contact in the performance of carbon nanotube field–effect transistors, Nano Lett. 5, 1497–1502 (2005) 461, 462